ABSTRACT

Title of Document: INTERACTION OF INTENSE LASER PULSES WITH DROPLET AND CLUSTER SOURCES: APPLICATION TO EXTREME ULTRAVIOLET LITHOGRAPHY AND PLASMA WAVEGUIDE GENERATION

Hua Sheng, Doctor of Philosophy, 2006

Directed By: Professor Howard M. Milchberg
Department of Electrical and Computer Engineering &
Institute for Physical Science and Technology

Several topics were studied in the interaction of intense laser pulses with droplet and cluster sources. Laser pulse-formatting that can enhance laser-to-EUV conversion efficiency in the 13.5nm band for next generation lithography was first explored, using droplet sources as the laser target. Xenon droplets size distribution was measured, and the droplet plasma spectrum irradiated by various laser energies was scanned. A 2-pulse heater setup and a 4-pulse stacker scheme were built and studied. Results suggest that, unlike droplets of argon (Ar) and krypton (Kr), the ionization-state distribution in xenon may be much more transient. The decay timescales for 13.5nm emissions are approximately 0.5-1.5ns, a timescale intermediate to the results

from excitation and recombination emission in Ar and Kr droplet targets. Comparing xenon's results with argon's, the argon droplets generated a more robust ionization-stage distribution, while the xenon droplets generated a more transient ionization-stage distribution.

The second topic studied was an investigation of plasma waveguides generated in clustered gases, using 100ps long pump pulses axicon-generated Bessel beam. The plasma waveguide space and time evolution was measured, using picosecond interferometry. The resulting waveguides have both central densities as low as ~10^{18}cm^{-3} and small diameters, a desirable but hard to achieve combination for either hydrodynamic shock waveguides using conventional gases or for other techniques, such as discharge capillaries. Extremely efficient absorption of laser pulses by cluster targets was shown to extend to pulses significantly longer than the timescale for cluster explosive disassembly. These long pulse absorption efficiencies can be more than a factor of 10 greater than those in unclustered gas targets of the same volume average atomic density. The maximum long pulse absorption observed in cluster jets under our range of conditions was 35%.

A third topic explored was resonant pulse-shortening of Bessel beams in the under-dense (N_e is ~10^{-2} N_{cr}) plasma channels formed by 100ps Nd:YAG laser pulses. Pulse shortening was seen at two pressures under our range of conditions: 340torr and 460torr.

INTERACTION OF INTENSE LASER PULSES WITH DROPLET AND CLUSTER SOURCES: APPLICATION TO EXTREME ULTRAVIOLET LITHOGRAPHY AND PLASMA WAVEGUIDE GENERATION

By

Hua Sheng

Dissertation submitted to the Faculty of the Graduate School of the
University of Maryland, College Park, in partial fulfillment
of the requirements for the degree of
Doctor of Philosophy
2006

Advisory Committee:
Professor Howard M. Milchberg, Chair
Professor Thomas M. Antonsen, Jr.
Professor John Melngailis
Professor Charles Tarrio
Professor Michael Zachariah

Dedication

To my parents.

Acknowledgements

Firstly, I thank my advisor, Professor Howard M. Milchberg, for supporting this work for all these years. He provided me with a stimulating research environment and showed me how to be creative, insightful, and joyous, and he shared with me his original ideas about this research project. More importantly, under his knowledgeable guidance, I learned how to transit from a student acquiring learning from books and lectures to a researcher thinking independently and acquiring knowledge from other pioneers' work. He also earned special thanks for carefully reading and editing this dissertation.

Second, I thank Professor Thomas M. Antonsen, Professor John Melngailis, Professor Charles Tarrio, and Professor Michael Zachariah for serving on my doctoral dissertation committee.

I am indebted to Dr. Jingyun Fan, Dr. Enrique Parra, Dr. Vinod Kumarappan, Dr. Ki-Yong Kim, and Mr. Brian Layer for their valuable assistance in performing the experiments, and I am indebted to Mr. Jianwei Liu, Mr. Brian Epstein, and Mr. Greg Moore for their continuous help with much mechanical machining. They have my everlasting appreciation and best wishes.

Finally, I am grateful to my family—my parents; my brother, Can; and my fiancée, Jingzhi—and many friends for their endless love and caring, so that I could complete this dissertation. Their unwavering belief in me was an invaluable incentive to finish this work.

Table of Contents

List of Figures

Chapter 1: Research Motivation and Introduction to EUV Lithography and EUV sources

1.1 Overview

Thirty years ago the calculation speed of a state-of-the-art computer was very slow, compared to today's desktop machines, and the space it occupied was as large as several rooms. Today's computers are more compact and powerful because of integrated circuits (ICs). One of the key technologies for making ICs ever smaller is lithography. Lithography is a photographic process used in the manufacturing of ICs to transfer circuit patterns from a mask to the silicon surface by imaging the pattern on the mask onto a semiconductor wafer covered with light-sensitive photoresist. The traditional imaging system for those tasks has employed transmissive optics (lenses). Creating circuits with even smaller features has required ever finer resolution; the resolution of the imaging system is proportional to the wavelength of the light used. Therefore, shorter and shorter wavelengths are desirable. Historically, several different wavelengths have been used. Currently, high-volume lithography techniques use, as a mask illumination source, KrF excimer laser light at a wavelength of 248nm and ArF excimer laser light at 193nm; both are in the deep ultraviolet range (150nm to 300nm). The feature size on a chip they are capable of printing is 350- to 130-nm for KrF lasers and 130- to 65-nm for ArF lasers, respectively. Another candidate light source is 157nm F_2 excimer lasers, but light is strongly absorbed instead of

transmitted by conventional lens imaging systems. A historical development diagram is shown in Fig. 1.1. There has been considerable recent interest in exploring wavelengths in the extreme ultraviolet (EUV) range (5nm to 50nm)" [1], which is approximately ten to twenty times shorter in wavelength. Such light can be produced, for example, by synchrotrons, laser-produced plasmas, or plasma discharges. The consideration of using this wavelength range has been motivated by the development of mirrors with high-reflection efficiency that operate in that range [2]. The reflective optics are multilayer mirrors, composed of alternating $\lambda/2$ thickness layers of high Z (atomic number) and low Z materials. The mirror of choice for EUV, which is the best one developed and understood [2], has alternating molybdenum and silicon layers (MoSi multilayer mirror). So, while the reduction imaging paradigm for lithography is intact, both the light source and the imaging system have changed radically, from excimer lasers to hot plasma; and from lenses to multilayer mirrors. Semiconductor manufacturers are currently deciding which lithographic technique to use in the next generation of microchip manufacturing. Currently, there are five possible choices: EUV lithography (EUVL) [3], x-ray (0.1nm to 5nm) lithography [4], maskless lithography (ML) [5], electron-beam projection lithography (EPL) [6], and ion-beam projection lithography (IPL) [7]. In many respects, EUVL is similar to optical lithography, as practiced today [8]. EUV lithography can achieve good depth of focus and linearity to provide for sufficient process control and to yield the desired control of critical dimensions within a tolerable process window [8]. Now, the EUV-based technique is considered the most promising and feasible for a feature size of 45nm and below [9]. Most of industry money is being used to investigate such

systems. Currently, each world region has an independent program to development EUVL. In Europe, a MEDEA-sponsored program (Microelectronics Development for European Applications 1997-2000, MEDEA+ 2000-present)—the industry-initiated pan-European program for advanced co-operative research and development in microelectronics—focuses on "system innovation on silicon for the e-economy". In Japan, ASET's (the Association of Super-Advanced Electronics Technologies) EUVL program has begun studying EUVL technology since 1998. A consortium (EUV-LLC) consisting of Intel®, AMD®, IBM®, Motorola®, Infineon® and Micron Technology® was founded in United States. Basic research on the scheme is underway and all elements of EUVL technology were successfully demonstrated in a full-field "proof of concept" lithography tool called the Engineering Test Stand (ETS) at Sandia National Laboratories in Livermore, California in 2001 [10]; this tool is capable of printing feature-size resolution of 70-nm. In late 2004, Intel® installed the world's first commercial EUV lithography tool, called a Micro Exposure Tool (MET), which is capable of printing feature-size resolution of 30-nm but only has a very small field size of 600μm x 600μm (a full field size is 26mm x 32mm). An EUV alpha-demo tool with larger commercial-scaled field-of-view brought by Zeiss and ASML corporations in Europe is currently under assembly and will be delivered to the Interuniversity Microelectronics Center (IMEC) in Belgium in 2006 for testing. It will have sufficient throughput and imaging capability for a feature size of 45-nm [11].

Although many achievements and much progress have been accomplished, many challenges still lie ahead. The biggest challenges and risks for the EUVL, as the

next generation of lithography systems, involve sufficient source power to achieve high-throughput systems [9]. Laser-driven plasma is one of the leading candidates for the EUV source in EUVL. Condensed xenon gas, in the form of droplet sprays and liquid jet filaments, has emerged as one of the most promising laser targets to generate the EUV source. However, source efficiency, with respect to laser pulse energy, of EUV emission in the 13.5nm acceptance band of Mo:Si multilayer optics is still as low as ~1% with condensed xenon targets. Therefore to obtain higher conversion efficiency (to EUV source power) is crucial. The details will be discussed in Sections 1.2.5 and 1.2.6.

Many factors determine source efficiency. The main factors under experimental control are target design, laser focusing geometry, laser pulse energy, laser wavelength, and pulse temporal structure.

We conducted an experiment to help determine the optimum conditions for EUV source efficiency with laser-heated xenon droplet plasmas. In particular we controlled the laser pulse temporal as well as the focal structure. In parallel we continued 1D calculation to simulate laser interaction with droplets. The calculations provided (1) physical insight into designing our pulse-formatting experiments and (2) guidelines for general source design. The details are discussed in Sections 1.3 and 1.4 and in Chapters 2 and 3.

This chapter is organized as follows: the next section (Section 1.2) introduces the entire EUVL system, where each component of the system is addressed. Emphasis is given to the EUVL source and source targets. Section 1.3 describes the research motivation. In Section 1.4 the research scope and objectives are specified.

1.2 Engineering Test Stand (ETS) - EUV Lithography prototype system

In 1997, three Department of Energy national laboratories—Lawrence Livermore, Lawrence Berkeley, and Sandia—formed the Virtual National Laboratory (VNL), funded by EUV-LLC, to research and develop an EUV lithography prototype system. In 2001, the first full-scale prototype EUVL machine, called the Engineering Test Stand (ETS) located at the Sandia National Laboratories, was completed. The ETS consisted of six subsystems: a laser-produced plasma EUV source, condenser optics, projection optics, a mask, precision scanning stages, and a vacuum enclosure. Laser-produced xenon plasma supplied the extreme ultraviolet radiation at the wavelength of 13.5nm with bandwidth of 2%, and the radiation was collected by a complex condenser optics system whose purpose was to bring as much light as possible to the lithographic mask. The mask was then imaged by projection optics onto a semiconductor wafer with a reduction of 4:1 or 6:1, depending on the design of projection optics. The optical layout is shown in Fig. 1.2.

1.2.1 Condenser optics sub-system

Traditionally optics concentrates a light source onto a small area, using a lens or combination of lenses. However, in EUVL systems, EUV radiation is strongly absorbed in virtually all materials, even gases. Therefore, EUVL imaging systems must be entirely reflective. On one hand, because the more light delivered, the shorter exposure time needed, this translates a greater chip-manufacturing rate. So, the EUV condenser system consists of multilayer-coated concave mirrors; it collects as much EUV light as possible from the source and directs it onto the mask. On the other hand,

in lithography, it is also extremely important that the image characteristics are invariant across the imaging field. The condenser optics sub-system plays a critical role here, too. Several different designs were proposed [12-15].

1.2.2 Multilayer coating

The reflectivity of a single mirror-surface for EUV light is very small, which depends on the choice of mirror material, the angle of incidence θ, and the wavelength λ. The model of a complex refractive index of mirror material is described as $n = 1 - \delta - i\beta$, where δ is the decrement of the real part of the refractive index and β is the absorption index. The amplitude reflectivity is calculated by Fresnel equation [16]. The Molybdenum has a normal incidence amplitude reflectivity of about 0.04 for 13.5nm radiation. Ignoring the effects of absorption, this means if we can arrange to get the reflections from 25 molybdenum-vacuum interfaces to add with the correct phase relationship, then one can achieve a reflectivity close to 1. Based on this principle, even though materials with zero absorption at EUV wavelengths do not exist, it is still possible to choose pairs of real materials with satisfactory optical constants. By depositing a stack of ultra-thin films with alternately high and low values of δ, where the thickness of the individual film is adjusted so that the reflections from each interface add in phase at the top of the stack, usefully high reflectivity at normal incidence can be achieved through the use of such multilayer interference coatings. The coatings, largely amorphous or polycrystalline in nature, consist of alternating high and low Z materials. The

response of those multi-layers is strongly wavelength-selective. The peak of the reflectivity of the stack is given by Bragg's law [17].

$$m\lambda=2d\sin(\theta) \qquad (1.2)$$

Where m=1, 2, 3… is the order of the reflection, the first order (m=1) is commonly used for EUV and x-rays. λ is the wavelength of incident light, d is the thickness of one bi-layer pair of the multilayer coating, and θ is the incident angle between the EUV beam and the plane of the multilayer. For normal incidence ($\theta = 90^0$), a periodicity d equals λ/2 of the illumination light, for EUV of interest at ~13.5nm, the total thickness of one bi-layer pair of such coating is ~6.7nm. A side view of such a coating is shown in Fig. 1.3. The reflectivity of a multilayer coating depends on a number of factors. By taking absorption into account, the contrast in β is also important for achieving optimum reflectivity [18]. Typically, high-absorption layers are thinner than low-absorption layers for optimum reflectivity. Importantly, the reflection bandpass of such mirrors can be made narrower by making the absorber layers thinner than optimum while the peak reflectivity will be reduced [19]. The final reflectivity of a multilayer coating also depends on the roughness of the interfaces [20]. Normal incidence reflectivity of approximately 70% has been achieved [21-23] in the EUV with Mo/Si corresponding to 13.5nm. The spectral bandpass for those mirrors is of the order 1/N, where N is the number of layer pairs, typically between 30 and 50 for high reflectivity. The deposition of up to 100 or more ultrathin layers having constant and uniform thickness requires special technology. Multilayer coatings are most commonly made by a vacuum-deposition process, such as

evaporation [24] or sputtering [20, 25-29]. Both methods can yield good multilayer coatings [20]. Sometimes the coating is topped by an oxidation-resistant capping layer, such as Ru, to extend its lifetime [30]. A great advantage of multilayer interference coatings is that they can be applied to curved substrates [31] for use in imaging applications, such as microscopes and telescopes [32]. Multilayers have been used to coat optical elements for instruments, such as EUV optics, spectrometers and monochromators at synchrotron radiation beamlines. In EUV lithography, a multilayer coating is used not only on the projection mirrors and condenser mirrors but also on the masks to enhance the EUV power reflectivity on those EUVL components. EUVL would be impossible without multilayer coating.

1.2.3 Projection optics sub-system

Projection optics plays the core role in the lithographic exposure system. It determines the resolution of the imaging system. The two fundamental characteristics of an imaging system are governed by the following two equations:

$$\text{Resolution} = k_1 \lambda / \text{NA} \tag{1.3}$$

$$\text{Depth of Focus} = k_2 \lambda / (\text{NA})^2 \tag{1.4}$$

Depth of focus (DOF) is a measurement of how much distance exists wherein the photoresist plane will remain sharply in focus. In lithography, DOF is the total range of focus that can be tolerated; that is, the range of focus that keeps the resulting printed feature within a variety of specifications. NA denotes the numerical aperture of the lithographic imaging system, and λ represents the wavelength of the radiation light used in lithography, corresponding to 13.5nm for EUVL. k_1 is a constant that is

a figure of merit for the lithography process, indicating how cleverly the lithographer used the light source. k_2 is also a constant. For lithographic application, k_1 and k_2 are dependent not only upon optical system, but also upon the photoresist recording and processing. The smaller the value of k_1 is, the better the resolution is. A value of k_1 lower than 0.5 requires advanced resolution-enhancement technologies, which bring more constraints on shape design and a significant cost increase. Those technologies include alternating phase-shift masks [33], double-exposure dipole [34], and others. Historically, values for k_1 and k_2 had to be greater than 0.6 for use in high-volume manufacturing [35]. Those equations show that there is significant trade-off between resolution and DOF. Better resolution can be achieved by reducing λ and increasing NA while DOF is decreased. The requirement for DOF that was used in high-volume manufacturing already exceeded 0.5μm [35]. In the earlier ETS implementation for the purpose of acquiring experience in the development of EUV high-volume manufacturing tools, the four multilayer mirrors of the ETS projection optics system (POB1) were installed in the ETS [36]. It had a 4x reduction and an NA of 0.1 at the wafer [37]. With the POB1 design, the resolution of 70nm was achieved at a k1 value of 0.52 [38].

There are two main characteristics of mirrors under major scrutiny because of the effects on the image quality. They are wavefront quality [39] and intrinsic flare [40-41]. Flare is unwanted light that reaches the photoresist by scattering from the optical components of a lithography tool system [42-43]. The light that was supposed to shine on an area of an image intended to be bright was redirected to those regions of the image intended to be dark by scattering, which results in background

illumination within the image field. Intrinsic flare can reduce image contrast, lead to critical dimension (CD) variations, and shrink the process window. Where CD is the width of a line or space that has been identified as critical to the device operating properly and measured on the wafers in lithography, and process window is a contour plot of the high and low CD specifications as a function of focus and exposure. Mid-spatial frequency roughness of the imaging mirror surfaces creates the flare. The flare for a given feature size is measured as the ratio of the dose to clear the bright region to the dose to clear the dark feature. POB1 offered wavefront error of ~ λ/14 rms and 50% flare [37]. However, it is shown that the required range of flare must be controlled to be within 11% for commercial EUV optics [42]. So a higher-quality projection system with the similar design, the second projection optics box (POB2), has been fabricated. Measured wavefront error and flare are ~ λ/20 rms and 18%, respectively [44-45]. For installation of POB2 in the ETS, lithographic characterization was experimentally explored [38]. However, such design has very small NA (=0.1), which is only suitable for 70-nm resolution. In order to extend EUVL down to 45-nm resolution, the NA is expected to be approximately 0.25. To achieve that goal, another high NA small-field exposure system was developed with an NA of 0.3 [46] and imaging field of 300μm x 500μm [47]. In that design, the projection optics consists of two aspherical mirrors that achieved wavefront error of 1.9nm rms corresponding to ~ λ/7.

1.2.4 EUV masks

The EUVL mask consists of 5 layers: substrate, the Mo/Si multilayer

(reflecting EUV at 13.5nm), buffer layer (protecting Mo/Si multilayer when repairing absorber layer), absorber layer (absorbing EUV at 13.5nm) and EUV photo resist. The EUV substrate is made from the 6" x 6" x 0.25" low thermal expansion material (LTEM) such as ULE® or Zerodur® [48] which must have low spatial variation in thermal expansion. High reflectivity of the multi-layer coating requires a very smooth substrate. Usually 80-100 pairs of multi-layers are deposited on the LTEM substrates serving as the reflection part of EUV masks. Absorber layer then serves as absorption part of EUVL masks. A buffer layer between multi-layers and absorber layer on EUVL masks plays a role of protecting the multi-layers during absorber layer repair. A key breakthrough in this area was the development of an Ultra Clean Ion Beam Sputter Deposition System about 5 years ago [49]. Significant progress has also been achieved in both multilayer smoothing [50] and defect repair [51]. The first ETS mask with minimum features 30nm has been successfully fabricated by Intel® and ensured the successful ETS demonstration [52].

1.2.5 EUV sources

As discussed earlier, one of the main obstacles in the realization of EUV lithography is that no source of EUV radiation is currently available that meets all the specifications for a commercial tool. To enable the throughput of 100 wafer/hour and achieve uniform dosage control, next-generation semiconductor chip manufacturing using EUVL requires a brilliant radiation source with an output power ~115 W at 13.5nm within 2% bandwidth (BW) at the entrance of the EUV illuminator system (intermediate focus IF) and a pulse energy stability of ±0.3% (3σ, integral over 50

pulses) [53]. The diagram of IF is illustrated in Fig. 1.4. To date, only a maximum of ~50 W at IF in 2% BW of 13.5nm with gas-discharge produced plasma from tin sources has been reported [54]. The development of a suitable source for the generation of EUV energy remains the primary barrier to the introduction of an EUVL system in the Intel®-planned 2009 time frame. Several source concepts have been proposed and are under development; they are all based on hot plasmas. They include electrically driven gas-discharge produced plasmas (GDPP), such as z-pinch [55-57], dense plasma focus [58-59], capillary discharge [60-66], and hollow cathode triggered (HCT) discharge [67-68], as well as laser-produced plasma (LPP) [69] concepts.

From the continuum spectrum-emission perspective, assuming the plasma as a black-body radiator, the plasma should maintain a temperature of ~20eV or ~220000K [70] in order to provide the maximum yield of EUV light source at wavelength around 13.5nm, according to Wien's law [71]:

$$\lambda_{\max} = \frac{250\, nm \bullet eV}{T_e} \tag{1.5}$$

On the other hand, from the specific line-emission perspective, $\lambda_{\max}$ is dependent on target species and on whichever ionization stage of the target is dominant among all ionization stages in the produced plasma.

Such EUV light is then collected by the condenser and focused to an intermediate point (IF), where it serves as the entrance of EUV illumination for EUVL system shown in Fig. 1.4. For estimating the power requirement at the location of the plasma source, based on the power requirement at IF, the power losses between the plasma source and the IF have to be taken into account. they are (a) the loss of the

condenser resulting from reflectivity of the condenser optics and solid angle of collection and (b) the loss resulting from the absorption of the debris-mitigation system and spectral-purity filter. The debris mitigation system mitigates debris particles that are formed during production of EUV radiation for the long operational lifetime of EUV optics, and the spectral purity filter is used to reduce out-of-band radiation in the ultraviolet, visible, and infrared, which also propagates through the optical system and degrades the image or heats the wafer stage. From the point of view of solid angle of collection, the larger the size of the produced plasma, the smaller the collecting angle is.

In a Z-pinch setup, a column of plasma in pre-filled gas is generated by a current driven in the axial (z) direction by an electrical power source producing an azimuthally directed magnetic field that tends to confine the plasma [72]. During the typical dynamic Z pinch process, a high-voltage pulse is applied to two electrodes from a capacitor bank. The current passes through the initial load gas, a column of conducting plasma is formed, having an axial current channel through the process of breakdown, rapid ionization (dominant avalanche ionization), and heating of an initially cold gas. The resulting plasma is propelled rapidly toward the axis by the pressure of the azimuthal magnetic field produced by the current flowing in the plasma. The plasma is compressed and heated. At stagnation, the thermal pressure of the plasma is balanced by plasma inertia and by the magnetic pressure. The discharge's electrical energy is converted first to the kinetic energy of the imploding plasma, then to its thermal energy after its stagnation at the axis, and part of the energy is then radiated away from the plasma volume in the EUV and x-ray spectral

ranges [72]. That is the goal of the whole process. Some of the energy is consumed as ohmic and compressional heating of the plasma during implosion and stagnation. Generally, compact, uniform pinches on the axis produce the high plasma densities and temperatures that are needed to achieve a large EUV power. The widely used working gas is xenon (Xe) gas from 4d-5p transitions [73] of Xe^{10+} corresponding to near 13.5nm EUV emission of interest.

The dense plasma focus has the similar principle as Z-pinch, except for an unusual electrode design. Two main types of plasma-focus devices are widely used: the Filippov [74] type and the Mather [75] type. The main difference is the aspect ratio of D/L, where D is the anode diameter and L is its height. The Filippov type has D/L >1 while the Mather type has D/L <1. The discharge is initiated at one end of the electrodes and a current sheet is formed because of the initial axially non-uniform shape of a pinch resulting from the special designs of the electrodes. During the propagation of the current sheet to the axis before the final pinch compression, part of the energy stored in the capacitor bank is converted into kinetic and thermal energy of the imploding plasma. Then the current sheet converges to the axis, further compressing the imploding plasma, and most of energy is transformed into thermal energy, just as the Z-pinch plasma method does. Eventually part of the thermal energy is radiated in the form of EUV and/or soft x-rays. The conversion efficiency from the energy stored in the capacitors to EUV at a wavelength of 13.5nm within 2% BW is sensitive to many factors, such as the energy stored in the capacitor bank, the shape of the electrodes, the material of the anode, filling gas species, filling gas pressure, and the insulating walls [76]. Currently, the conversion efficiency from the

energy stored in the capacitors to EUV at a wavelength of 13.5nm within 2% BW is up to 1% with xenon gas [77].

The electric capillary discharge source is one of the smallest, simplest, and most economically attractive. The typical setup is described as follows: A several-hundreds- of-a-micron diameter hole is drilled, centered on the axis in a several-tens-of-millimeter diameter and ~0.5-3cm long ceramic disk; two metal electrodes are attached on the two end surfaces of the ceramic disk. The anode is hollow to allow xenon gas to flow into the capillary. The discharge is initiated by supplying high voltage across the electrodes. A surface discharge is formed in the hole. The discharge is confined by the capillary, and a high density, local thermodynamic equilibrium plasma is formed [78]. Previous work on the EUV electric capillary discharge source has shown a consistent increase in power generation and a reduction in debris generation over the past several years [78-80]. The recent development in this scheme achieved >9W of EUV power within 2% BW of 13.5nm at IF in burst mode at 1kHz [81].

The hollow-cathode triggered (HCT) source has electrodes with central bore holes opposite each other, connecting to a capacitor bank that is charged to a high voltage. Additionally, a trigger electrode is inserted into the hollow cathode and put on a positive voltage of a few hundred volts with respect to the cathode potential. Its basic function is to remove the initial electrons in the hollow cathode prior to a breakdown, hence preventing the breakdown altogether. Switching the trigger to off immediately moves the system into breakdown when the capacitor is charged to a specific voltage. Breakdown occurs spontaneously when increasing the voltage

because of this special design. Therefore, no external switch or solid insulator in the vicinity of the discharge region is needed. That is the key advantage of the HCT source. The effect of the trigger is a widening of the operation margins. In particular, it allows operation over a wide pressure range. More importantly, timing of the pulses is now entirely determined by the timing of a low-power trigger pulse. The recent advances in this area have been reported in reference [82]. Approximately 3W EUV power at 13.5nm in 2% BW at the IF is achieved.

However, the hot plasmas generated by all the above GDPP concepts are very close (<several mm) to the discharge electrodes. The generated debris may easily contaminate the discharge electrodes. Moreover, the GDPP has electrode mass loss because of excessive heating, which causes condensation of target on optics. Thermal management of the electrode discharge region—because it is very close to the discharge electrodes—prevents the GDPP sources from achieving the high-power levels required for high-volume manufacturing. The size of the typical GDPP source is generally ~1mm x 1-3mm.

Laser-produced plasmas (LPP) are one of the leading candidates for the EUV source in next-generation EUV lithography. In a typical setup, a pulsed Nd:YAG laser with moderate power (~10^{10}-10^{12}W) and high repetition rate (>1kHz) heats the target, such as xenon, and generates the plasma, which generates the EUV of interest. The leading edge of the laser pulse generates some free electrons via multi-photon ionization (MPI) [83]. If the peak laser focus intensity is higher than ~10^{13}W/cm^2, field ionization may take place in the case of a xenon target. The initial seed free electrons will be further heated by absorbing energy from the remaining part of the

laser pulse through inverse *bremsstrahlung* [84-86], in which many electron-ion collisions occur. Absorption occurs as the quiver energy of electrons in the laser field is converted into random thermal energy. The process is also called collisional heating [84-85]. When electrons are heated to energies greater than the ionization potentials of the atoms and ions, the collisional ionization [84] arises and frees more electrons to be heated. Some of the absorbed energy is then radiated via line emission after ion excitation by collisions or via continuum emission by recombination or scattering. Most of the absorbed energy is converted into kinetic energy of expansion of the plasma. Condensed xenon gas, in the form of droplet sprays and liquid jet filaments, has emerged as one of the most promising laser targets. The resulting interaction plasma produces EUV light at 13.5nm, consistent with the highest reflectivity of MoSi mirrors (approximately 70%). The identified strongest line corresponding to ~13.5nm is the band of $4d^8$-$4d^7$5p transitions in Xe^{10+} [87]. Xenon droplets or liquid jet filaments are typically generated through a gas jet with high backing pressure such that the laser-droplet/laser-filament interaction area can be far away (~several mm to several cm) from the jet opening. Compared with GDPP, the distance of the nearest hardware for LPP (gas jet) from the plasma can be roughly as 10 times far as that for GDPP (electrodes).Therefore, components of laser-plasma sources are less likely to be damaged. Also, cooling requirements are ~100X relaxed for laser plasma. Moreover, the typical size of the laser-produced plasma (depending on both the target size and laser focus size, generally ~100μm x several hundred μm) is smaller than that of the gas-discharge-produced plasma, more EUV power generated from LPP is useable, compared with GDPP from the point of view of solid

angle of collection. The typical geometry for GDPP is discussed in reference [70] and the typical geometry for LPP is discussed in reference [88] and shown in Fig. 1.5. Generally, the transmission into the IF is likely to approach 50% for LPP and is lower for GDPP because of a smaller solid angle of collection. However, only ~15W of power at IF is achieved with LPP to date, compared with ~50W of power at the IF achieved with a GDPP running with xenon gas [77]. To increase the drive efficiency into EUV power remains the biggest challenge for LPP. Nevertheless, the significant portion of energy transformed into dissipated heat for GDPP is a big issue [88]. At the end of 2004, Cymer Inc., located in San Diego, California, announced that they have chosen to focus on LPP because of the ever-increasing challenge of GDPP after their long-time research and development on GDPP [88].

1.2.6 Source targets

Because high conversion efficiency (CE) from input laser power to output EUV power at the wavelength of 13.5nm in a 2% BW (FWHM 0.53nm) is very important, a number of laser-plasma source targets have been investigated for EUVL. There are some materials that have been considered efficient spectral emitters in the 13-14nm range including oxygen (O_2) [89], gold (Au), tin (Sn) [90-91], lithium (Li) [88, 92-93], and xenon (Xe) [94-97]. However, the long lifetime of collector optics is required to minimize the operation cost. As discussed earlier, the performance of the collector optics is strongly dependent on its multi-layer (ML) coating, which can be degraded by deposition of the source element and debris. Both GDPP and LPP generate debris, which cause erosion and deposition of materials on mirrors. This

causes the diffusion of source materials into the ML structure and the interaction of the energetic ions with the collector optics in the source chamber. Ultimately, those debris mechanisms degrade mirror reflectivity. Oxygen-based targets result in the oxidation of the collector mirror capping layer, which reduces reflectivity and increases the replacement costs for this mirror [98]. Predominantly, 4d-4f transitions in tin ion stages (Sn^{8+}-Sn^{13+}) producing unresolved transition arrays (UTAs) [99] makes it a very promising high CE target and the CE of 3% in 2% BW of 13.5nm has been achieved [100]. In that experiment, a pulse-duration of 1.2ns, wavelength of 1.05μm, peak intensity of 0.5-1 x 10^{11}W/cm^2 laser pulse was used to heat a 1μm thick tin layer coated on a spherical plastic target with a diameter of 300-750μm. Simulations of laser-produced plasmas formed from a spherical solid Sn predicted CE as high as 3.5-6% could be obtained [91]. However, the metal vapor and particulates generated in Sn LPPs remains a big issue. Gold has the same problem. In December 2004, Cymer Inc. announced that they had have achieved a CE of >2.5% with lithium droplets [88]. The collector lifetime might be extended by using a capping layer on the ML and heating system to evaporate any deposited lithium because of its lower evaporation point [88]. Nevertheless, to minimize contamination, it is preferable to use a target consisting of inert gas atoms [101] because such gases will not react chemically with the multilayer mirrors. Xenon, which does not condense on surfaces at room temperature and emits broadband radiation (10-14nm from Xe^{9+}-Xe^{17+} ions [102]), became very attractive and now is one of several promising primary LPP targets for the goals of intense EUV emission and clean operation. Additionally, by recycling xenon gas, with filtering and periodic re-injection, a xenon target system

can be operated indefinitely at low operating cost. The highest CE achieved with xenon to date is 1.2 % in the form of solid targets [103] and 1% with frozen xenon droplets [70].

To fully realize the potential of xenon LPP sources in high-volume manufacturing EUV tools, a xenon target system must be developed—one that achieves high laser power to EUV power CE, and minimum collector-mirror degradation. In the xenon target-development history, xenon targets in the form of gas were initially used. However, laser to EUV CE in the 2% BW at 13.5nm was very low because of the low number-density of atoms. Therefore, high-density xenon is essential and desirable for high CE. Several different approaches and implementations of xenon targets have been evaluated with the goals of achieving high CE: pulsed, or continuous Xe cluster targets [104], planar solid Xe targets [105], spray of liquid Xe aerosols [106], liquid Xe filaments [107], liquid Xe jets [108], and liquid Xe droplets [109]. There is no xenon target concept that meets all the EUV light-source requirements. A LPP using a solid xenon target can realize high CE ~1.2% [103], but solid-xenon replenishment has the associated debris, which will be a challenge for high pulse-rate systems. Among them, the xenon droplet targets have demonstrated extended operating lifetimes without significant debris contamination [110]. For the longer term, filament and droplet sources seem to have the greatest potential for high power and high repetition-rate operation [106], where the filament is typically formed by pressurizing xenon behind an orifice at a temperature of about -100C and ejecting a continuous jet of the liquid into a vacuum, and the droplets are

typically formed by a spontaneous break-up mechanism because of the minimization of surface energy, while ejecting a jet of the liquid into vacuum.

1.3 Research Motivation

As discussed above, laser-driven plasma is one of the leading candidates for the EUV source in next-generation EUV lithography. Condensed xenon gas, in the form of droplet sprays and liquid-jet filaments, has emerged as one of the most promising laser targets to generate the EUV source. However, source efficiency, with respect to laser pulse energy, of EUV emission in the 13.5nm acceptance band of Mo:Si multilayer optics is currently 1%, using a liquid xenon filament [111] and frozen xenon droplets [70]. This is a significant increase over previous efficiencies of <0.5% with droplet spray jets [112], but it still remains too low to achieve CE >4% [88] for a cost-effective EUV stepper.

Different laser wavelengths have been used to explore the laser-to-EUV conversion efficiency at 13.5nm within 2% BW by using different lasers, such as CO_2 lasers, Nd:YAG lasers, and Nd:YLF lasers [113] and by higher harmonics of a Nd: YAG lasers [114-115]. In the industrial setups of EUV source suppliers, only Q-switched pulses of duration ~6.5-10ns have been used to drive those targets.

Many factors affect source efficiency. The main ones under experimental control are: target design, laser focusing geometry, laser pulse energy, laser wavelength, and pulse temporal structure.

Compared with liquid-filament targets, droplet sources provide a good test case for exploring source-efficiency issues.

(a) Matching of spatial and therefore temporal scales: Average droplet diameters are controllable in the range 5-50 μm through jet temperature, backing pressure, and jet orifice diameter [116]. Current liquid continuous-filament targets are of diameter <30 μm, so that droplet conditions can be found, and so that the spatial scales are matched. Thus, hydrodynamic timescales for laser-driven plasma evolution from filaments and droplets of similar diameter should be comparable.

(b) Droplets form a simple system with which to understand basic efficiency issues: Droplets can be completely consumed by the laser pulse; while, in laser interaction with continuous filament, one must consider thermal and mechanical interaction of the plasma with the undisturbed filament material above and below the focused laser spot.

(c) Flexibility for pulse formatting: Spray droplet streams can be made as thin as ~ 1mm with slits or skimmers [116-118], so that laser pulse propagation time through the droplet stream can take as little as ~3ps for 100ps laser pulses. For single droplets, propagation time is not an issue. Thus, experiments testing pulse shape, width, multiple pulses, or pre-pulse are not sensitive to the fact that the droplets are spatially distributed throughout a portion of the laser focal volume.

(d) Ease of use: In spray jets, as many (10-100) droplets will occupy the focal volume so that highly accurate laser focal spot alignment is not required. Furthermore, because the jet is pulsed, much less gas is consumed than with liquid filaments. Chamber background pressures are easily maintained by small pumping systems, and gas recovery systems are not needed.

As some industry efforts utilize a liquid-filament source [112], investigations of conversion efficiency in that geometry would ideally use a liquid-filament jet. Ultimately, for the best fit benchmarking with industry results, a liquid-filament jet is desirable because there is no temporal synchronization problem between the laser pulses and the liquid-xenon filament targets.

We conducted an experiment to assist in the determination of optimum conditions for EUV-source efficiency in condensed xenon droplet targets. In particular, we controlled the laser pulse temporal structure, as well as the focal structure. In parallel, we continued 1D calculations in radial and planar geometry (both thin-film and semi-infinite slab) to simulate laser interaction with droplets and liquid filaments. Those calculations provided (1) physical insight into designing our pulse formatting experiments and (2) guidelines for general source design.

1.4 Research Scope and Objective

The goal of the experiment was to explore laser pulse formatting and condensed xenon-target characteristics that can enhance laser-to-EUV conversion efficiency in the 13.5nm band appropriate to MoSi multilayer optics. The approach was one in which the fundamental physics basis for enhanced EUV emission is elucidated.

One of the critical time scales for laser droplet plasma interaction is the time τ_{crit} for the plasma to expand below critical density, where the laser droplet-plasma coupling drops significantly. Critical density is defined as $N_{cr} = m\omega^2 / 4\pi e^2$, where m is the electron mass, ω is the laser frequency, and e is the electron charge. For

1064nm laser pulses used in this experiment, $N_{cr} \approx 10^{21} cm^{-3}$. In our earlier group work, We proposed $\tau_{crit} \approx \frac{R}{c_s}(\frac{N_{e0}}{N_{cr}})^{\frac{1}{3}}$, where R is the droplet radius, N_{e0} is the pre-expansion electron density, c_s is the plasma sound speed given by $c_s = \sqrt{\frac{\gamma Z k_B T_e}{m_i}}$ [119], and γ is the ratio of the specific heats at constant pressure and constant volume for electrons. For an ideal gas of electrons and ions, $\gamma = \frac{5}{3}$, Z is the average ionization, m_i is the ion mass, T_e is the electron temperature, and k_B is Boltzmann's constant. For typical values $N_{e0} = 2 \times 10^{23} cm^{-3}, N_{cr} = 10^{21} cm^{-3}$, and $c_s \approx 10^7 cm/s$ (for a plasma temperature of several tens eV), $\tau_{crit} \approx$ 200ps for 7 -μm krypton droplets, and ≈280ps for 10 -μm krypton droplets [120]. We have found in previous experiments, using fixed energy and variable-width laser pulses (100fs-10ns), that EUV generation from micron-sized krypton droplets is most efficient for pulse durations of ~200-300ps [118]. The model is in reasonable agreement with the experiments. Therefore, $\tau_{crit} \approx$ 100ps to ~1ns for the xenon droplets with size range of 5-50μm discussed above seem most likely.

As a good starting point, we concentrated exclusively on the ~100ps to ~10ns timescale regime. In that process, we developed time-resolved diagnostics appropriate to the picosecond timescales of target disassembly for spray jets.

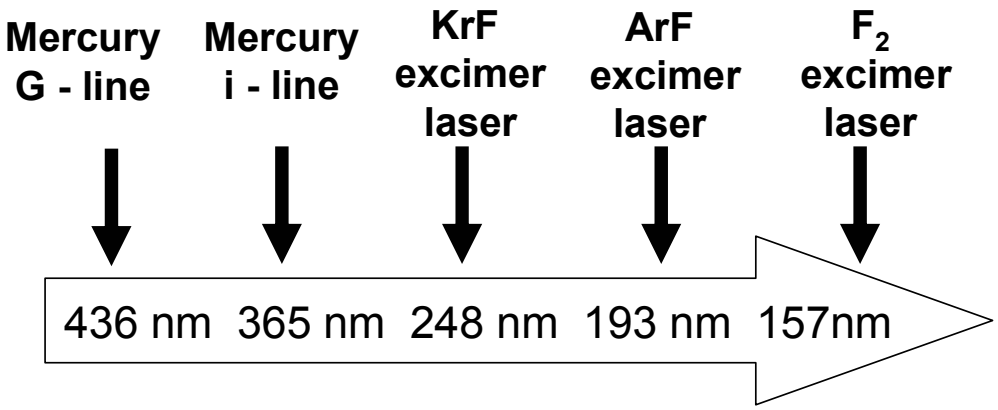

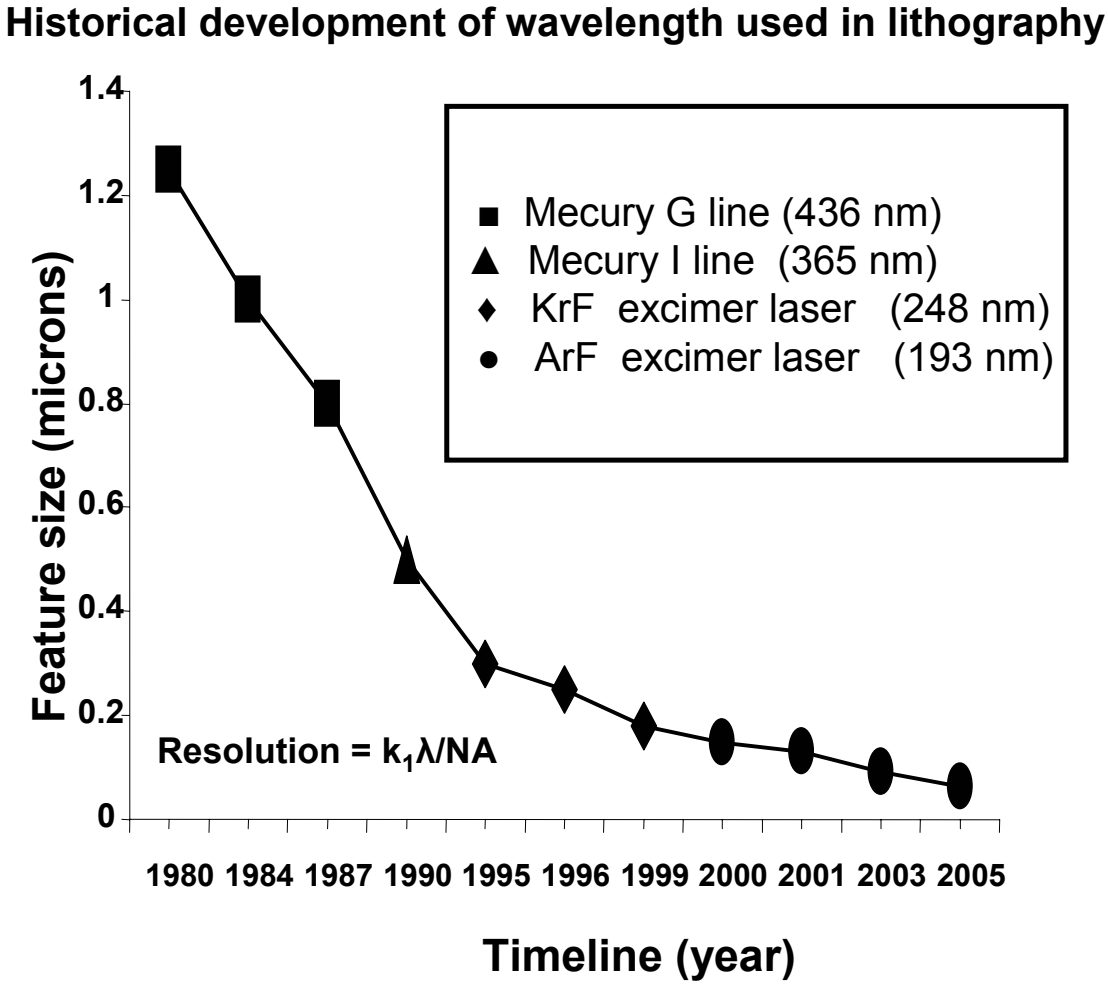

Figure 1.1: Schematic diagram of historical development of illumination wavelength used in lithography

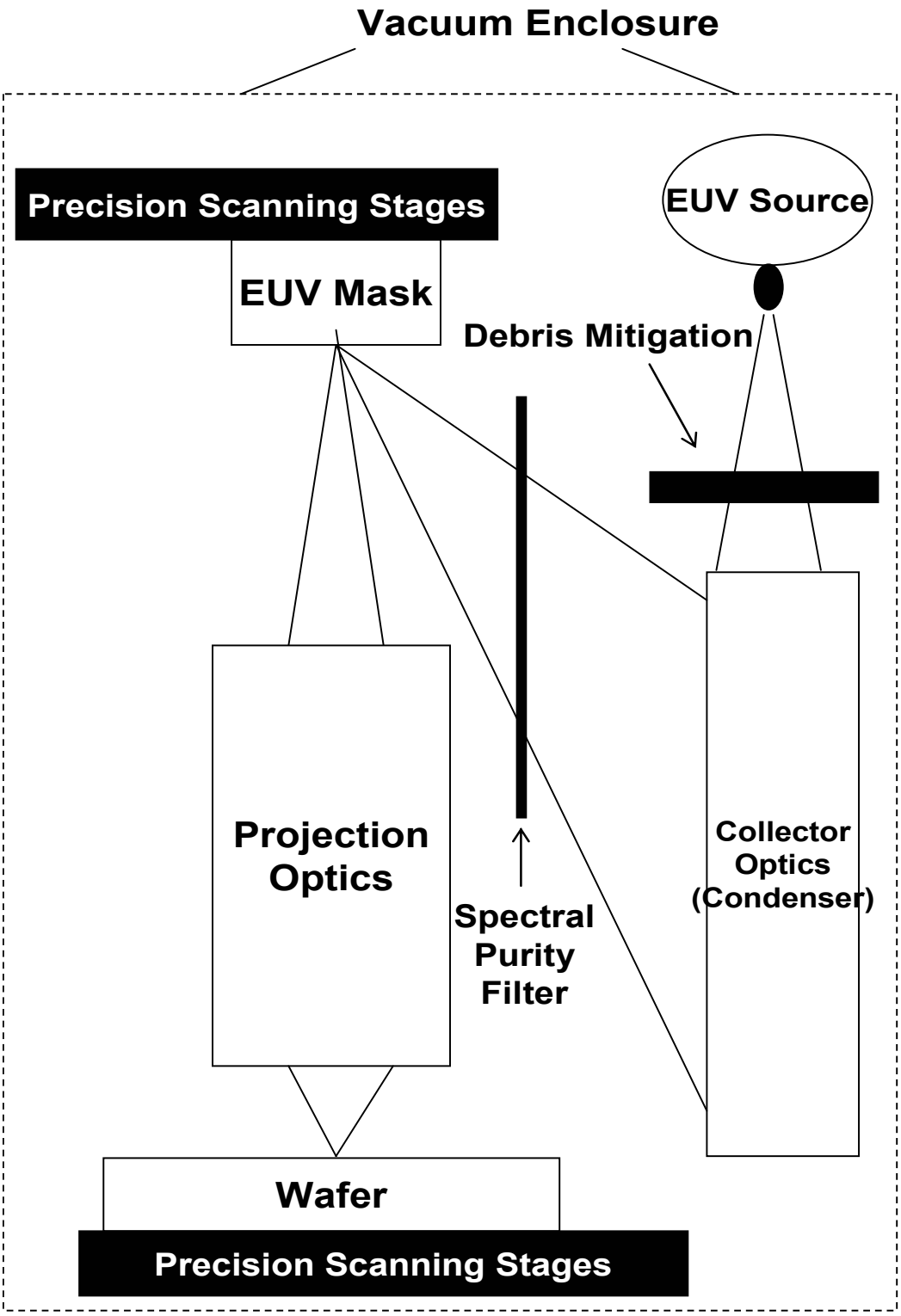

Figure 1.2: Block diagram of optical layout of the Engineering Test Stand (ETS)

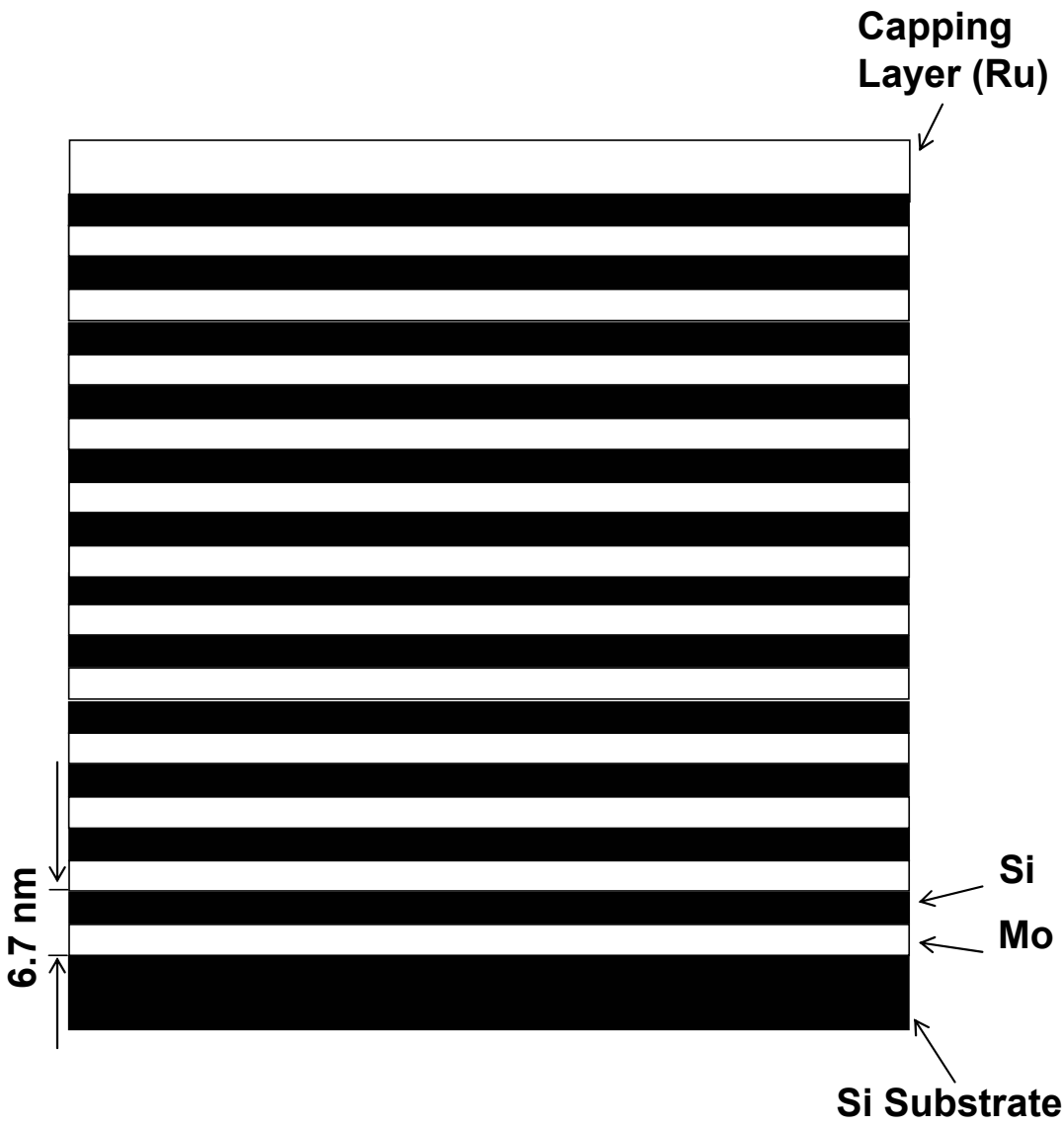

Figure 1.3: Side view of a multilayer interference coating. In this example there are 12 layer of molybdenum (white) and silicon (black). The d-spacing, the thickness of one layer pair of Mo and Si, is 6.7nm. Sometimes, a capping layer made of Ru is applied.

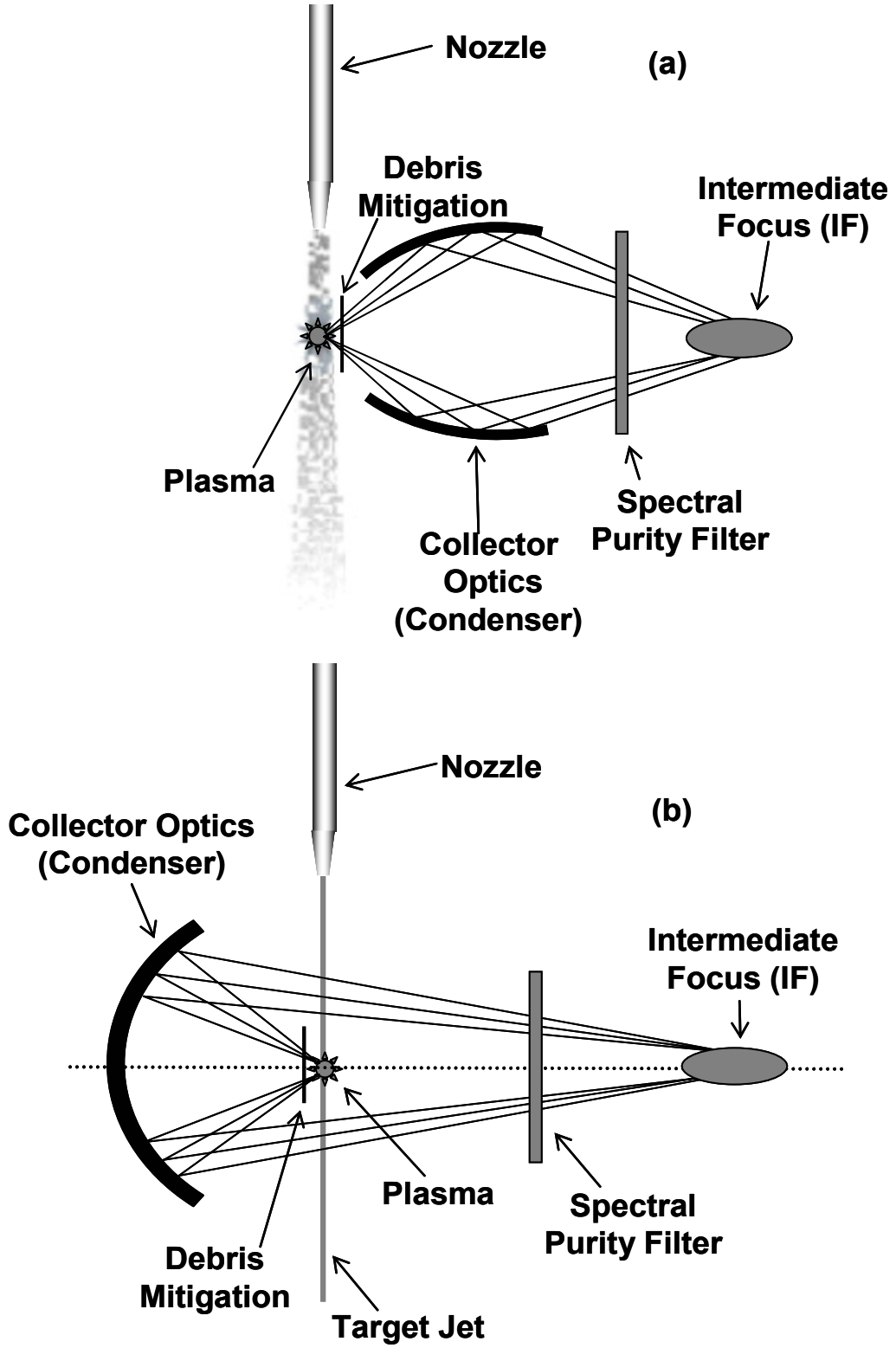

Figure 1.4: Schematic of an intermediate focus generated by an EUV source with collector module, (a) schematic view with forward collector, (b) schematic view with backward collector.

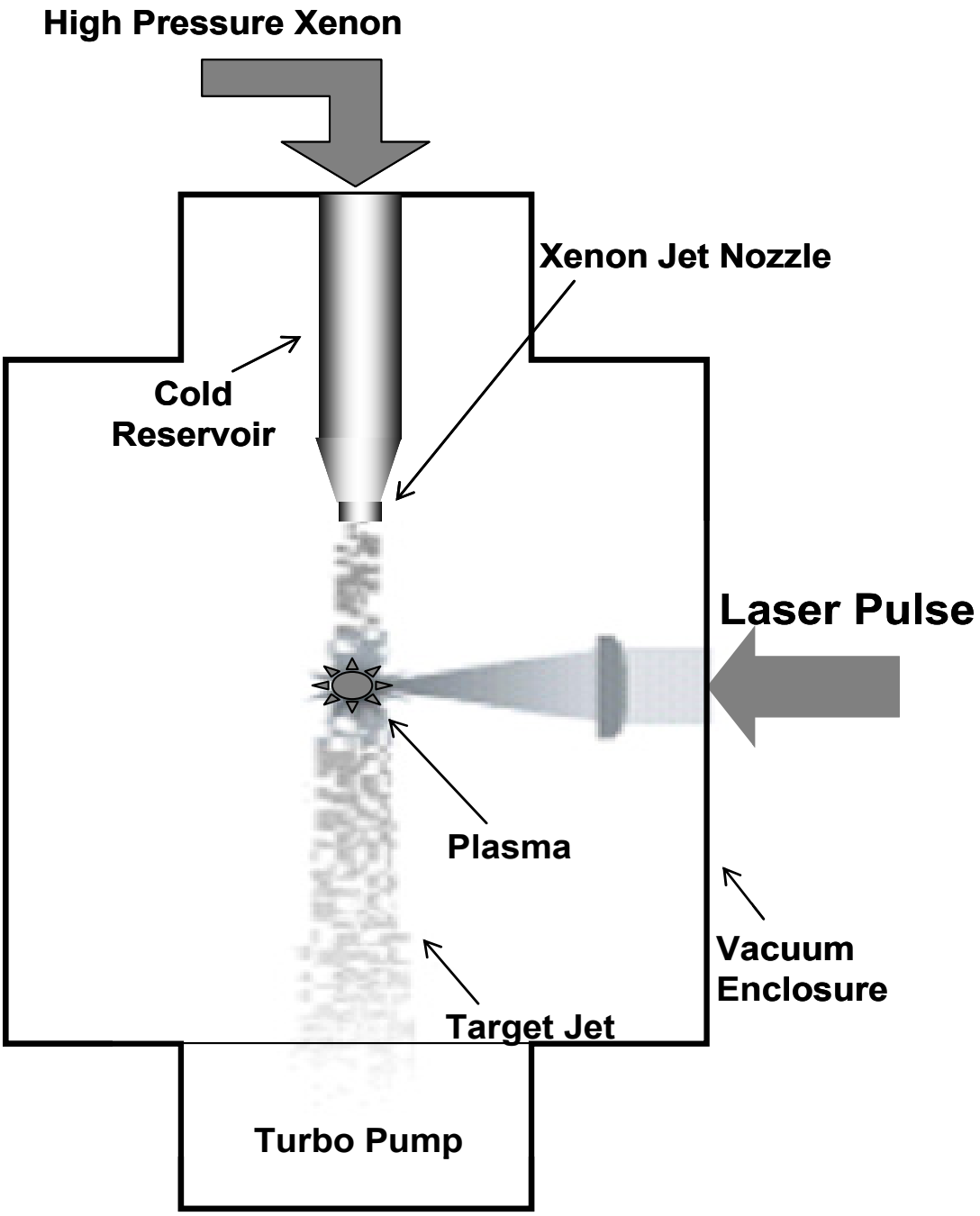

Figure 1.5: Typical schematic of laser produced EUV plasma (LPP) setup with xenon jet target.

Chapter 2: Laser System, Cryogenic Droplet Source, and Experimental Chamber

2.1 Nd:YAG Laser System

The high-power laser used in this experiment is a 100ps pulse duration Nd:YAG (Neodymium doped Yttrium Aluminum Garnet)-based system that is comprised of a Coherent 'Antares' 100ps 76MHz active mode-locking oscillator, a regenerative amplifier (RGA), and Power Amplifiers PA1 and PA2. Figure 2.1 is a block diagram that shows the output beam energies at each level. Each functional block and the intermediate optical path will be described in the following subsections. The overall optics layout showing the detail construction of our Nd:YAG system is in Fig. 2.2.

2.1.1 Oscillator and pulse down-sampling

The output of the oscillator is a 76MHz train of 100ps pulses with an average power ~20W. Such output serves as the short-pulse seed beam to our cascaded homemade Nd: YAG amplifier system. The mode-locker driver of this oscillator has two 38MHz synchronized signal outputs. One of them is frequency-divided down to 10Hz to trigger a pulse slicer (PS) and downstream amplifiers in the Nd:YAG laser system, and to externally trigger the pockels cell (PC1) in our homemade regenerative amplifier. 5W out of the ~20W beam is picked up from the Nd:YAG oscillator output

by a half-wave plate (HW1) and thin-film polarizer (TFP1) combination and then injected to the PS. The PS consists of a pockel cell (PC) and a polarizer. Without applying high voltage (HV), the PS allows vertical-polarized laser beams to pass through it and blocks horizontal-polarized laser beams. Whenever the $\lambda/2$ HV electric pulse is applied to the PC, the PC acts like a half-wave plate that rotates the beam polarization by 90 degrees from horizontal-polarization to vertical-polarization. The PS is triggered so that only 10 pulses per second in the 76 MHz pulse train from the oscillator are allowed to continue to the RGA. All the other pulses are dumped. This switch is completed within ~4ns, which is fast enough to pick up a single laser pulse from the 76MHz oscillator pulse train. The measured transmission contrast of this PS for vertical-polarized vs. horizontal-polarized laser beams is greater than 500:1.

2.1.2 Regenerative amplifier

The 10Hz signal seed beam is then directed into the flash-lamp pumped Nd:YAG regenerative amplifier (RGA), which is of a self-filtering unstable resonator design[1-2]. The RGA cavity contains a gain medium (a flash-lamp pumped Nd:YAG crystal rod), a quarter-wave ($\lambda/4$) plate, and a pockels cell (PC1). The self-filtering unstable resonator is designed as follows: the cavity length is equal to (f_1+ f_2), where f_1 and f_2 are the focal lengths of the cavity end mirrors M1 and M2, respectively (both concave), and $f_1 > f_2$. A spatial filtering aperture is put at the common focal position of M1 and M2 to eliminate sensitivity to the seed pulse spatial mode and to generate a near Gaussian RGA output mode. The aperture size is $a = (0.61 f_2 \lambda)^{1/2}$. The beam

propagation process in the RGA is a repeatable sequential process of focusing, filtering, and re-collimating. The effective magnification is given by $M_{eff} = 1.5\, f_1/f_2$. To maximize energy extraction from the rod and at the same time minimize the diffraction rings in the far field caused by aperture effect of the rod edges, f_1 and f_2 were selected as 1500mm and 375mm, respectively, to ensure that the output beam diameter $D = 1.5(f_1/f_2)2a$ is equal to the rod diameter of 1/4″. An optical switch consisting of PC1 and a $\lambda/4$ plate was used to allow the pump energy to build up a population inversion in the gain medium before the seed beam arrives. When the switch is open, approximately 15 roundtrips of amplification would occur. Finally, the input of ~5nJ 100ps single seed-pulse can be amplified to have an energy of ~10mJ. The output beam has a spatially smooth near-Gaussian beam profile.

2.1.3 PA1 and PA2

The 10mJ laser pulse output from the RGA is further directed to and amplified by the first and second power amplifiers (PA1 and PA2). PA1 is a ring-amplifier. The final output energy of PA1 is approximately 200mJ. Typically, in short-pulse power amplifiers, self-focusing and gain saturation must be considered. As for self-focusing, the rod diameter and length of PA1 were chosen as 3/8″ and 3″ (10mm x 75mm), respectively, which can accept over 20 times the power of RGA, with the beam size in PA1 over twice its size in RGA. Considering gain saturation and optimal energy extraction, the pulse energy density (J/cm^2) prior to the final pass should be close to the saturation energy density, and the beam size should fill the rod cross-section as much as possible. The saturation energy density for Nd:YAG at line center is

$0.370 J/cm^2$ [3], which implies that an energy of about 230mJ will saturate on the final pass for the beam size of ~9mm. For the same considerations, and avoiding the potential damage to PA2 rod, only 50mJ output beam energy of 200mJ is directed into PA2; all the remaining 150mJ is dumped either by a thin-film polarizer (TFP4) and half-wave plate (HW6) combination or by a following vacuum spatial filter (VSF). Before it reaches PA2, the pulse is directed into a VSF, which smoothes the beam profile by eliminating local modulations of its intensity through a Fourier transform mechanism. The size of the PA2 rod is 9.52mm X 104mm. After the PA2, the Nd:YAG laser system provides up to 1J/pulse, which could be split into multiple output beam pulses for applications. To eliminate the hot spots and fringes caused by clipping at the rod edges and the uneven temperature profile of the PA2 rod, a vacuum-relay imaging tube is used. Such vacuum-relay imaging tube performs two tasks: 1) It expands the laser beam to a larger diameter to avoid the potential damage to the following optics, and 2) It relays the image of the output aperture of PA2 to the entrance of the target chamber, essentially projecting the near-field of the beam to the experiment. The goal is to geometrically transfer the beam-intensity distribution onto a desired plane located in the target chamber, impeding development of far-field diffraction fringes that would otherwise distort the spatial profile of the laser beam if it were left to propagate in free space.

2.2 Cryogenic droplet source

As discussed in Chapter 1, a droplet source has some advantages over other EUV sources. Our experiment used a droplet source only.

Droplets are formed by the injection of a liquid into a vacuum. The formation process varies depending on conditions such as jet velocity, nozzle geometry, liquid supply pressure, liquid turbulence, and temperature, etc [4-12]. There are many ways to generate droplets. One is by directly connecting a liquid supply to the nozzle, when the substances are liquids at room temperature. If the substances are gases at room temperature, another approach is by cooling the gas valve at high pressure, where a gas-to-liquid phase transition is induced, creating a liquid supply in the local gas reservoir. Droplets form when the liquid is injected out of the nozzle attached to the valve body. Such is the case in our laboratory.

The Weber number is used to describe the different flow conditions. It is the ratio of the inertial force to surface tension force calculated by

$$W_e = v^2 \frac{d\rho}{\sigma}, \tag{2.1}$$

where v is the flow velocity (m/s), d is the nozzle orifice diameter(m), ρ is the liquid density (kg/m^3), and σ is the surface tension (N/m) [4], which contains the combined effects of inertial forces, gravity, surface tension, and viscosity. Four main breakup regions are categorized according to their Weber number. They are $W_e \approx 1$ (dripping regime) [4], $W_e \geq 10$ (Rayleigh regime) [4, 8], $W_e \approx 10^3$ (second wind-induced breakup regime) [4], and $W_e \geq 10^5$ (atomization regime [12]). For the conditions of argon-droplet formation in our laboratory, d = 500 μm, v_{Argon} ~ 200m/s [13], ρ_{Argon} = 1400kg/m^3, σ_{Argon} = 0.012N/m [14], and We is around 2 x 10^6. For the conditions of xenon-droplet formation in our experiments, d = 500 μm, v_{Xenon} is ~200m/s estimated from the sound speed in liquid Xe at 190K is 353m/s [15], ρ_{Xenon} =

3060kg/m^3, σ_{Xenon} = 0.019N/m [14], giving We ~3 x 10^6. Both, having $W_e \geq 10^5$, are well within the atomization breakup regime. In that regime the liquid fragmentation is a spray that diverges immediately from the nozzle exit and contains droplets that have an average diameter much smaller than the nozzle diameter [13].

Our droplet source is driven by a standard commercial stainless-steel solenoid valve (General Valve Corporation series 9). It consists of a shell, body, poppet, O-ring, main spring, buffer spring, and armature. Its mechanical structure is shown in Fig. 2.3. The solenoid valve is actuated and synchronized with the arrival of the laser pulses, using a high-speed high voltage pulser (General Valve IOTA ONE) with a minimum valve-opening time of several hundred microseconds and external trigger of 10Hz laser pulses. The high-voltage pulser provides a ~300 volt pulse for actuation and 28 volt holding voltage for keeping the valve open. The valve seals are optimized for high-pressure cryogenic operation. Instead of standard gasket seals made of stainless steel, copper seals are used to minimize leakage. That has the advantage of reducing the background gas pressure in the vacuum chamber in order to minimize EUV photo absorption. The maximum backing pressure used in our experiments is ~1000psi. The standard Teflon poppet was replaced with a harder Kel-F one; that increases the poppet's longevity by minimizing deformation over time.

At the valve backing pressures and temperatures of the experiments, the supply gas liquefies in the gas reservoir behind the poppet shown in Fig. 2.3. When the valve opens, liquid is ejected into the vacuum and fragments into droplets [13, 16]. The phase diagram for xenon, argon, and krypton is shown in Fig. 2.4. The black circle and squares show the locations of the liquid argon operating region on the

argon phase diagram and liquid xenon operating region on the xenon phase diagram, respectively, for our spray jet.

The precise and stable temperature control of the valve (so as to fix the operating point on the working gas phase diagram) is combined by a cooling supply of liquid nitrogen and two Omega Engineering CSS-10150 solid-state cartridge heaters. A copper-jacketed cooling block was designed to clamp to the valve body in the center, and the liquid nitrogen supply feeds the cooling block, while the heaters are clamped on the sides of the block. A type-T thermocouple and an Omega Engineering CN77324 electronic temperature controller are used to measure and monitor the temperature of the valve. The jet with this cooling-block setup together is mounted onto a single vacuum flange through which passes a tube for the working gas, the valve body, the liquid nitrogen cooling line, electrical feedthroughs, and a thermocouple sensor feedthrough. This arrangement is shown in the photograph in Fig. 2.5.

An elevated liquid-nitrogen-filled dewar supplies the liquid nitrogen to the block via a gravity feed. By carefully adjusting the power (0-55W) of the heaters, the temperature is well controlled within ±0.25K at any given set point within the range of 100-300K [13]. The valve backing pressure is controlled by the gas regulator connected at the output of the working gas cylinder. To have the laser interact with as few droplets as possible—which can help us understand the laser-droplet interaction more easily, but can still allow detection of acceptable EUV and x-ray signals—a 1mm diameter skimmer is used to narrow and collimate the stream of droplets as

shown in Fig. 2.6. It is located 1cm below the valve orifice and 4.5cm above the laser-droplet interaction region [13].

2.3 Pulse-temporal formatting

To maximize EUV and x-ray emissions from the droplet for a given laser-pulse energy, an intrinsic limitation on laser-coupling efficiency is the droplet lifetime, after which the laser-heated droplet plasma expands to an electron density below plasma critical density [17], whereupon laser-light absorption will decrease significantly. That suggests that the EUV/x-ray emissions from laser-heated droplets should be a strong function of pulse-temporal structure. Therefore, we conducted our experiments to explore the laser-droplet coupling efficiency by varying laser-pulse temporal structure.

2.3.1 Schemes for variable pulse width

A well known way to obtain variable pulse widths is to use a grating stretcher [18]. However, in the case of our Nd: YAG laser, the output bandwidth of our mode-locked oscillator is around ~1 Å. To stretch such a pulse with a grating stretcher from 100ps to 1ns, a length of free propagation of the beam would be approximately 1 km that is not feasible in our laboratory environment. Another approach is to make a pulse stacker. Several types of pulse stacker have been investigated [19-23]. The basic concept of a pulse stacker is to divide an initial laser pulse into a number of pulses, then delay and attenuate each pulse and finally recombine the modified pulses

to form the desired pulse shape. In reference [19], two mirrors and two beam splitters were used to generate N stacked pulses. In that scheme the pulse is injected onto the beam splitter at an angle, the reflection from the beam splitter propagates to a mirror, which then reflects the beam back onto the beam splitter. Subsequent reflections from this beam splitter produce a train of transmitted pulses that are delayed in time and separated in space. Individual attenuators were placed in each of these beams to shape the pulse. A second beam-splitter-and-mirror combination was then used to recombine the pulses into one beam. The advantage of such a system was that the construction was very simple and able to provide a wide variety of pulse shapes for use. Nevertheless, even with optimum reflectivity, the over-all efficiency would be on the order of 1-5% which is not acceptable for our intense pulse applications.

Another design uses several parallel-sided glass plates at normal incidence with individual multi-layer dielectric coatings [22]. The reflections from each surface are separated in time by the difference in their optical path lengths. Only three or four plates (six to eight surfaces), having 150ps delay between reflections, are needed to generate the ~1ns pulse from the 100ps short pulse. The disadvantage of that design is that the reflectivity of the individual multi-layer coating on each plate has to be preset before the stacker is assembled for a particular pulse width. In reference [23], basic triangle multiple optical-ring cavities utilizing partially transmitting beam splitters were used to stretch a laser pulse. The optical delay time between the adjacent leakage pulses was controlled by the optical propagation path length (L) in the optical cavity, and the pulses' energy distribution was determined by the intra-cavity leakage rate. The pulses leaving one cavity could then be further stretched out in temporal

profile by injecting them into other cavities. A 100ps delay between the adjacent pulses is equivalent to a 3cm space separation. It requires that our pulse-stretcher system with such a design to be very compact; for our laser system, it can only be implemented before RGA because of the very small beam size requirement of this design. Our approaches are different. Two schemes were designed by using the half-wave plate and thin-film polarizer combination and beam splitters. In Section 2.3.2-3, our implementations are described.

2.3.2 Pump-probe scheme

The simplest method of temporal-pulse formatting is to create two adjustable-amplitude pulses with variable delay between them. The optical scheme for doing that is shown in Fig. 2.7. The beam is first split into two beams by a thin-film polarizer (TFP1) and half-wave plate combination. One, a vertical-polarized beam, goes to the second thin-film polarizer (TFP2) directly by two reflective mirrors (M3 and M4) coated at 1064nm. The other is directed to a variable optical-delay line before it reaches TFP2. At TFP2 the two beams are recombined collinearly to the same direction again, but the original Nd:YAG beam is split into two 100ps pulses, which can be temporally separated by 0 to 14ns. The object of the experiment is to heat the droplet with the first, or pump pulse, producing the ion stages responsible for the EUV emission of interest. The variably delayed second, or probe pulse then further heats the droplet plasma. We expected that the additional EUV emission contributed by that pulse was dependent on the pump-probe delay. The inference from this measurement was the degree to which a

pulse of fixed energy but variable width can sustainably produce efficient EUV emission.

2.3.3 4-pulse stacker scheme

To obtain greater flexibility in pulse design, we built a 4-pulse stacker that can provide four pulses of variable energy and variable inter-pulse separation. The optics setup is shown in Fig. 2.8. The original Nd:YAG beam is split into two beams after the first beam splitter (BS1); one beam goes directly to the second beam splitter (BS2), and the other one is directed to an 0~8ns optical-delay line, after which it goes to splitter BS2. At BS2 each beam is split again. One beam is directed to a 0-5ns optical-delay line and the other passes through a half-wave plate (HW2), which changes the beam polarization to vertical. After BS2, two beams in the same direction with a specific time delay go through HW2 without further time delay. However, the other two beams are directed to the second optical-delay line. All four beams are then recombined at a thin-film polarizer (TFP), after which they proceed collinearly to the experimental chamber. To have a variable energy distribution among the four pulses, different neutral-density filters were used in each beam path.

2.4 Experimental Chamber

The Nd:YAG pulses are focused collinearly with *f*/3 optics into a spray-droplet jet located in a vacuum chamber. The schematic diagram of the experimental vacuum chamber is shown in Fig. 2.9. The vacuum chamber is normally maintained at a

vacuum of 10^{-3}torr with the spray jet off and at 10^{-1}torr with the spray jet on, using a high-speed displacement (351cfm) roots pump (Leybold RUVAC WS/WSU 501) backed by a mechanical rotary pump. The pressure inside the chamber was measured using a Baratron absolute-pressure transducer (MKS Instruments Model 626A). The laser-plasma interaction region is roughly equivalent to the cylindrical volume, whose length and width are the confocal parameter and focal spot diameter of the laser, respectively [16]. In our case, the focal spot radius is w_0 =16.2 μ m, and the confocal parameter is $2z_0 = 2\pi \frac{w_0^2 n}{\lambda_0}$ ~1.5mm, where n is the refractive index of the medium, λ_0 is the vacuum wavelength, and w_0 is the laser beam minimum waist. The peak intensity of the laser pulse is in the range of 10^{13} to 1.5 x 10^{15} W/cm^2 corresponding to pulse energy in the range 4mJ to 600mJ. The hot plasma emits the EUV and soft-x-ray sources in all directions. The central wavelength of the emission spectrum and the emission time duration are strongly dependent on the laser pulse formatting, laser energy, laser wavelength, target species, as well as target geometry.

The laser-droplet plasma is diagnosed with an x-ray detector, a grazing-incidence EUV spectrometer, weak laser-probe pulses, and visible-imaging diagnostics. The x-ray detector was located at an angle of 135^0 with respect to the laser-propagation direction and 12.5cm from the interaction region; it is used to monitor any x-ray signal with an energy higher than 1.5keV. EUV emission from the laser-heated target is collected by a rhodium-coated paraboloidal condenser at 90 degrees from the laser axis shown in Fig. 2.10 and focused onto the entrance slit of a grazing-incidence EUV spectrometer. The details of the spectrometer are given in the next sub-section (Section

2.4.1). By using such a condenser, the effective collective solid angle of the spectrometer is increased by a factor of as much as 1600 [16]. To ensure that all the pulses from the 2-pulse or 4-pulse trains are collinear through the target region, we set up a side-imaging system and an end-imaging system for beam alignment.

2.4.1 EUV Spectrometer

In the EUV range, we recorded spectra with a grazing-incidence vacuum spectrometer (Acton GIMS-551.5), that gives us access to the wavelength range of 2 to 44nm with fine resolution better than 0.015nm (given 10 μm wide slits). It operates as follows: a concave diffraction grating with a grazing-incidence angle of 88 degrees, 1.5m radius and 1200grooves/mm, diffracts and images the spectrum from the entrance slit onto the grating focal surface, or Rowland circle [24]. A windowless electron-multiplier tube (PMT) (Thorn EMI EM226) with a BeCu first dynode is mounted on the exit-slit housing, which is driven by a stepper motor along the Rowland circle. Spectra are obtained by scanning the exit slit. A photograph of the spectrometer is shown in Fig. 2.11. A vacuum-isolation valve is located in the entrance-slit assembly to isolate the slit chamber from the main vacuum chamber. A separate turbo-molecular high-vacuum pump is used to maintain the vacuum as low as 5 x 10^{-8}torr with the entrance slit closed and 9 x 10^{-5}torr with the entrance slit open and the droplet jet operating at 10Hz for this spectrometer.

2.4.2 Imaging

To ensure the precise overlap of the beam paths of the experimental laser pulses, side imaging of laser scattering from the plasma and end imaging of the focal spots of laser pulses were monitored and captured, using two separate CCD cameras. The optical layout of the side-imaging system is shown in Fig. 2.12(a). It was set up as follows: an f/3 lens was located at 90^0 from the laser-propagation direction and 275mm away from the laser-droplet interaction area, and the CCD camera sat 350mm away from the lens. The linear magnification was 1.27. A light bulb with ~1.5mm long filament was used at the object position to align the side CCD image system. To precisely align the laser pulses collinearly, an end imaging system was set up to monitor the overlap of the focal points of the pulses. The optical layout is shown in Fig. 2.12(b). The laser-droplet interaction area was relayed to the CCD camera with a f/3 and f/6 lens pair, the f/3 lens was oriented along the beam axis and 150mm behind the target object. The second lens was positioned to have the common focus point position with and 450mm away from the first one, the CCD camera was sitting 300mm away from the second lens. A 20X magnification microscope was used to align the overlap of the pulses extremely precisely. The total effective magnification is 40X.

2.4.3 X-ray detector

The laser-droplet interaction not only generates the EUV, but also x-rays (wavelengths <10nm). To better understand the physics behind the laser-droplet interaction mechanism, the emission of x-ray photons was also monitored. A $1cm^2$

silicon photodiode (IRD AXUV-100) coated with a 150nm-thick aluminum (Al) filter performs as a high-pass photon filter to eliminate visible background light and IR background light from the laser itself and the plasma source. The diode output was amplified by a current-to-voltage amplifier. The setup was enclosed in an aluminum can to shield against electromagnetic-noise pulses induced by the laser-plasma generation. A 25μm-thick beryllium (Be) filter formed the front window of the can, which acted as a high-pass filter for x-rays above ~1.5keV, and also completed the electrical shielding. Fig. 2.13 shows plots of the effective transmission curve as a function of incident-photon energy for the Be filter and Al filter, respectively. The transmission characteristics are predominantly those of the Be filter with the small sharp feature at 1.49keV because of K_α edge from thin Al coating on the photodiode.

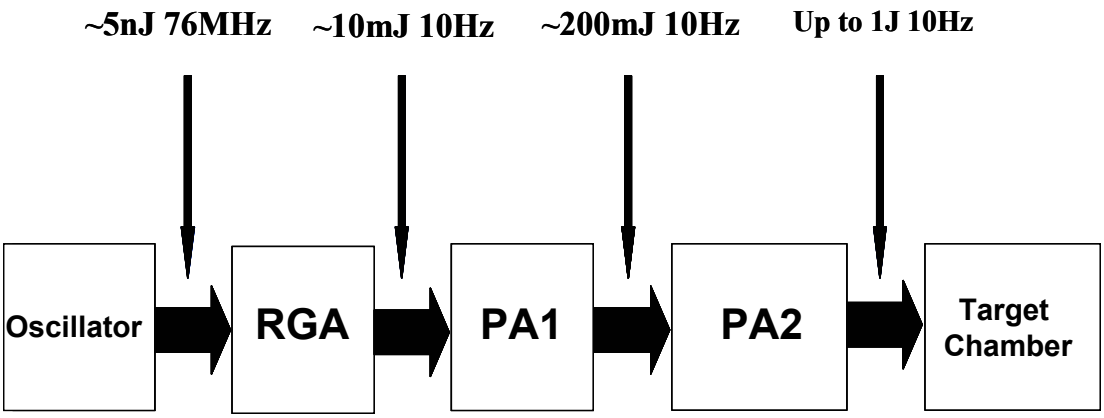

Figure 2.1: Block diagram of output energy of our 10Hz 1064nm 100ps Nd:YAG intense pulsed laser system.

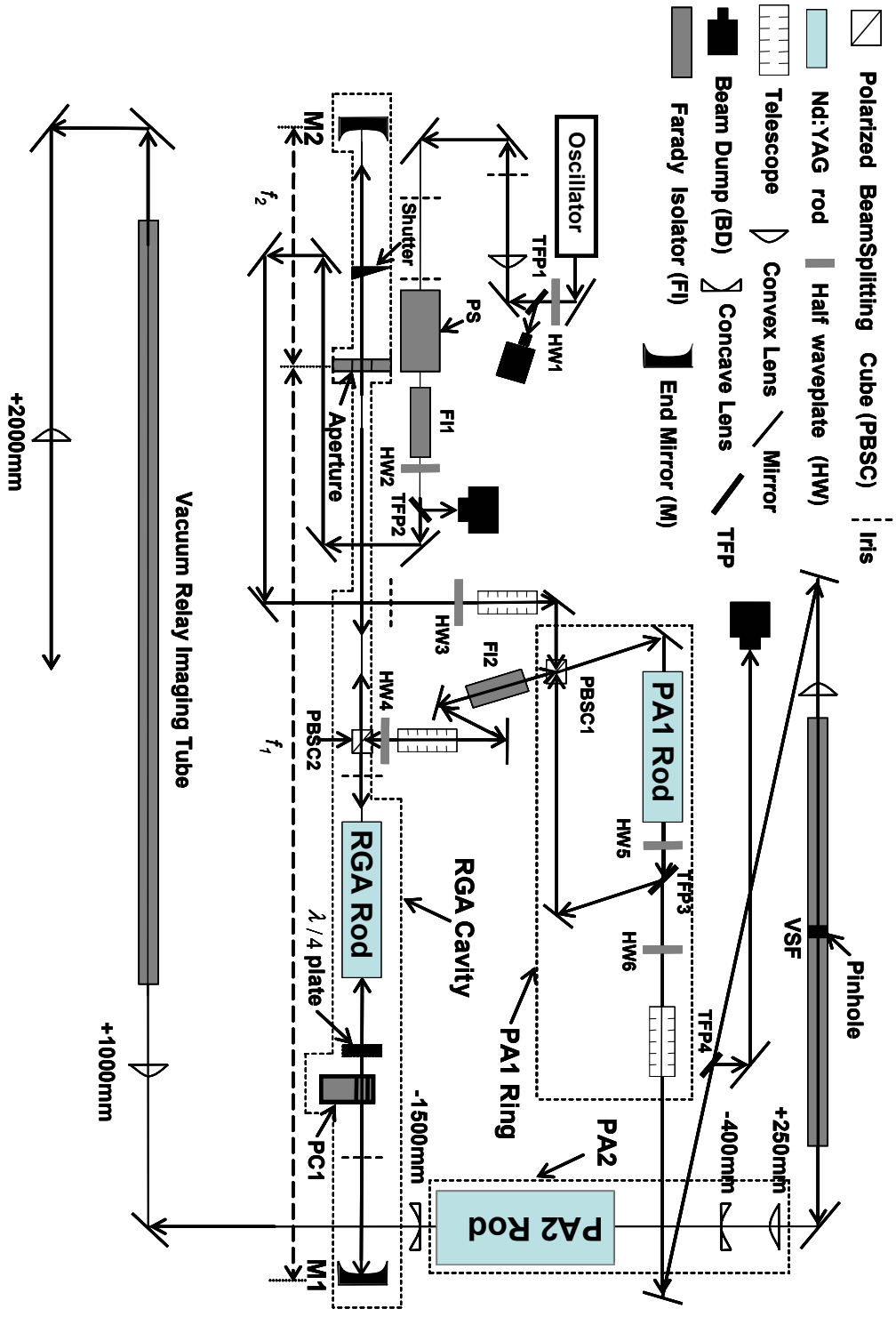

Figure 2.2: Detailed optical layout of our 10Hz 1064nm 100ps Nd:YAG intense pulsed laser system.

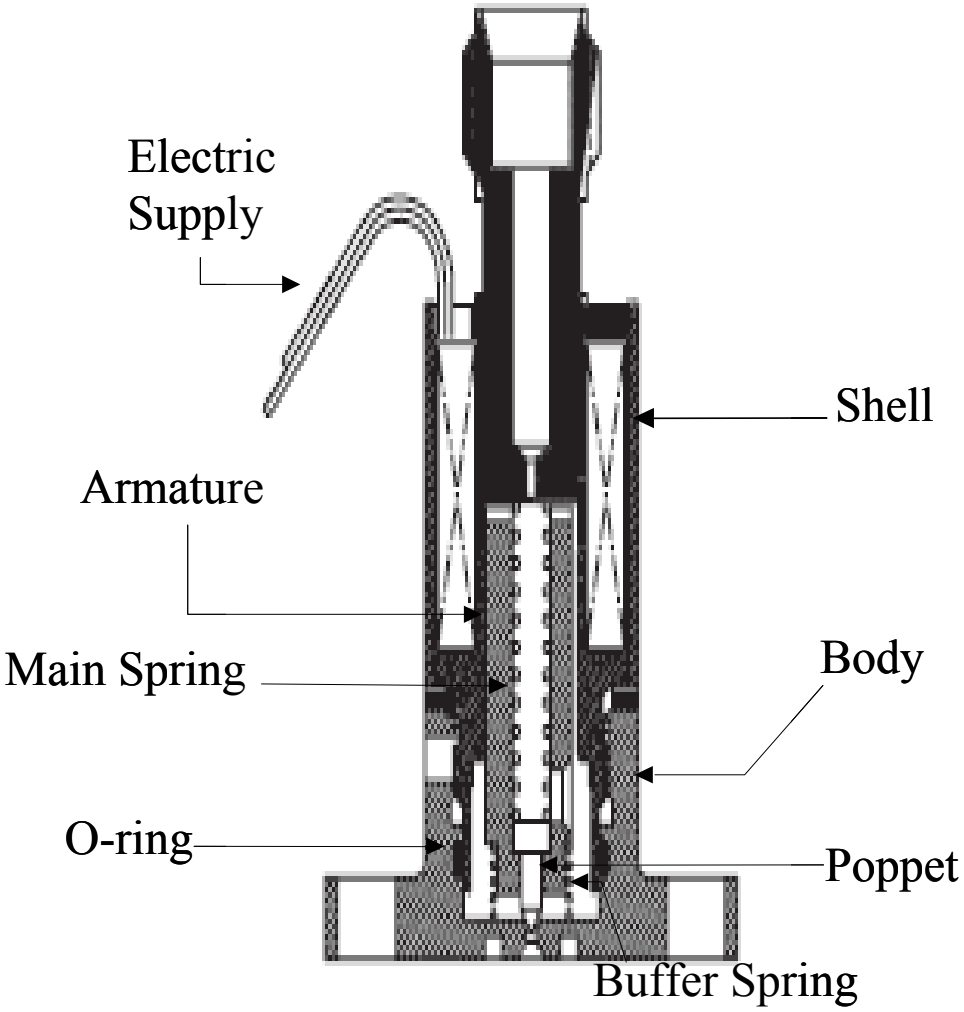

Figure 2.3: Schematic diagram of cryogenic ultra high vacuum solenoid valve.

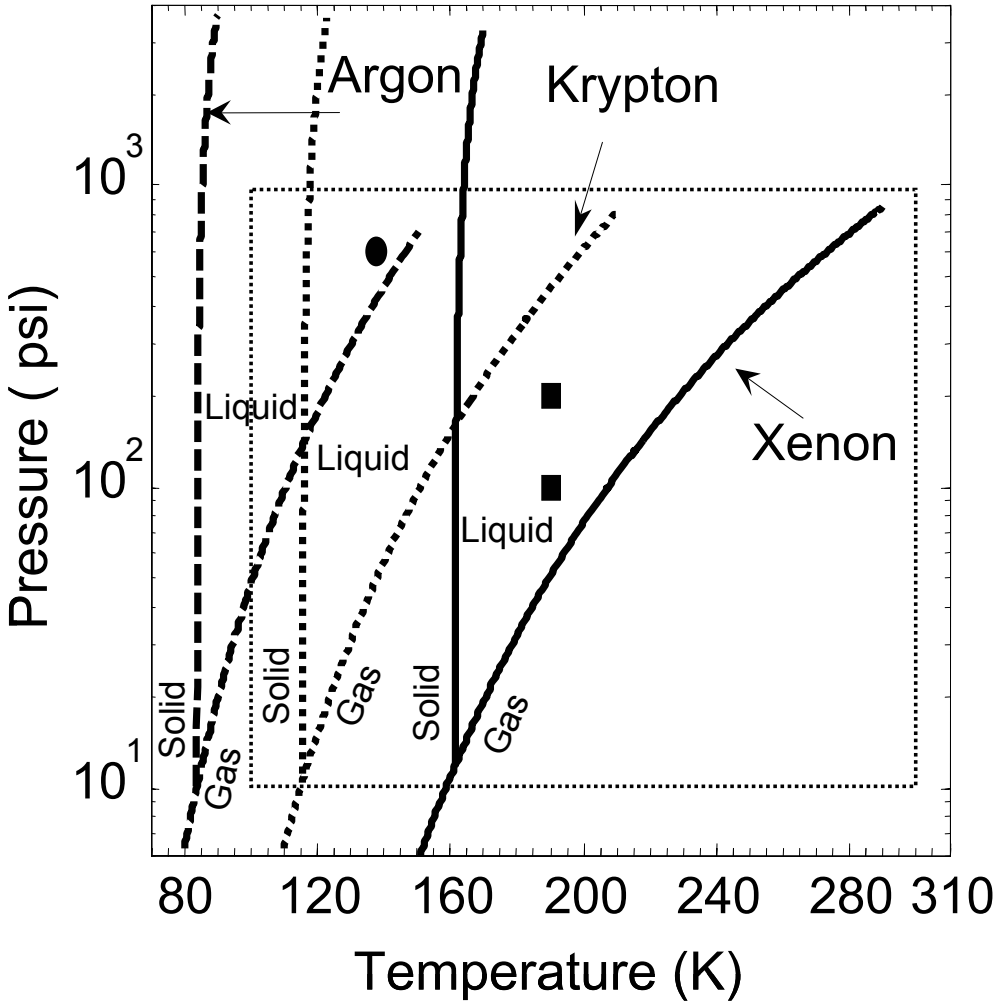

Figure 2.4: Argon, krypton and xenon phase diagrams laid over the pressure and temperature range of our nozzle system. The black dot corresponds to our experimental condition for argon droplets. The black solid rectangles correspond to our experimental conditions for xenon droplets.

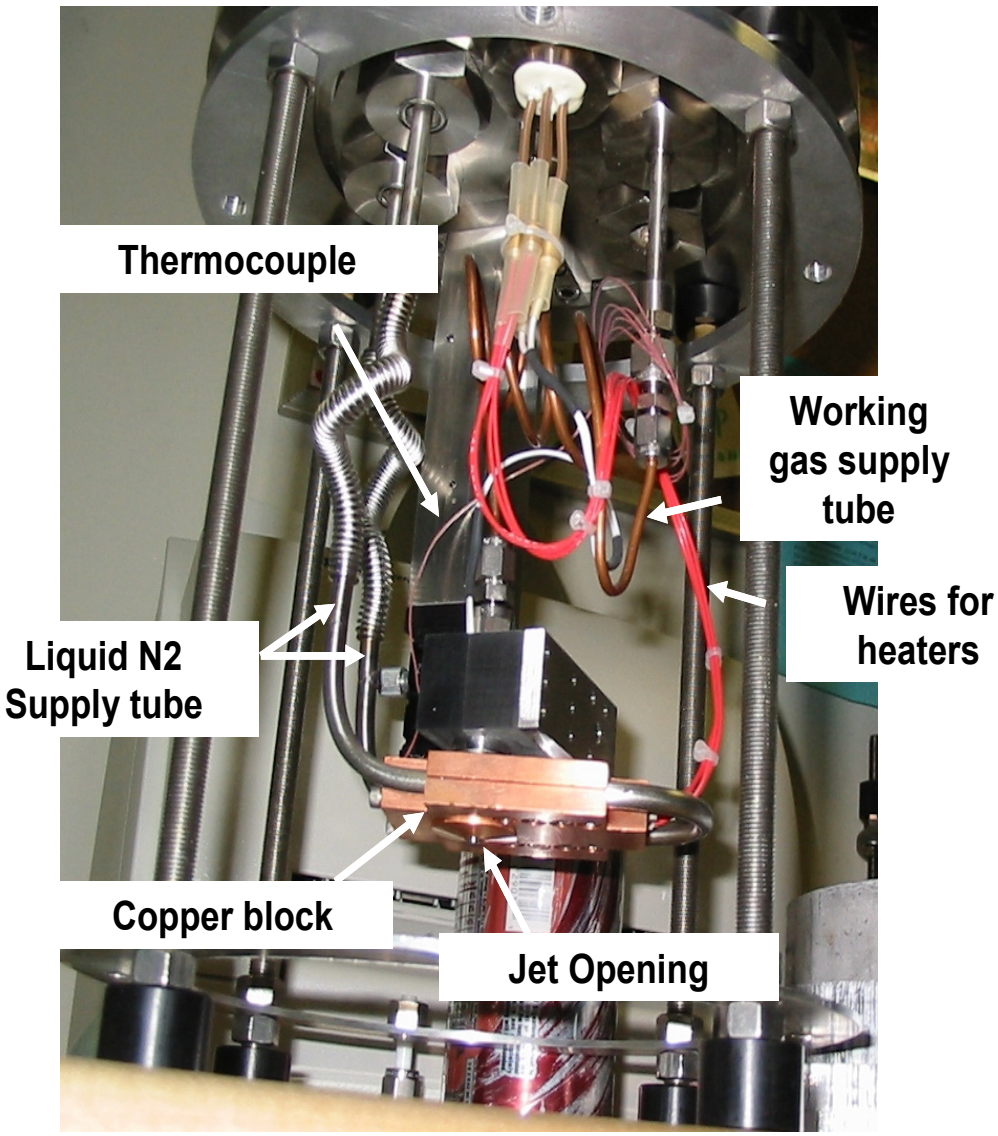

Figure 2.5: Photograph of the gas jet assembles showing all the components arrangements.

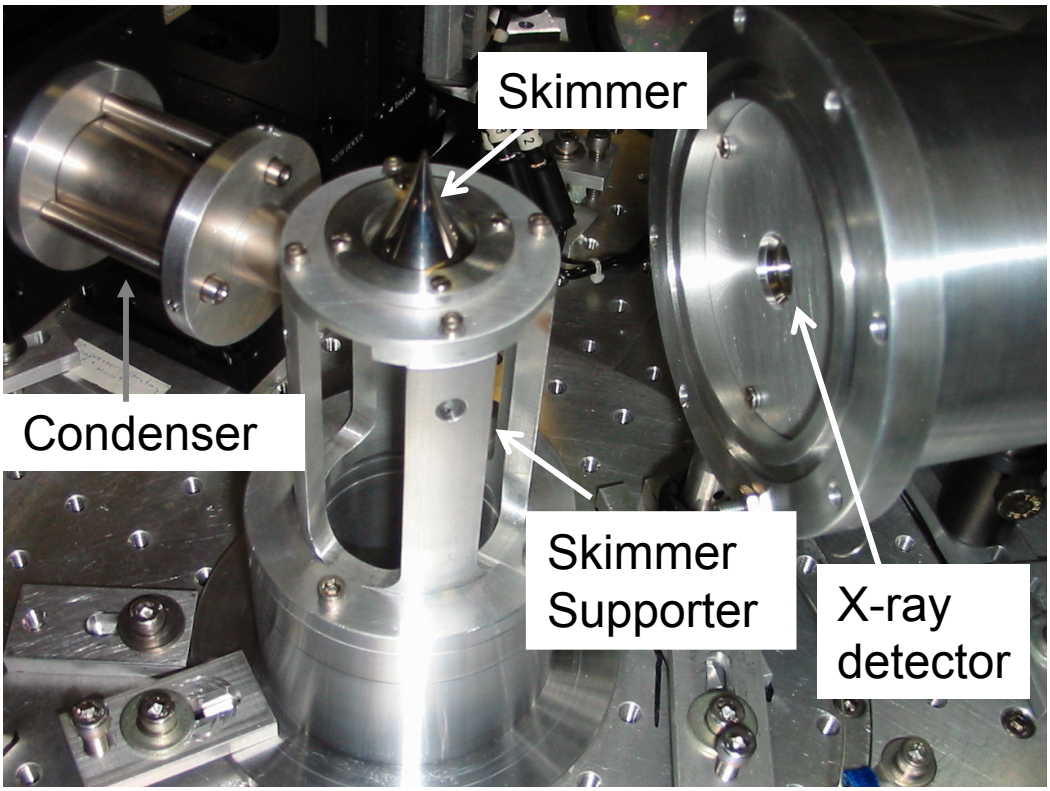

Figure 2.6: Photograph of skimmer with its supporter along with condenser and X-ray detector.

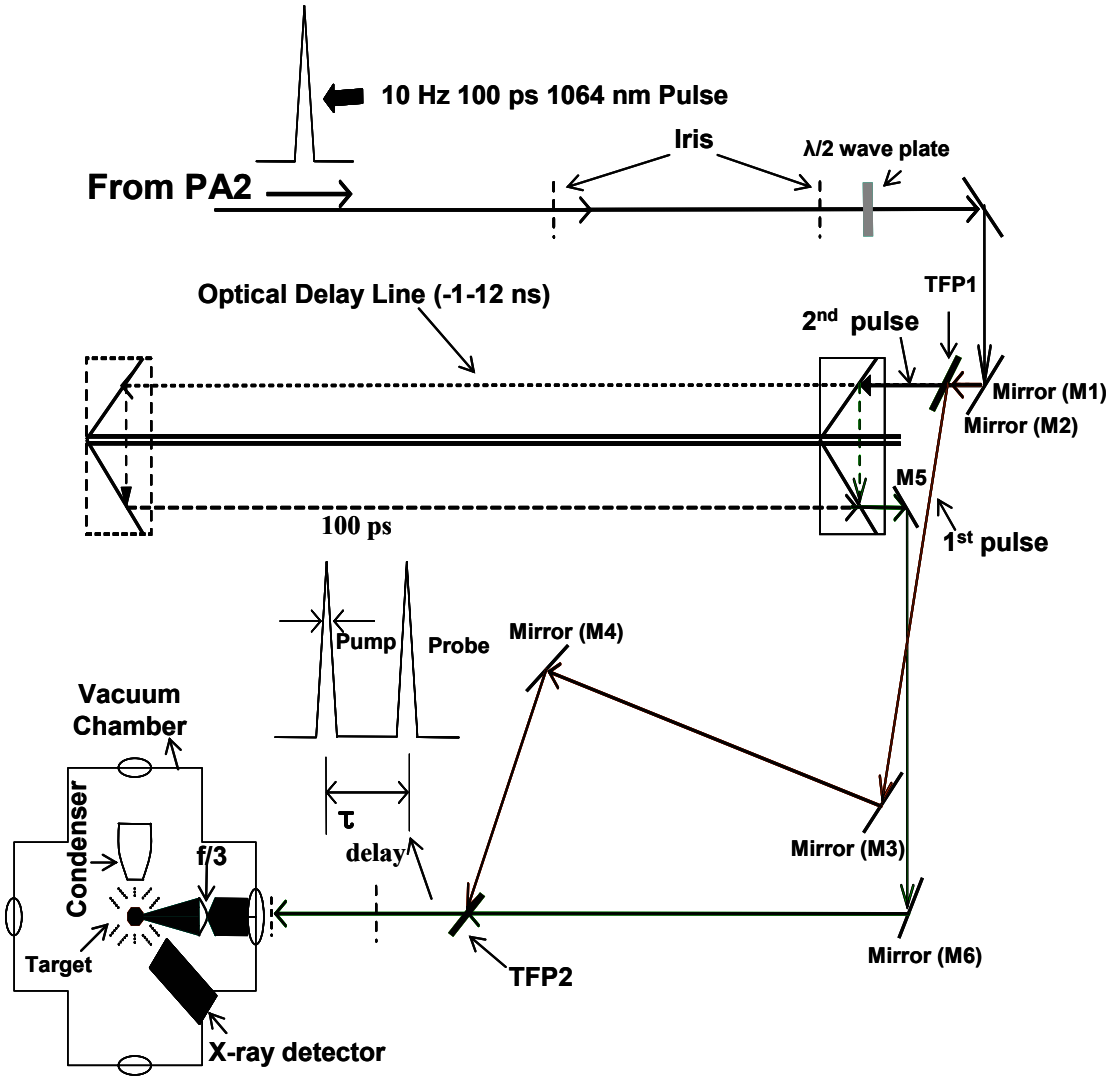

Figure 2.7: Experimental setup of optical layout of pump probe scheme.

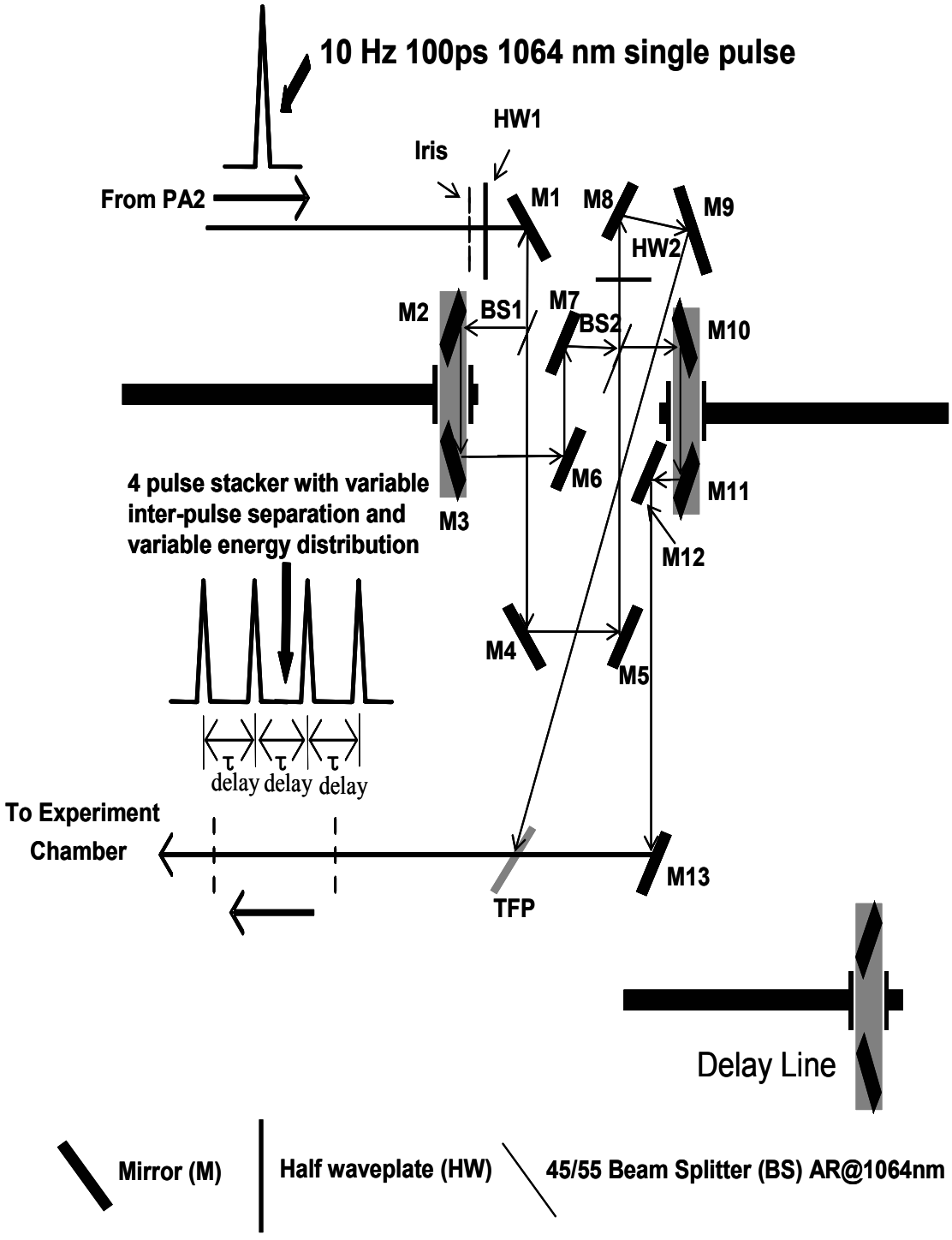

Figure 2.8: Experimental setup of optical layout of 4-pulse stacker scheme.

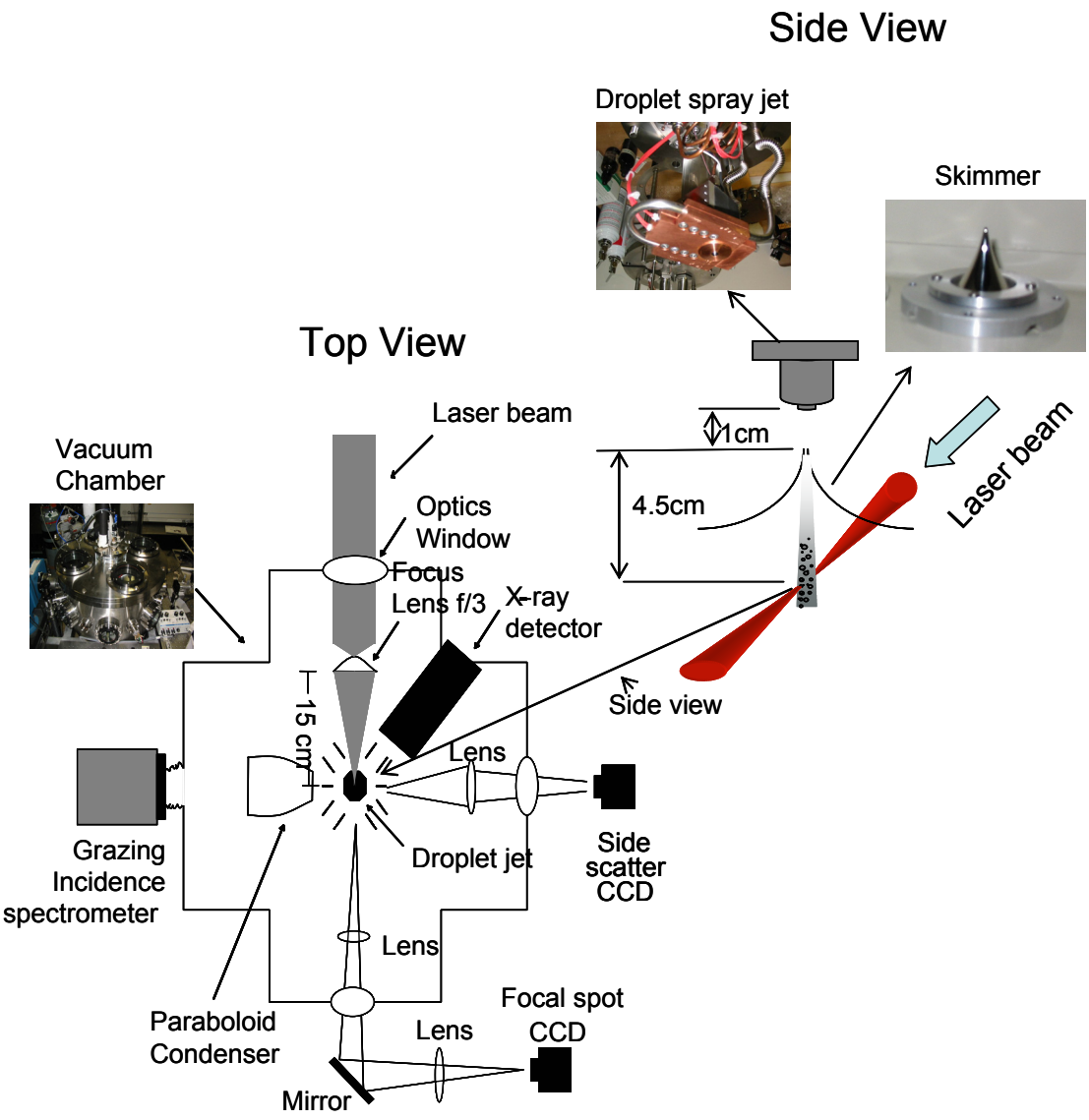

Figure 2.9: Schematic diagram of top view and side view of experimental vacuum chamber.

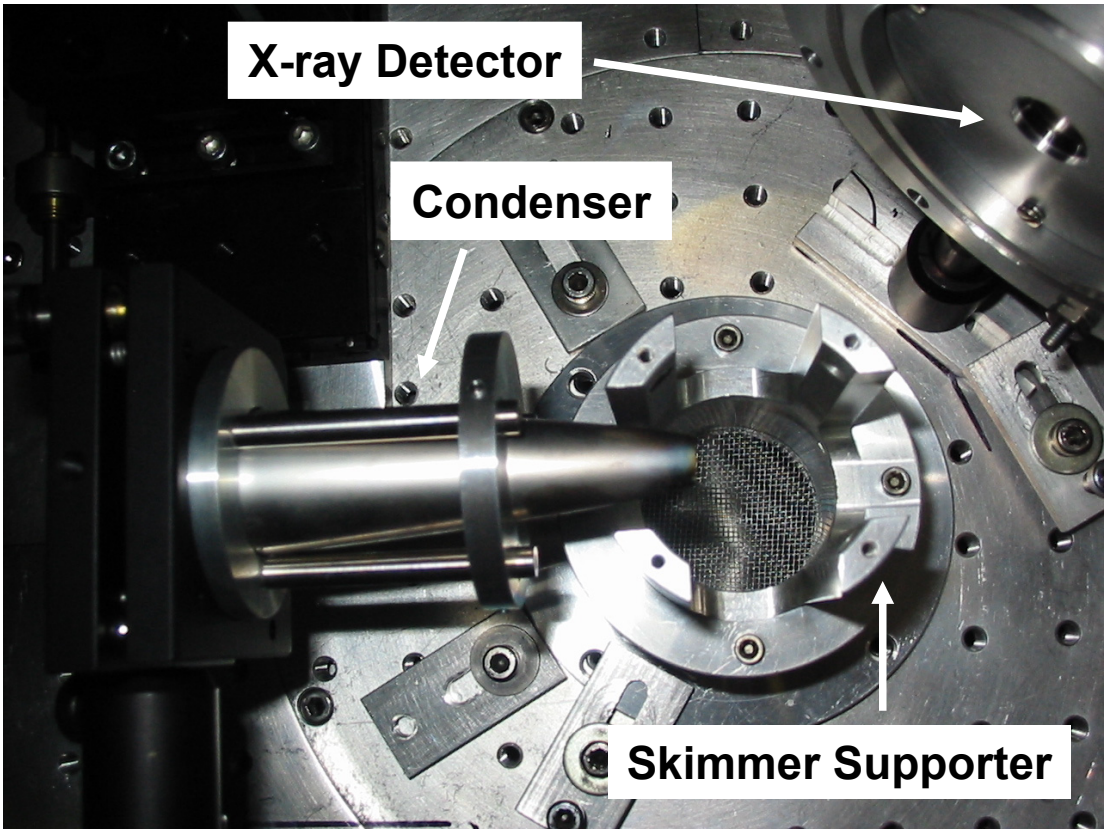

Figure 2.10: Photograph of rhodium-coated paraboloidal condenser.

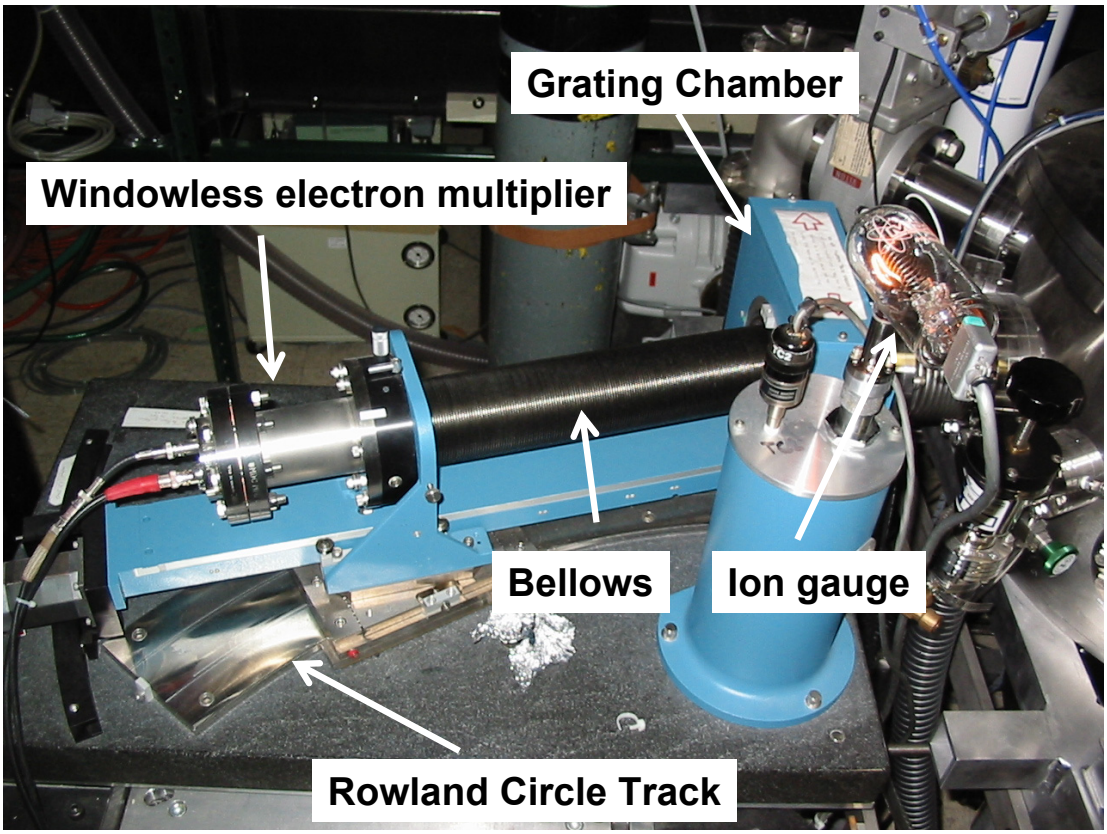

Figure 2.11: Photograph of Acton (GIMS-551.5) grazing incidence spectrometer.

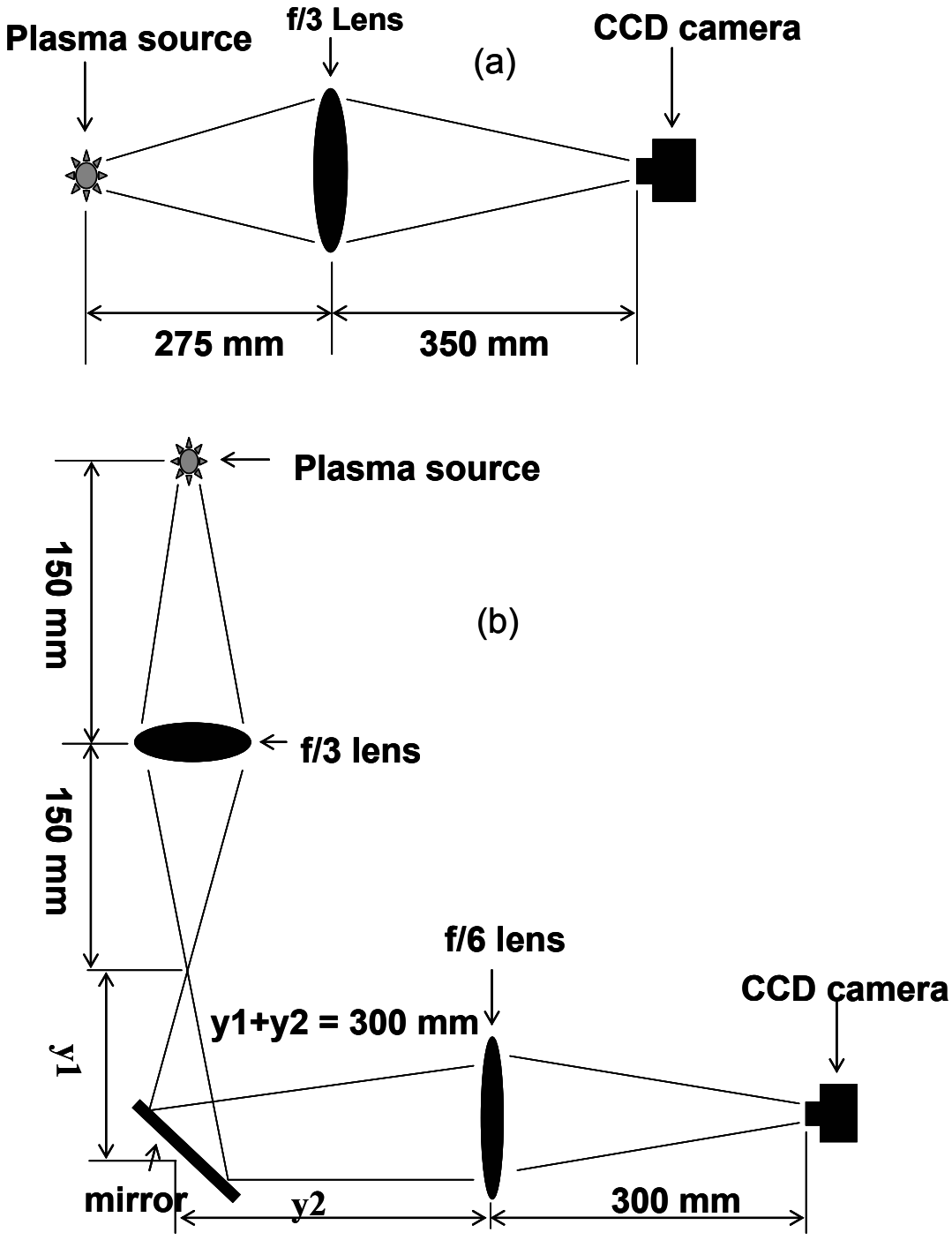

Figure 2.12: (a) Schematic optical layout of side imaging system with magnification of 1.27. (b) Schematic optical layout of end imaging system with total effective magnification of 40X.

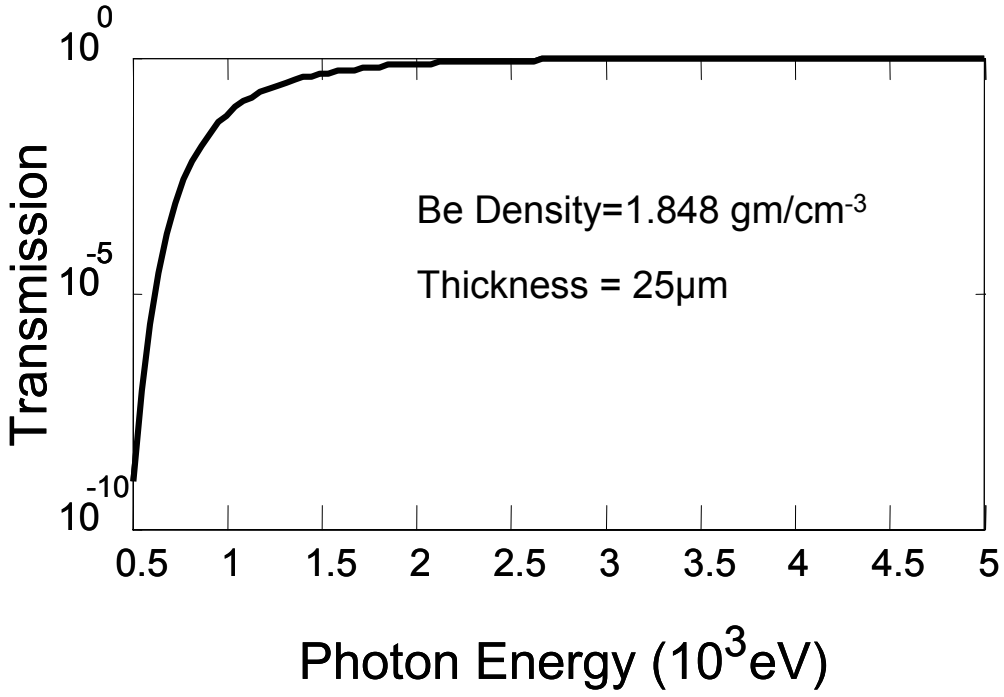

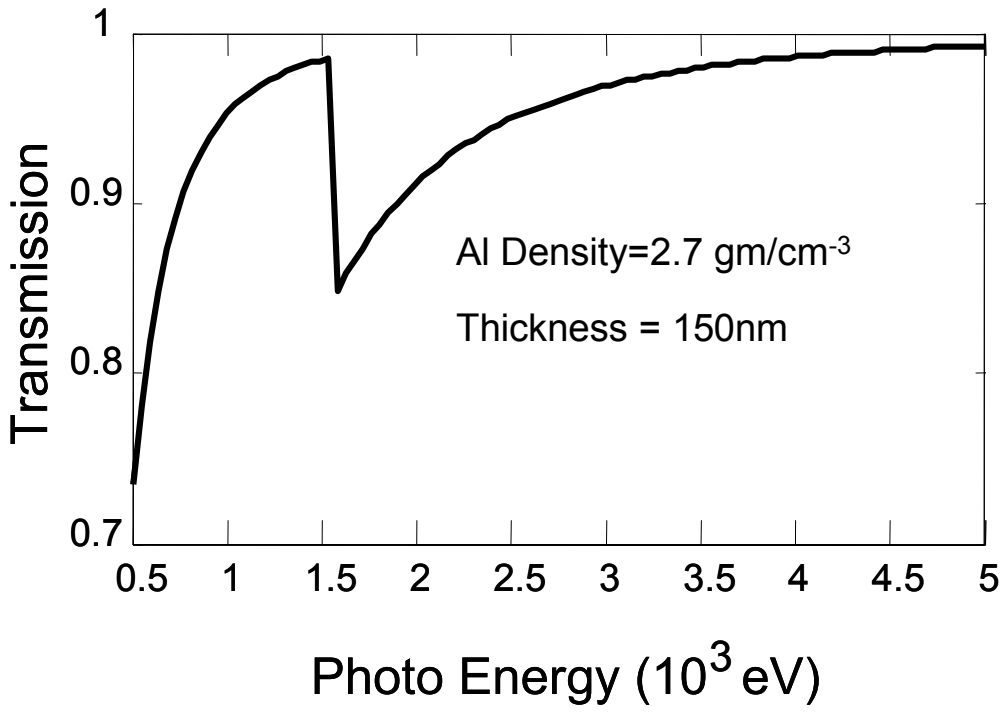

Figure 2.13: The transmission curve versus photon energy for (a) 25μm Beryllium filter and (b) 150nm Aluminum filter.

Chapter 3: EUV Efficiency Experimental Results

3.1 Results with Argon Droplets

As there is no gas recirculation system on our setup, argon gas was used mainly to reduce the cost of the experiment and to allow extensive streamlining of our data acquisition and analysis. More importantly, it provided a good comparison and physical insight to understand the xenon-droplet experiments.

The earliest work by our group was performed with argon-liquid droplets, using the well-characterized cryogenic droplet-source discussed in Chapter 2. The laser-droplet plasma is diagnosed with an x-ray detector, a grazing incidence EUV spectrometer, weak laser-probe pulses, and visible imaging diagnostics. A more complete description of the diagnostics can also be found in Chapter 2. We found that argon droplets present a special case in which the ionization stage distribution is "robust" [1]. In argon, for example, the ionization potential of Ar^{7+} is about 140eV, while for Ar^{8+}, it is ~420eV. Thus, providing sufficient laser power to heat the plasma to the 8+ ion stage of argon is relatively easy (it requires approx. 50eV thermal electron temperature). Supplying excess power, however, does not lead to a large onset of Ar^{9+} population because of the large gap in ionization potential. Thus, an ionization distribution dominated by Ar^{8+} can be achieved over a wide range of laser powers and temporal/spatial laser-power distributions. In fact, no Ar^{10+} emission lines were observed in our experiments. The "robust" population of Ar^{8+} ions serves as a reservoir

from which either recombination proceeds to Ar^{7+}, with resulting recombination emission, or from which electron collisional excitation or ionization results in relatively weaker emission from either Ar^{8+} or Ar^{9+} excited states [1]. The situation is similar for krypton, except that the "reservoir" ion is Kr^{10+} [1]. So, at least for species that achieve stable or robust ionization distributions, maximizing spectral yields from features associated with an excitation process requires laser heating to occur when the droplet is at or above the critical electron density—when heating efficiency is greatest. Under those conditions, the optimal laser-pulse duration is set mainly by droplet size, and is less than a few hundred picoseconds for a ~10μm droplet [1-2]. If the desired spectral feature is associated with recombination, the condition is relaxed, and the most EUV-efficient laser-pulse duration is generally longer. In that case, it is determined by achieving at least several recombination cycles, and it can be in the few-nanosecond range [1].

The 16.6nm and 26.0nm EUV-emission yields in argon-droplet target corresponding to Ar^{9+} transition of $2s^22p^5$-$2s2p^6$ [3] and Ar^{7+} transition of $2p^63d$-$2p^64f$ [3], respectively, are reported in this dissertation. We focused on those two lines because in our laser-power range, Ar^{8+} is the main ionization stage as discussed above, therefore the two lines that are primary emission lines from Ar^{9+} and Ar^{7+} will be the direct reflection of the two different types of emission of interest: excitation emission and recombination emission. In our case, a valve temperature of 138K and backing pressure of 600psi were chosen to run for argon droplets. Under those conditions, the average argon-droplet size is ~4.8μm [4]. Figure 3.1 shows the location on the argon phase-diagram of the liquid operating region for our spray jet. A

single laser-pulse with an energy of 600mJ generated a sample EUV spectrum ranging from 2-44nm spaced by 0.05nm as shown in Fig. 3.2. Fifty shots were averaged for each data point along the spectrum. The peak emission in the spectrum occurs at 26.0nm. The emission of the 16.6nm line was also observed but relatively weaker. No Ar^{10+} emission lines were observed. This implies that the large onset of Ar^{9+} population did not occur but an ionization distribution dominated by Ar^{8+} was achieved under these conditions. With a fixed total energy of 600mJ, two-pulse heater experiments were studied to explore whether heating from the second pulse at a different arrival time can enhance laser-to-EUV conversion efficiency. The EUV yields versus pulse temporal separation with each pulse 300mJ are shown in Fig. 3.3-3.4, corresponding to the 16.6nm line emission and 26.0nm line emission with bandwidth of 0.1nm, respectively. At each delay, the total EUV yields integrated over time from pump plus probe together were captured first corresponding to EUV yield from pump + probe in the figures. Then at the same delay, probe was blocked, the EUV yields integrated over time from pump alone were collected corresponding to EUV yield from pump alone in the figures. The EUV yield from extracted probe in the figures corresponds to the total EUV signal from pump plus probe subtracted from that from pump alone. Five hundred shots were averaged for each data point. The negative values of EUV yield from extracted probe for delays > 1ns could due to the high-power laser-energy fluctuation shot by shot in the experiment. In Fig. 3.3 the peak yields produced by the second pulse occurs at 400ps delay. In Fig. 3.4 the peak yields produced by the second pulse occurs at 200ps delay. The results suggest that different pulse temporal structure with the same fixed total laser energy can generate different

total EUV yields for argon droplets. That encouraged us to continue the pulse-formatting experiment with xenon droplets. Especially ~200-400ps separation between first pulse and second pulse produced more EUV yield at the 16.6nm and 26.6nm lines, compared with 0ps separation (two pulses temporally overlap, which is equivalent to a single pulse with double energy) under our experimental conditions. In the 4-pulse-stacker experiment with argon droplets, the 16.6nm and 26.0nm EUV yields from the three following pulses together versus the inter-pulse temporal separation are plotted in Fig. 3.5. In that experiment, the four pulses carried equal energy. By increasing the total laser energy from 100mJ (each pulse 25mJ) to 400mJ (each pulse 100mJ), we found that the peak EUV yields over various inter-pulse temporal separations always occurred at 200ps rather than at 0ps, and the total absolute EUV yields increased for all the inter-pulse temporal separations <0.4ns when total laser energy increased. Those results show that different pulse temporal structures could enhance the laser-to-EUV conversion efficiency by heating droplet plasma at an appropriate time point when more laser energy could be absorbed by droplet plasma.

In the next experiment, two pulses proceeding collinearly, each with 300mJ, were used to heat the argon droplets but with two different time-separation settings between the first pulse and the second pulse: 0ps and 200ps, respectively. Two separate sets of EUV spectra in the 2-44nm range, produced by double-laser-pulse heated argon-droplet plasma corresponding to the above two time delays, were acquired. The two sets of EUV spectra are plotted in Fig. 3.6. The dashed line is the argon-droplet spectrum corresponding to the case of separation of 200ps between the

first pulse and the second, and the solid line is the argon-droplets spectrum corresponding to the case of 0ps. The results show that more EUV yield is produced at the 200ps time delay than at the 0ps time delay for the full spectra range of 2-44nm. The averaged enhancement is approximately 1.5 times. That implies that laser energies from consecutive pulses are more efficiently coupled into argon droplets.

3.2 Xenon-Droplet Size and the EUV Spectrum

We first measured the sizes of xenon droplets under selected experimental conditions (valve backing-pressure and temperature: 100psi/190K and 500psi/240K). The measurements were made using the dark-field shadowgraphy technique shown in Fig. 3.7. In our experiment the optical technique was accomplished using a two f/3 lens pair and an obstacle located at the mutual focus of the lens pair. Low-intensity collimated third-harmonic laser pulses (355nm, 60ps) from the Nd:YAG laser system were shined on the droplet target, a portion of the laser light passed through the droplets without scattering and was focused by the first lens, and therefore, completely blocked by the obstacle. The remaining light was scattered by the target. The scattered light, which carried the information of the target, was collimated by the first lens and was then refocused by the second lens to form an image. The obstacle at the mutual focus did not perturb the scattered light very much. The image of the droplets was then magnified and relayed to a CCD camera with a microscope lens. The goal was to backlight and photograph the droplets-object while suppressing the strong background light. The contrast of the image was greatly enhanced by removing the low-order Fourier components, corresponding to the unscattered portions of the

irradiating laser pulses. The resulting images show the droplets as bright objects against a dark background. A skimmer with a 0.5mm-diameter orifice 2mm below the jet was used to isolate a thin (~2mm diameter) droplet stream in order to avoid multiple scatterings. The laser-droplet interaction region was a total distance of 63mm downstream from the valve orifice. The system's resolution limit (defined as the distance for a 10-90% intensity change in the image of a hard edge) was ~1.5μm (determined by using a resolution target). As a result, the smallest resolvable droplet diameter was about 3μm [5]. The experimental valve temperature and backing-pressure conditions, corresponding to our xenon-droplet size-measurement experiment, are marked on the xenon phase-diagram shown in Fig. 3.8(a). The insets are side-scattered images of a droplet stream, corresponding to two different conditions on the phase-diagram. The droplet-size distribution is plotted in Fig. 3.8(b). The scale is from several μm to ~10μm. In general, we have demonstrated the control of average droplet sizes through feedback control of our valve backing-pressure and temperature [2]. Typical xenon-droplet diameters under our conditions range from ~5-20μm. A valve backing-pressure of 100psi and a temperature of 190K were used for the following experiments for the sake of saving xenon. Under such conditions, the average xenon-droplet size is ~7.4μm.

A single pump-pulse induced EUV spectrum near 13.5nm is shown in Fig. 3.9 for pulse energy of 200mJ. Fifty shots were averaged for each data point in the spectrum with $\Delta\lambda$ of 0.05nm. It can be seen that the peak emission is near 11nm. In the range from Xe^{4+} to Xe^{13+}, which could be the main ion species relevant to EUV process in the 10-14nm spectral range [6], the peak emission of around 11nm

corresponds to 4*f*-4*d* transition arrays of Xe^{9+}~Xe^{12+} and 4*d*-4*p* transition arrays of Xe^{7+}~Xe^{12+} [7-9]. That implies that higher-order ionized xenon-ions (Xe^{11+}, Xe^{12+}) rather than the expected ions (Xe^{10+}), corresponding to 13.5nm emission [10], could be the dominant ions. To investigate how the spectrum is dependent on the laser energy, the pulse energy was varied. A plot of the xenon-droplets EUV spectrum versus laser-pulse energy is shown in Fig. 3.10. The dashed baselines are the signal levels with the laser pulse off. The total spectral yields increase when the laser energy increases.

3.3 Pulse-Formatting Results with Xenon Droplets and Discussion

In successive experiments to look into pulse-formatting, we first used the 2-pulse heater scheme. The plot of the EUV yields at the 13.5nm-line emission with bandwidth (BW) of 0.27nm (2%) from the pump (200mJ) plus probe (200mJ) together, pump alone, and extracted probe versus the delay time between the pump and probe pulse is shown in Fig. 3.11. The pulse-to-pulse EUV yield from the pump alone was almost constant, having very small fluctuation (~5%) during the experiment. That indicated that experiment conditions—such as laser energy of each shot, valve temperature, backing pressure of the gas reservoir, and the average droplet properties—were stable during the experiment. From the plot, the EUV yields at the emission line of 13.5nm produced by the probe are always greater than that produced by the pump for delays shorter than 4ns. That implies that to efficiently generate 13.5nm EUV in the 2% BW, the single 400mJ 100ps pulse is less optimal than the two 200mJ pulses separated with <4ns delay. The peak emission occurs at 1ns delay.

At that delay, the yield from the extracted probe is approximately double that from the pump alone.

Next, we compared the EUV yields by varying the total energies of the pump and the probe, while keeping their energy equal. The comparison of the EUV yields from the extracted probe—between the case of a total energy of 200mJ (pump 100mJ and probe 100mJ) and the case of a total energy of 400mJ (pump 200mJ and probe 200mJ) —is plotted in Fig. 3.12. It is clearly seen that the peak emission vs. delay is shifted to earlier times when the laser energy decreases. For the case of a 100mJ pump and 100mJ probe, the peak emission occurs at ~200ps time delay, much shorter than the 1ns delay that was optimum for the case of a 200mJ pump plus a 200mJ probe. Thus, the emission peak is dependent not only on the delay time, but also on the total energy of the split pulses. For both cases, the probe always produces more EUV yield (13.5nm) at their optimum delays than at the delay of 0ns. The averaged enhancement is ~1.74 times for the case of a 100mJ pump and 100mJ probe and is ~1.63 times for the case of a 200mJ pump and a 200mJ probe. The efficiency of the EUV yield of 13.5nm drops slightly (from 1.74X to 1.63X) while the energy increases from 100mJ/100mJ to 200mJ/200mJ. Because the cooler plasma is more absorptive, the later case (100mJ/100mJ) cools sooner compared with the first case (200mJ/200mJ), since there is less heating.

We next explored EUV-emission efficiency with a more complex 4-pulse-stacker scheme. The four pulses were arranged with a uniform energy distribution and with the same time delay between successive pulse pairs. The total laser energies used in this experiment were 100mJ, 200mJ, and 400mJ, respectively. The plots of the

total EUV yields at 13.5nm from the three following pulses (subtracting the contribution from the first pulse) versus the inter-pulse time-separation for various total energies are shown in Fig. 3.13. With a total laser energy of 100mJ, the EUV yield decreases as the inter-pulse time separation increases. With the total laser energy of 200mJ, the peak EUV yield occurs at 200ps of inter-pulse separation; while it occurs at 0.8ns when the total laser energy is 400mJ. Our results for the 2-pulse and 4-pulse cases suggest that, unlike earlier experiments with argon and krypton droplets, the ionization-state distribution in Xe may be much more transient. The decay timescale for 13.5nm line emission is approximately 0.5-1.5ns, a timescale intermediate to the results from excitation and recombination emission in Ar and Kr droplet targets.

Compared with argon, the ion stage responsible for emission at 13.5nm, Xe^{10+} [10], is in a very transient state in the plasma. That is because, unlike the relatively robust ions Ar^{8+}, Xe^{10+} is close in ionization potential to surrounding 8+, 9+ and 11+, 12+ ions. For example $Xe^{9+} \rightarrow Xe^{10+}$ requires ~20eV, and $Xe^{10+} \rightarrow Xe^{11+}$ requires ~30eV [6]. At typical plasma temperatures of a few 10s of eV, it is easy to pass through Xe^{10+}. So, while laser overheating in Ar is tolerated, because the distribution tends to stabilize with an accumulation at the 8+ stage, the Xe ionization distribution will be much more sensitive to laser parameters. In addition, local plasma spatial and temporal variations in temperature would influence the ionization distribution to a greater extent than in a robust system. While the ideal situation would be to have a steady state population of Xe^{10+}, that fills a large fraction of the source volume, in practice that condition may be difficult to engineer.

3.4 Conclusions and Future Work

In this experiment, we explored laser-pulse formatting for enhancing laser-to-EUV conversion efficiency in the 13.5nm band. Droplet sources were studied as the laser target. First, we measured the xenon-droplet size distribution, and we scanned the droplet-plasma spectra with various laser energies under our experimental conditions. In successive experiments with pulse-formatting, we used 2-pulse and 4-pulse heater setups. We found that two laser pulses separated in time by several hundred picoseconds are more suitable for efficient generation of EUV at the 13.5nm line than a single pulse of the same energy. Our results suggest that, unlike earlier experiments with argon and krypton droplets, the ionization-state distribution in Xe may be much more transient. The decay timescales for 13.5nm emission are approximately 0.5-1.5ns, a timescale intermediate to the results from excitation and recombination emission in Ar and Kr droplet targets.

One approach in a next phase of work will be to try to maximize the lifetime of Xe^{10+} by repeatedly producing it in the interaction of a formatted laser pulse with a cryogenic Xe target. That is, even though plasma conditions may be difficult to attain for the long time steady appearance of Xe^{10+}, repetitive pulsing within the controlled substructure of a formatted laser pulse might transiently cycle the ion stage distribution repeatedly through Xe^{10+}, and at high enough density that the accumulated EUV emission at 13.5nm is significant.

It will be useful to continue to add pulses to the pulse stacker in order to have a wider flexibility in pulse design. A new 15ps pulse system with some grating-based geometric pulse stretching (with uncompensated transverse spatial chirp) will be

desirable to allow even more flexible use of pulse stackers than the current system. In order to have the most direct overlap with LPP source suppliers, it would be helpful to obtain or borrow a liquid-filament jet. Also, in order to be able to use multi-shot time resolved pump probe diagnostics, a cryogenic single-droplet source will be developed in the future, which can produce single constant-sized droplets at high repetition rates. Having such a source will drastically reduce our consumption of Xe.

The development of single-shot and multi-shot pump probe diagnostics for the plasma is also desirable. A single-shot diagnostic is needed for the spray jet, which has shot-to-shot fluctuations in the spatial distribution of droplets local to the probe and in the droplet-size distribution. The objective will be to use multiple probe pulses split from the main pulse. The probe pulses will be successively delayed with inter-pulse separations of no less than the laser pulse-width (100ps), and each pulse will be viewed with its own interferometric imaging system. In that way, a sequence of "framing" images can be collected in a single shot. We already have considerable experience with single-shot diagnostics in the femto-second regime [11]. For the single-droplet source, a standard multi-shot pump-probe interferometer will be used, as we have done in both the picosecond [12] and femtosecond regimes [13].

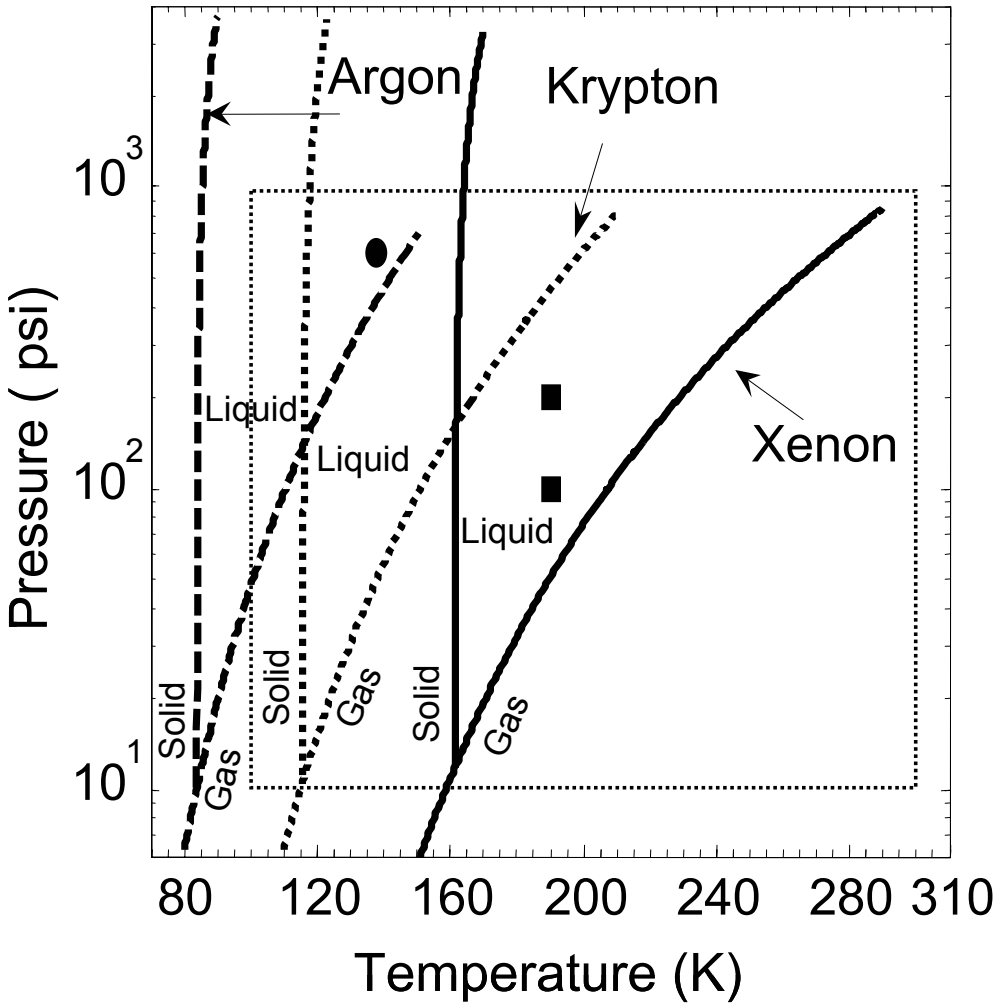

Figure 3.1: Argon, krypton and xenon phase diagrams laid over the pressure and temperature range of our nozzle system. The black dot corresponds to our experimental condition for argon droplets. The black solid rectangles correspond to our experimental conditions for xenon droplets.

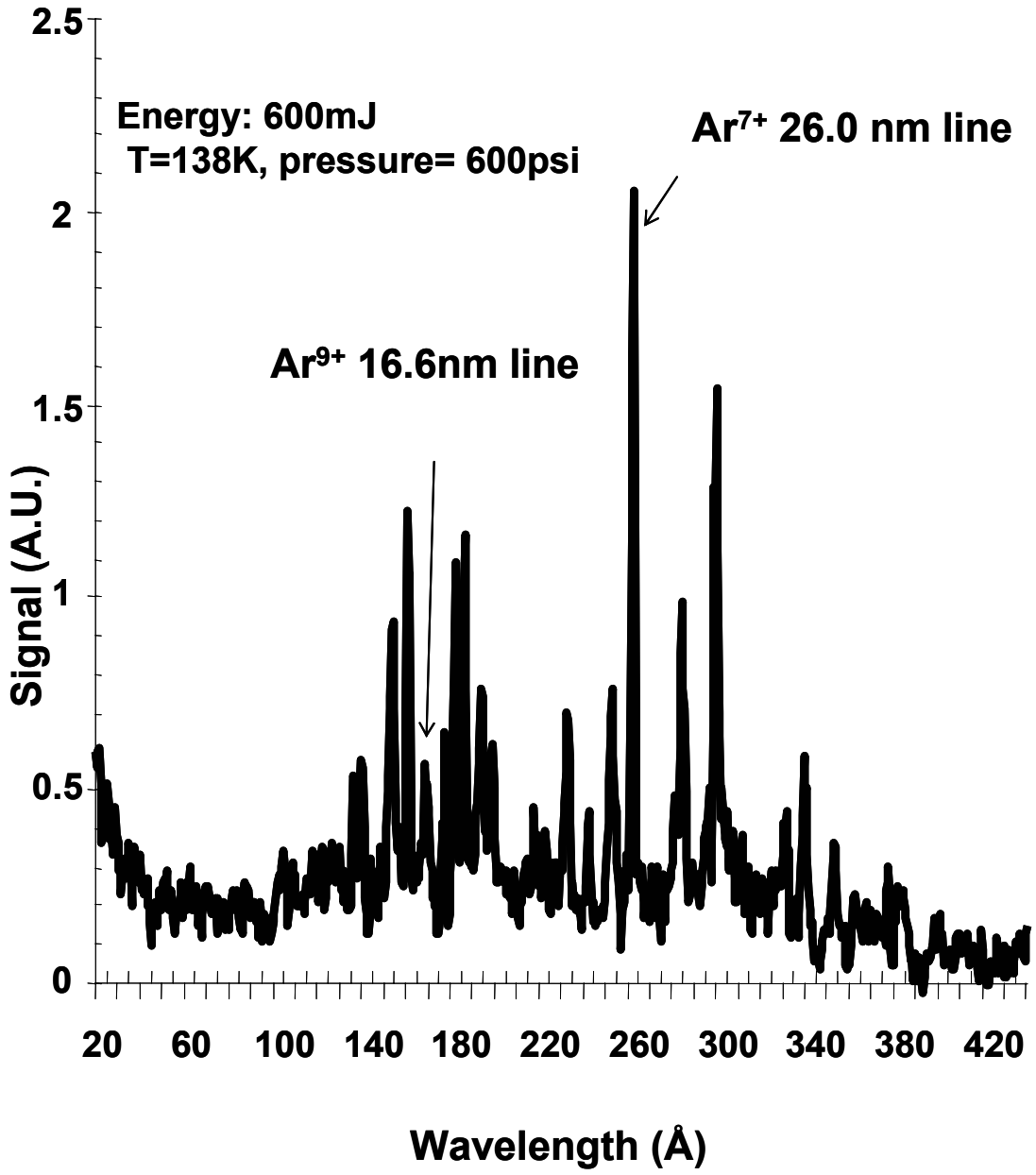

Figure 3.2: Sample spectrum of argon droplets plasma in the range of 2-44nm with space of 0.05nm irradiated by 600mJ 100ps 1064nm Nd:YAG laser pulse under temperature of 138K and backing-pressure of 600psi. Fifty shots were averaged for each data point.

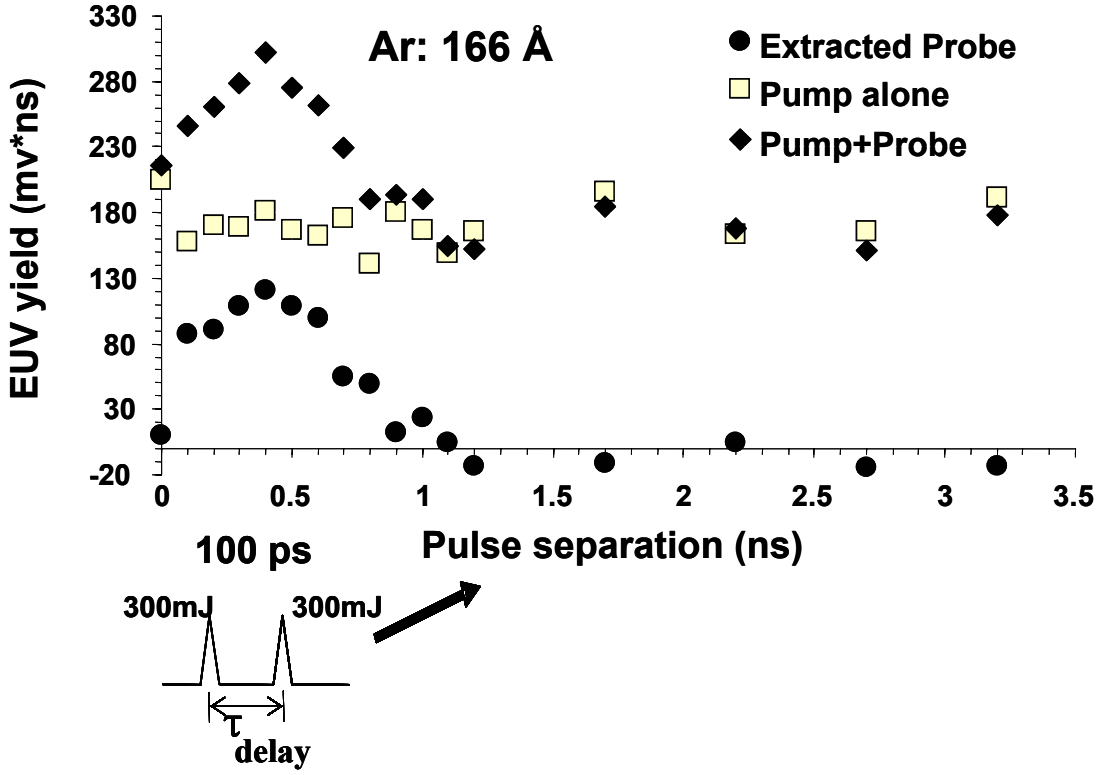

Figure 3.3: EUV yields of argon 16.6nm-line emission irradiated by 300mJ pump + 300mJ probe versus pulse separation under temperature of 138K and backing-pressure of 600psi. Each data point was averaged over five hundred shots.

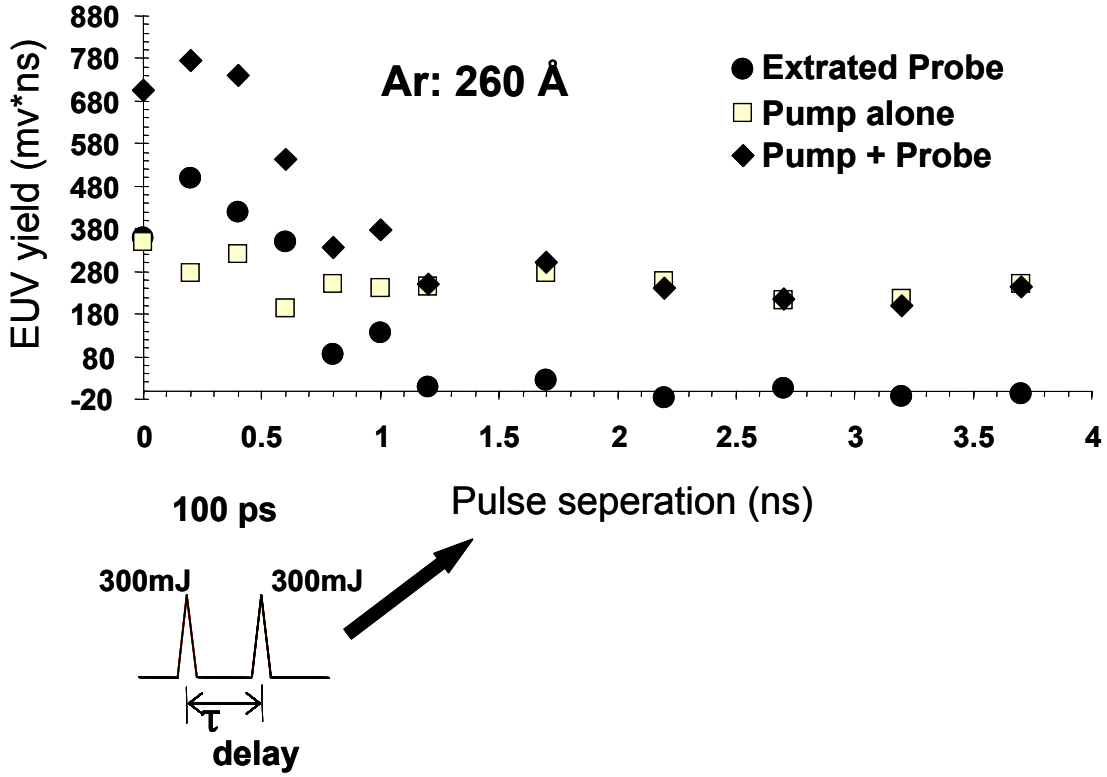

Figure 3.4: EUV yields of argon 26.0nm-line emission irradiated by 300mJ pump + 300mJ probe versus pulse separation under temperature of 138K and backing-pressure of 600psi. Each data point was averaged over five hundred shots.

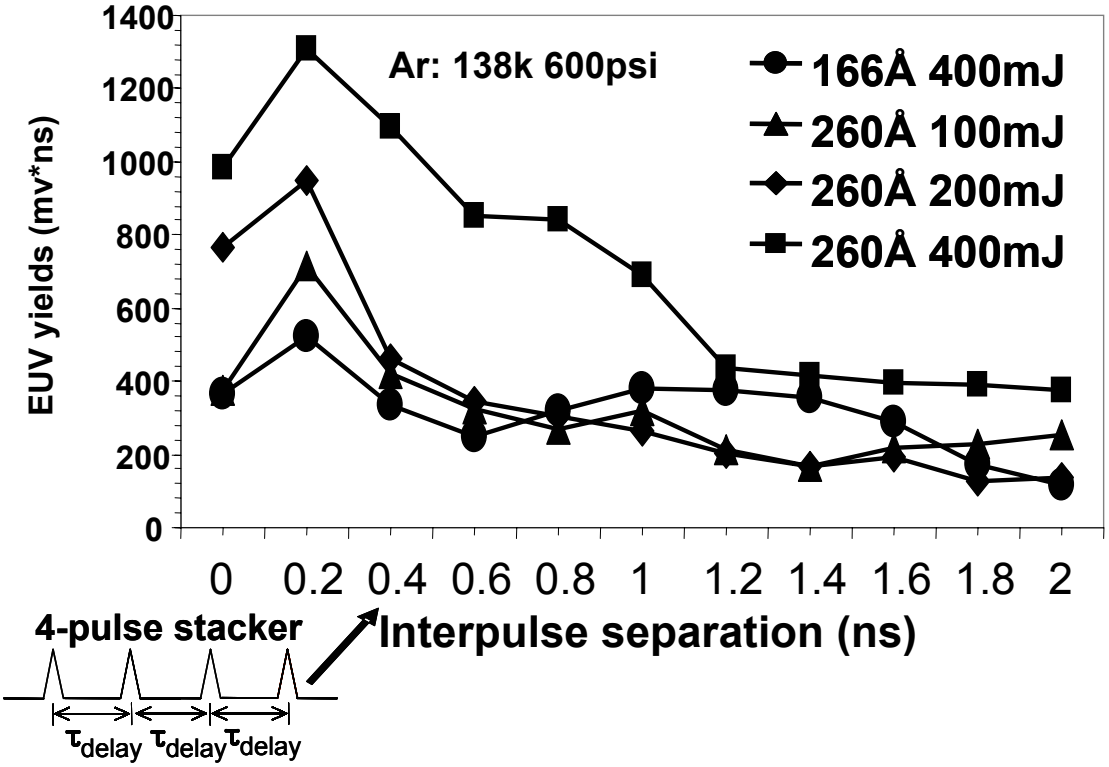

Figure 3.5: Comparison of EUV yields of 16.6nm-line emission and 26.0nm-line emission for argon droplets irradiated by various total laser energies versus inter-pulse separation under the temperature of 138K and backing-pressure of 600psi from the following three pulses (subtracted the amount contributed from the first pulse) with 4-pulse-stacker scheme. Each data point was averaged over three thousand shots.

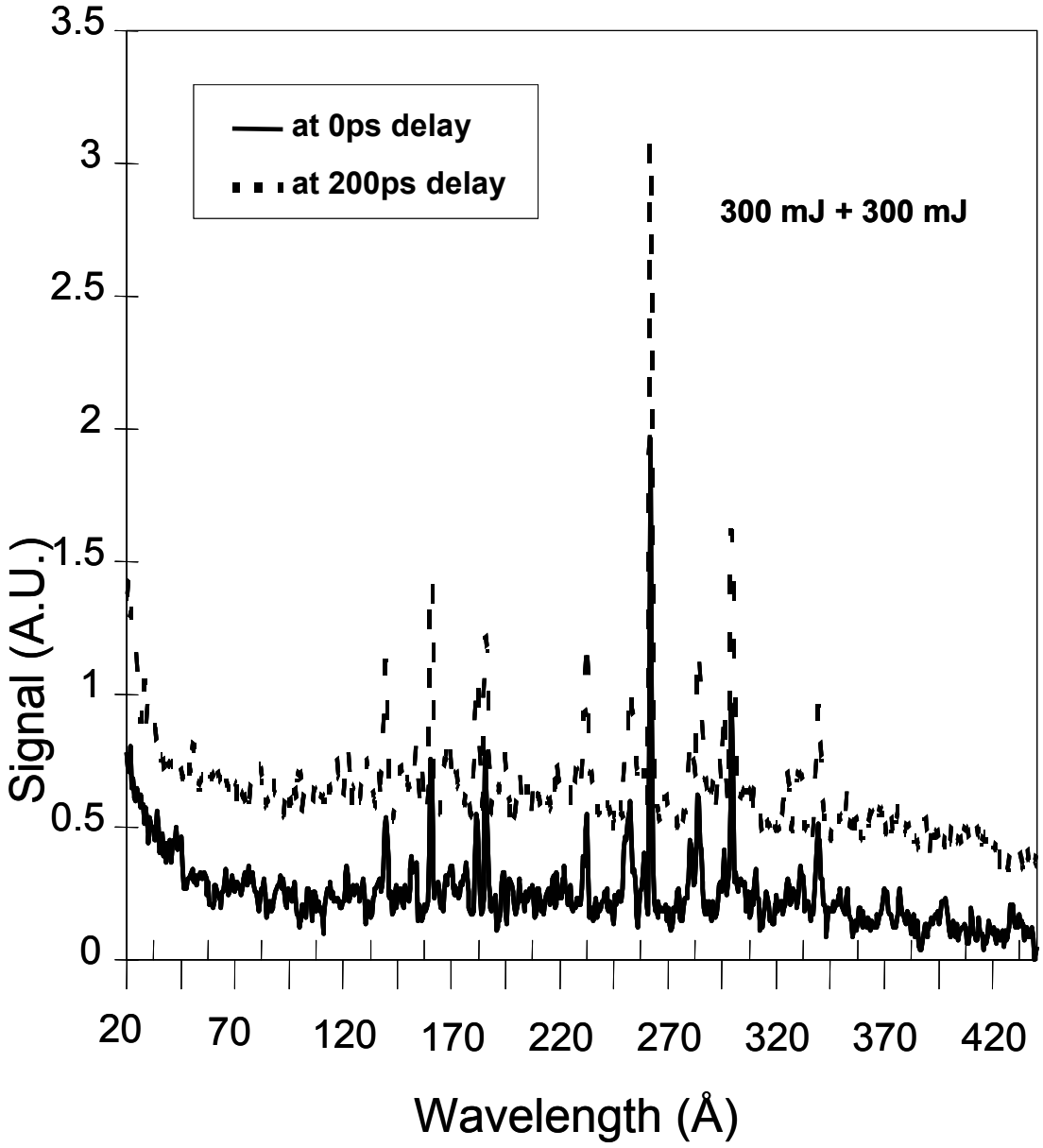

Figure 3.6: Comparison of total spectra yields from argon droplets in the range of 2-44nm under pump probe scheme for two different time delay between pump and probe irradiated by 300mJ pump and 300mJ probe 100ps 1064nm Nd:YAG laser under temperature of 138K and backing-pressure of 600psi.

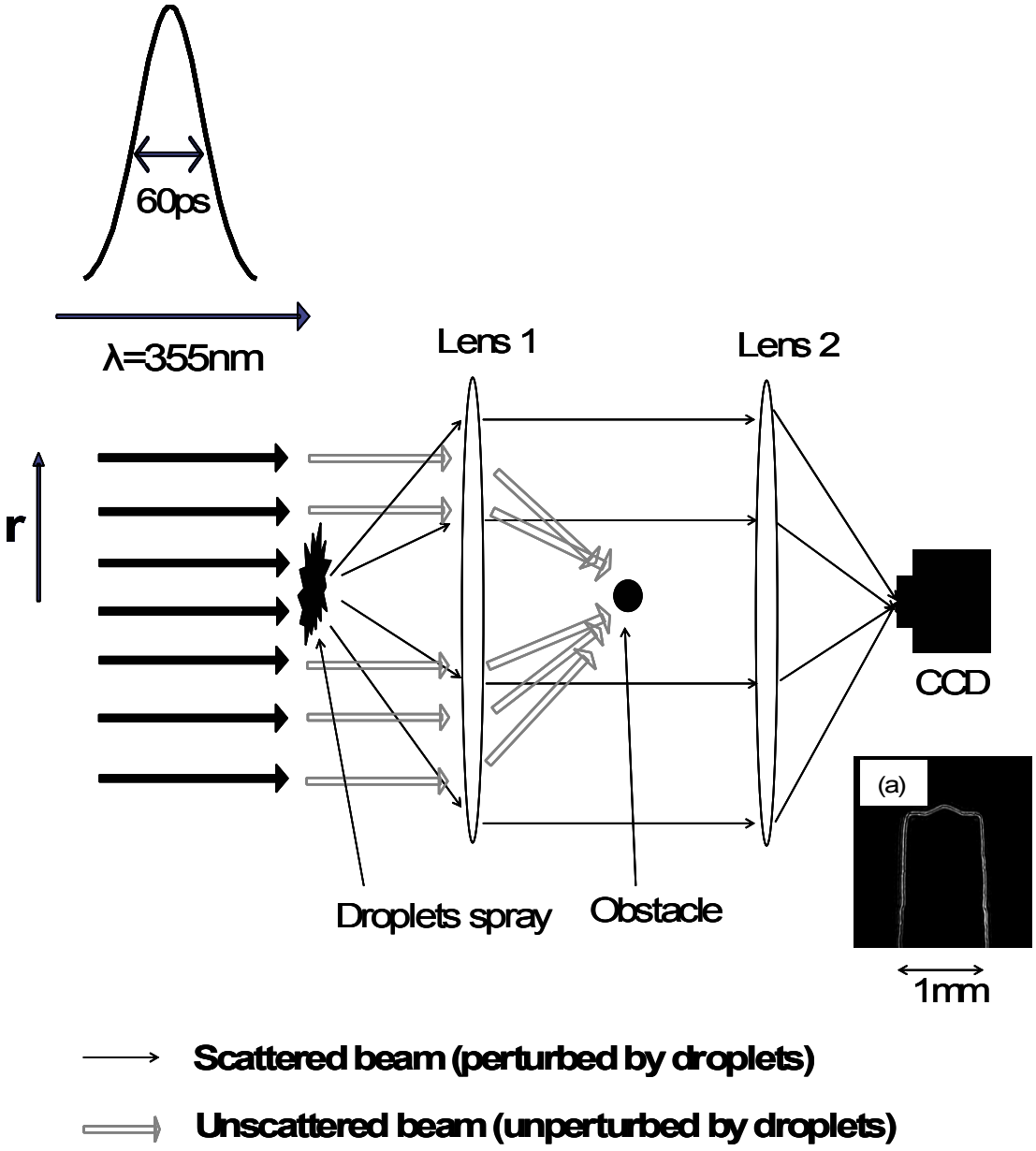

Figure 3.7: Schematic of dark-field shadowgraphy of droplet sources irradiated by 60ps 355nm laser pulses. Inset (a) shows a sample of shadowgraphy image of the tip of a pin used for jet center alignment with laser pulse.

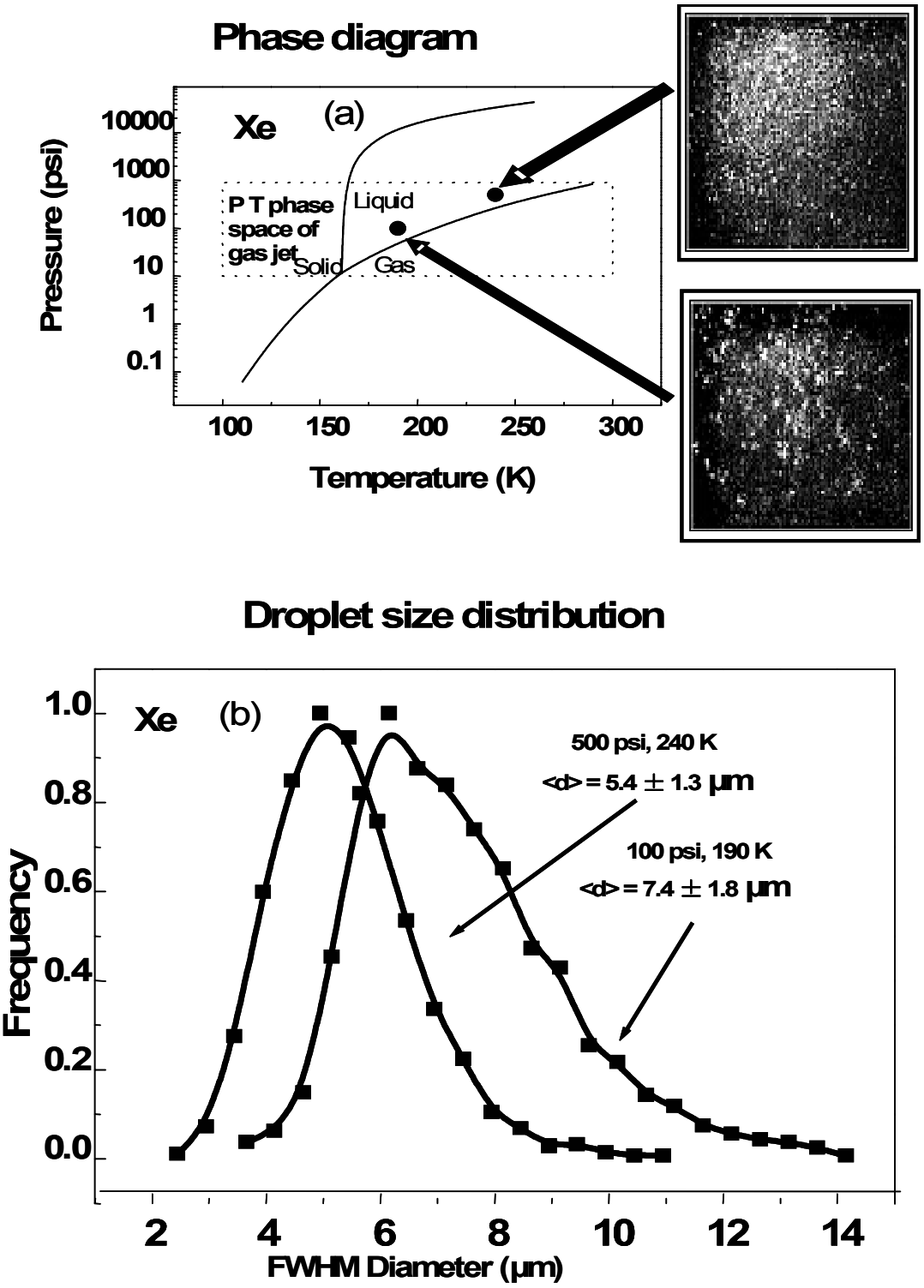

Figure 3.8: (a): Phase diagram of xenon, two dots correspond to experiment running conditions: 500psi/240K and 100psi/190K, respectively. Insets are the side images of the droplets assemble from our droplets jet under these two running conditions. (b): The droplet-size distribution under these two experiment running conditions.

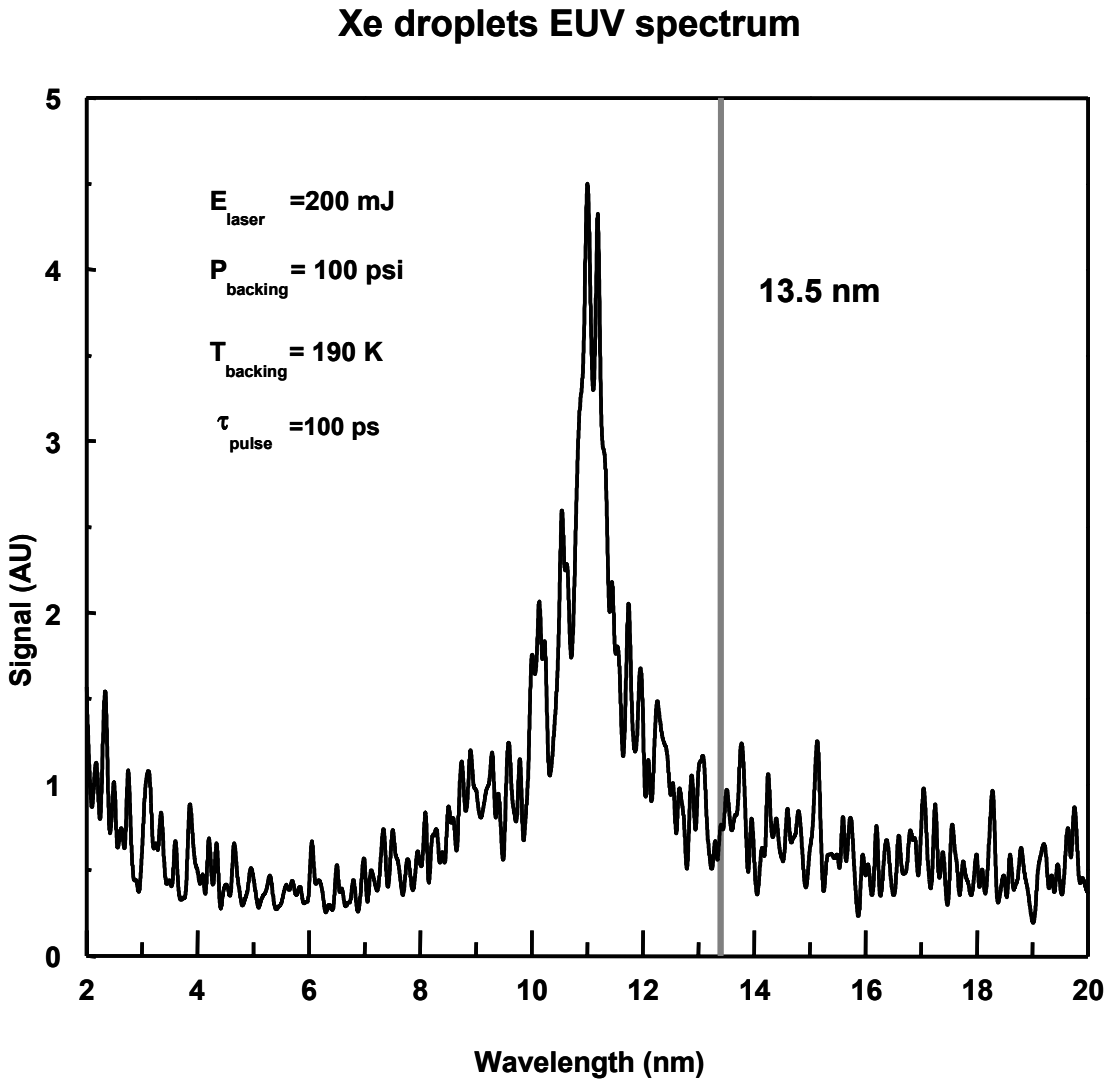

Figure 3.9: A single pump-pulse induced EUV spectrum near 13.5nm with space of 0.05nm from xenon-droplet plasma irradiated by 200mJ, 10Hz, 100ps, 1064nm Nd:YAG laser pulse under backing-pressure of 100psi and temperature of 190K.

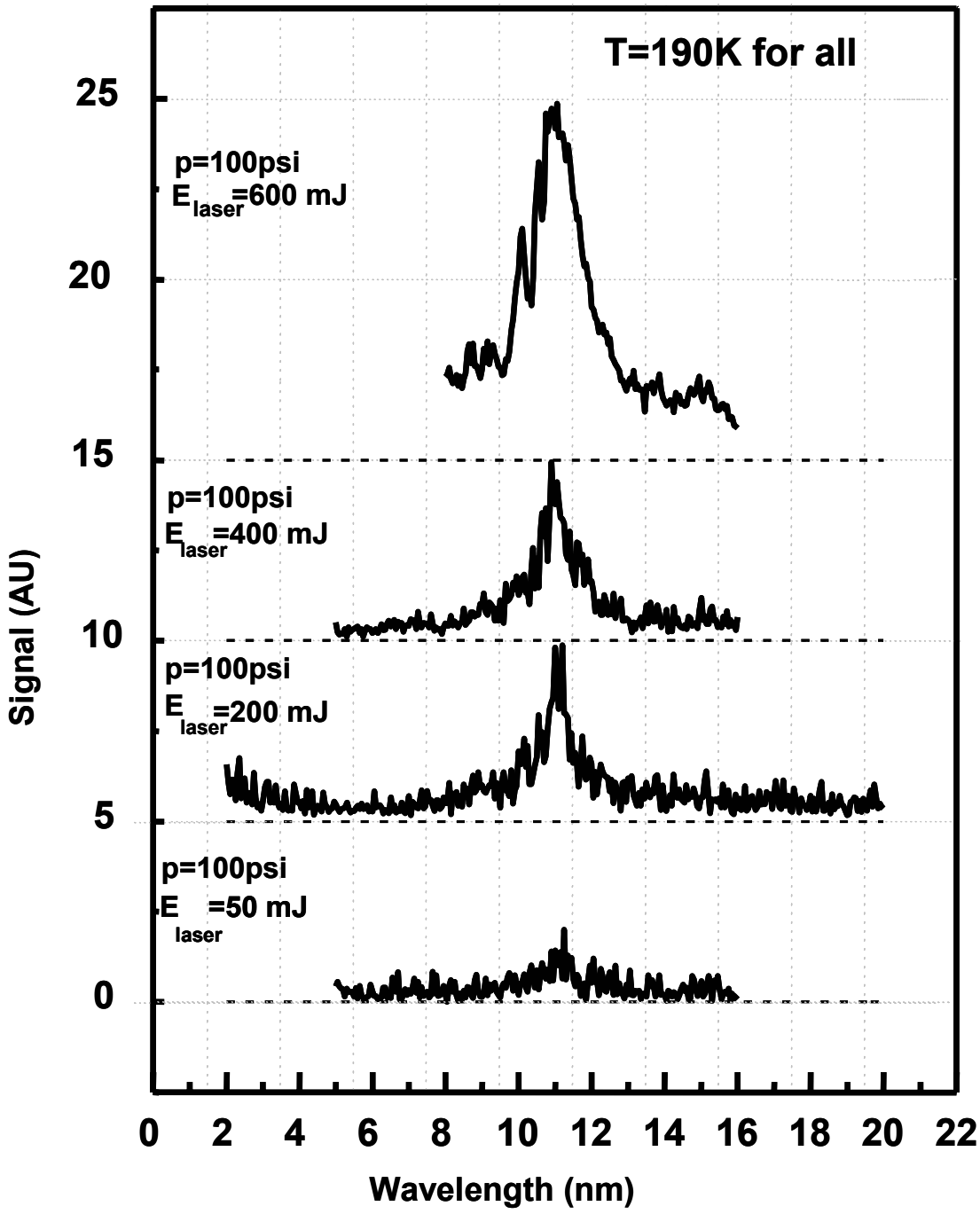

Figure 3.10: Xenon-droplet spectrum versus laser-pulse energy under backing-pressure of 100psi and temperature of 190K.

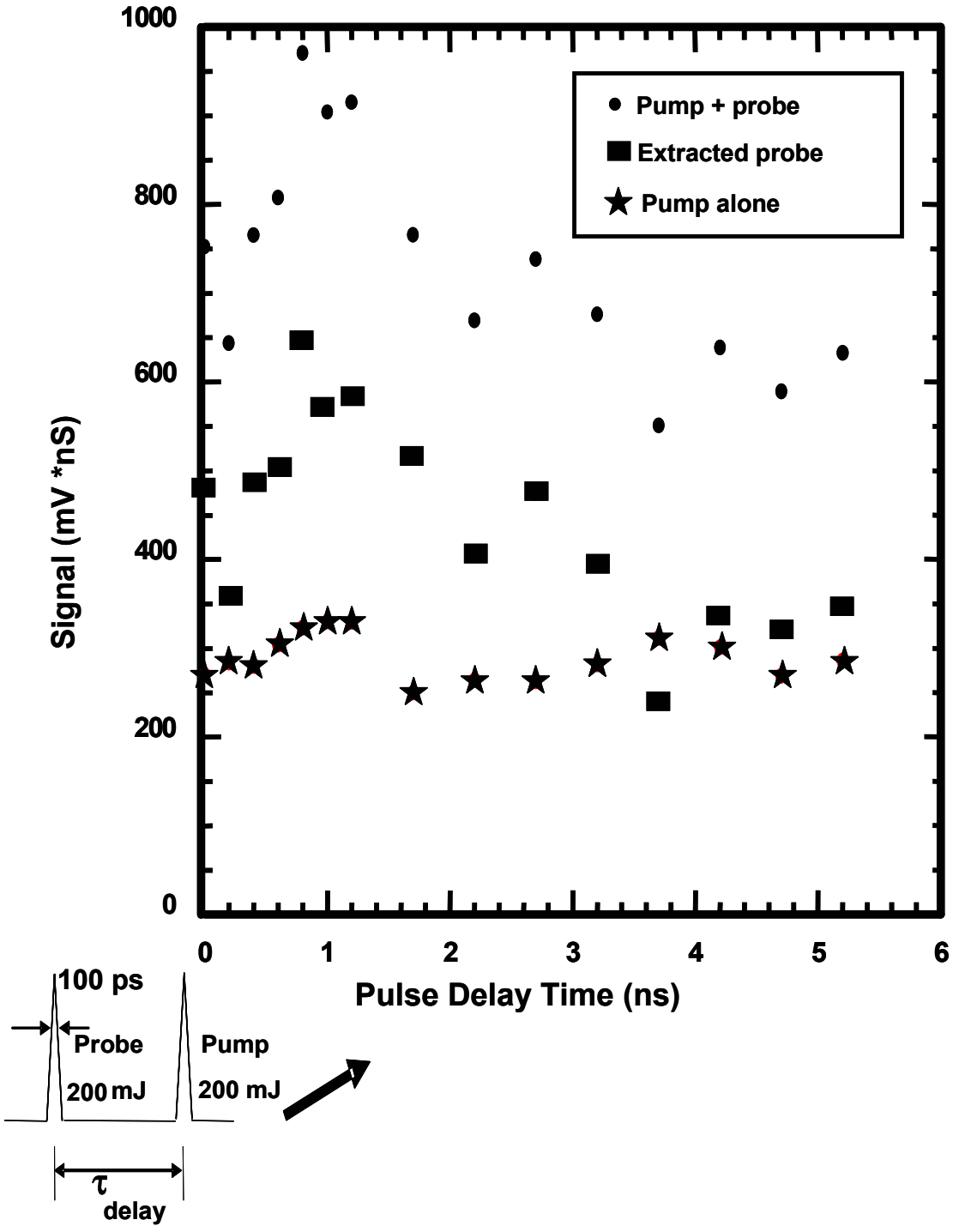

Figure 3.11: EUV yields at 13.5nm from xenon droplets under temperature of 190K and backing-pressure of 100psi versus time delay between pump and probe with laser-pulse energy of 200mJ each from pump probe scheme.

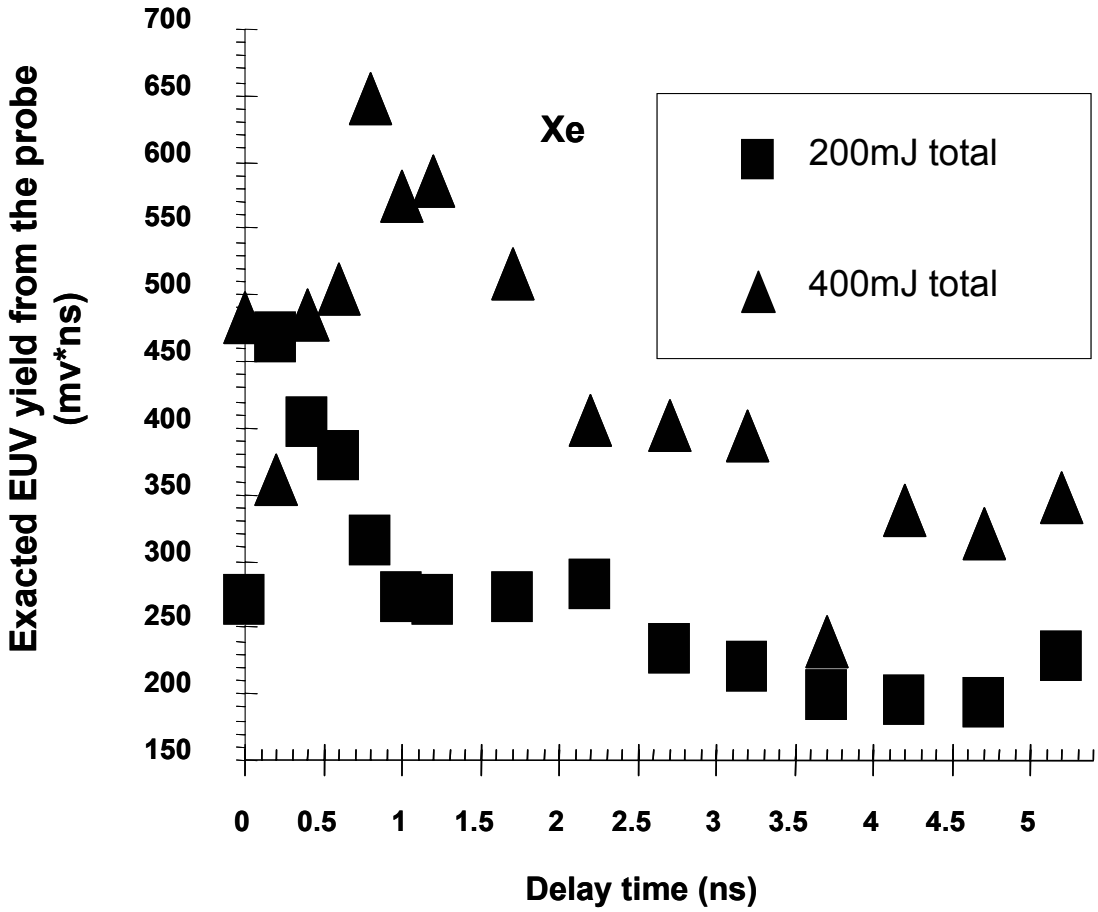

Figure 3.12: Comparison of extracted EUV yields of 13.5nm from various probe laser energy for xenon droplets under temperature of 190K and backing pressure of 100psi with pump probe scheme versus time delay between pump and probe.

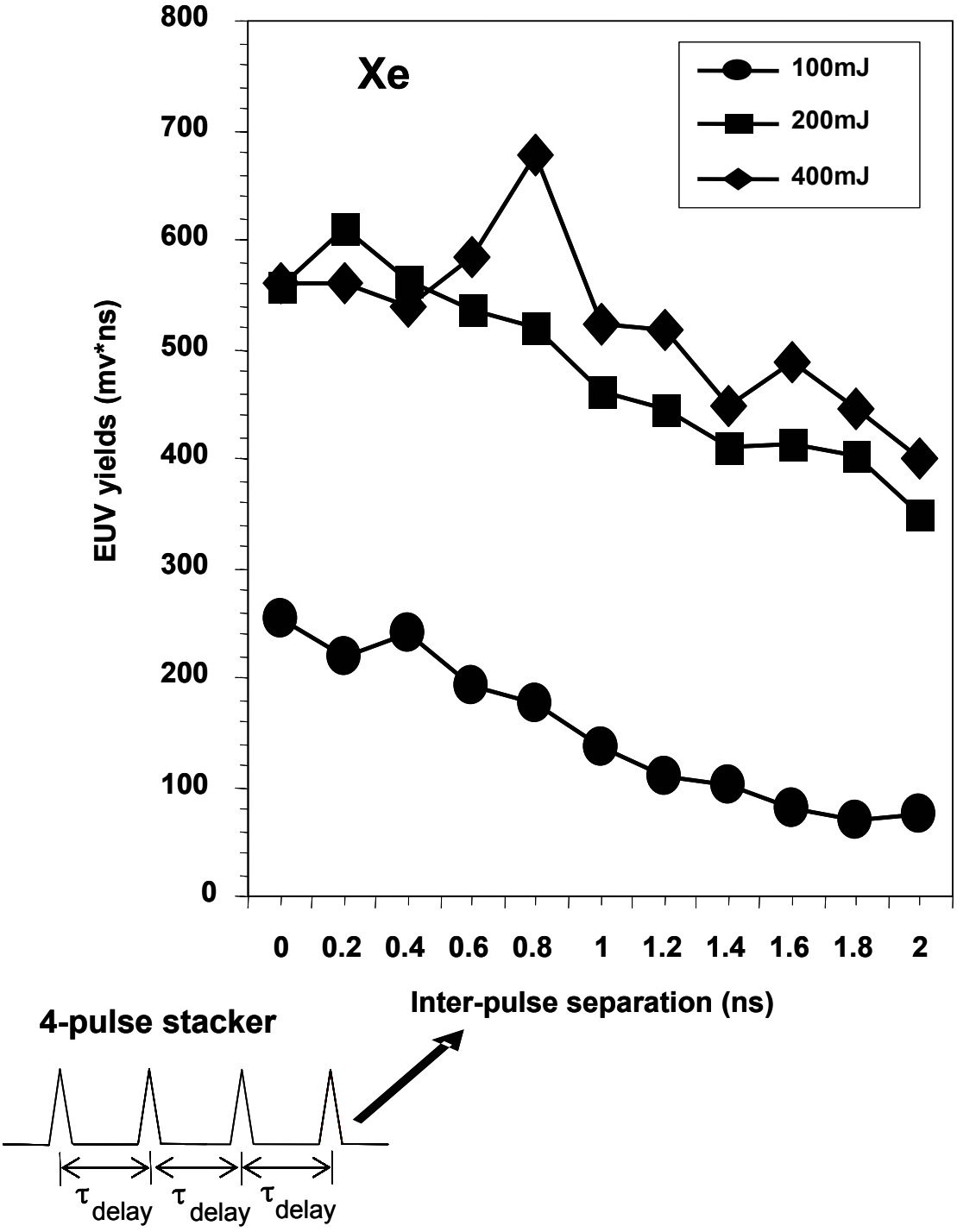

Figure 3.13: Comparison of EUV yields of 13.5nm from xenon droplets generated by the following three pulses (subtracted the amount produced by the first pulse contribution) by varying total laser energy versus inter-pulse separation with 4-pulse-stacker scheme under temperature of 190K and backing-pressure of 100psi.

Chapter 4: Resonant pulse-shortening of high intensity Bessel beams in self-generated under-dense plasmas

4.1 Introduction

The guiding of intense laser pulses over a distance much longer than the Rayleigh length $z_0 = \pi w_0^2/\lambda$ has many applications, such as laser-driven electron accelerators [1-2], guided nonlinear optics [3], nonlinear short wavelength generation [4], generation of high harmonics [5], and soft x-ray amplification [6]. Plasma waveguides formed through hydrodynamic shock expansion is one way to achieve intense pulse guiding over distances >> z_0 [7-13]. The evolution of electron-density forming the waveguide channel plays the key role for the above applications. It is strongly dependent on many parameters, such as neutral gas density of the initial gas target, gas species, channel breakdown energy, and laser parameters [14].

In the case of Bessel-beam generation of plasma waveguides, a new type of resonance absorption was explored by our group [15-16]. Those experiments found that the Bessel beam produced by axicon-focusing of an incident 100ps, 1064nm pump pulse, could experience enhanced absorption for certain ranges of gas pressure. The enhanced absorption corresponded to the condition where the Bessel beam side coupled some of its energy into a guided mode of the plasma waveguide [15-16]. Figure 4.1 shows absorption of the pulse as a function of pressure [16]. Two strong resonant-absorption peaks versus pressure occur. It was found that enhanced

absorption occurs only for specific backing pressures [15-16]. The resonant absorption results from the resonant self-trapping of Bessel beams [15-16]. The self-trapping of the Bessel beam versus the gas fill pressure is plotted in Fig. 4.2 [16]. The pressure dependence of the self-coupling corresponds well to that of the absorption resonance in Fig. 4.1, with a clear peak at ~300torr for the $p = 0, m = 0$ resonance and less well-defined peak at ~460torr for $p = 1, m = 0$ resonance, where p and m are radial and azimuthal mode indices [16]. The findings strongly suggest that a temporal slice of the pulse is trapped and guided through the generated waveguide, only under the resonant backing-pressures.

In this experiment we injected the scattered-out portion of laser pulses (transmitted beams/conical beam) into a streak camera with a time resolution of 5ps, which allows us to experimentally explore and characterize the temporal structure of the conical beam. We demonstrated that resonant pulse-shortening occurs, consistent with the earlier experiments [16]. Two dips were observed at ~340torr and 460torr, respectively. A 1-D simulation result of Bessel-beam-plasma interaction is also given for comparison. The details are discussed in Section 4.2-4.3.

4.2 Background

In the presence of plasma, a generalized Bessel beam solution for the electric field of a propagating laser pulse, in a medium invariant along the optical axis z, can be found, which has $\widetilde{E} = e^{i\beta z} u(\vec{r}_\perp, \omega)$, where ω is the laser angular frequency, β is

the propagation wave-number along z axis, $\vec{r}_\perp$ is the transverse coordinate, and $u(\vec{r}_\perp, \omega)$ satisfies the Fourier transformed wave equation

$$\nabla_\perp^2 u + \kappa^2(\vec{r}_\perp, \omega)u = 0 \qquad (1)$$

where $\nabla_\perp^2$ is the Laplacian in the transverse coordinate $\vec{r}_\perp$, $\kappa^2 = k^2 n^2 - \beta^2$, κ is the transverse wave-number, $k = \omega / c$ is the vacuum wave-number, n is the refractive index of plasma given by $n^2(\vec{r}_\perp, \omega) = 1 + 4\pi\chi(\vec{r}_\perp, \omega) + \delta_{plasma}(\vec{r}_\perp, \omega)$, χ is the sum of atomic and ionic susceptibilities, and δ_{plasma} is the contribution from plasma. We used a Drude model to describe the plasma dielectric response which gives $\delta_{plasma}(r, \omega) = -\xi + i\xi\nu / \omega, \xi = (1 + \nu^2 / \omega^2)^{-1} N_e(r) / N_{cr}$, where r is transverse radius, $N_e(r)$ is the transverse electron-density, and $N_{cr} = m_e\omega^2 / 4\pi e^2$ is the critical density. $\nu = \nu(r)$ is the collision frequency that takes account of electron-ion and electron-neutral collisions. Under our typical experimental conditions (300torr argon gas heated by 100ps, 350mJ 1064nm laser pulse), $\nu \approx 10^{12} - 10^{13} s^{-1}, \omega \approx 10^{15} s^{-1}$.

For a stationary profile, well outside the plasma boundary ($r >> r_b$ and $\kappa_0 r >> 1$), the asymptotic solution of Eq. (1) gives

$$E(\vec{r}_\perp, z, \omega) \approx E_i e^{i\beta z}[e^{-i\kappa_0 r} + \eta e^{-i(m+1/2)\pi} e^{i\kappa_0 r}] \times e^{im\phi} / (2\pi\kappa_0 r)^{1/2} \qquad (2),$$

where E_i is the peak electric field, m is an azimuthal index, $\kappa_0 = \kappa(r > r_b) = (k^2 - \beta^2 + 4\pi\omega^2\chi_0 / c^2)^{1/2}$, $\chi_0 = \chi(r > r_b)$, and η is the complex scattering coefficient of the outgoing wave, which depends on the specific plasma structure. In the stationary limit the fractional plasma absorption of the Bessel beam is given by $1 - |\eta|^2$.

For a given plasma channel $N_e(\vec{r}_\perp)$, the solutions to Eq. (1) can be categorized into several modes, depending on the behavior of $\kappa^2(\vec{r}_\perp, \omega)$. When $\kappa^2 < 0$ for all $r > r_m$ and $\kappa^2 > 0$ for all $r < r_m$, where r_m is a radial location in the plasma, solutions of Eq. (1) give the *bound modes*, which is the ideal case. However, in reality, beyond the plasma boundary, $\kappa^2 > 0$ occur again. Thus, strictly, *bound modes* do not occur. *Excluded modes* exist when $\kappa^2 < 0$ for $r < r_m$ and $\kappa^2 > 0$ for $r > r_m$. If $\kappa^2 > 0$ for all r, it gives the solutions of *radiation modes*. For some particular cases, the region of interest here, if $\kappa^2 > 0$ for $r < r_1$, $\kappa^2 < 0$ for $r_1 < r < r_2$, and $\kappa^2 > 0$ again for $r > r_2$, where $r_1 < r_2$, some confinement of the wave within the interior channel region occurs, but leaking to freely propagating waves at $r > r_2$ is allowed, such modes are called "*leaky"*. During the plasma evolution, *excluded modes*, *radiation modes*, and *leaky modes* are possible modes. In the early stage of the avalanche-driven electron-density growth, electron density has peak on the axis and keeps growing; only the *radiation modes* or *excluded modes* are present. When the shock wave develops and a plasma channel forms, the *leaky modes* are possible. For idealized *bound modes*, only discrete values of β are allowed because no field exists outside the channel. For the *leaky mode* solutions to Eq. (1), where the solutions extend beyond the plasma boundary, narrow continuous ranges of β, labeled as β_{ch}, are allowable [15-16]. Generally, for a given radial plasma-profile, β_{ch} must be calculated numerically [20]. In our experiment, the Bessel beams have been produced using an axicon lens on which a Gaussian laser-beam is normally incident. The beam is bent toward the axicon axis with the angle γ with respect to the axis of the axicon, as shown in Fig.

4.3. The rays interfere with each other on the axis, such that the transverse profile of the beam is invariant along the axis for a finite range. A Bessel-function-shaped-field profile with the axial wave number $\beta = k\cos\gamma$ is formed. After the line focus, the beam diverges as a cone of rays (conical beam) also shown in Fig. 4.3. When the leaky modes β_{ch} of an evolving plasma waveguide matches the axial wave-number $\beta = k\cos\gamma$, the laser field can tunnel into the waveguide and excite the quasi-guided modes, and resonant self-trapping occurs.

The modeling of the Bessel-beam plasma interaction is a quasi-stationary calculation, in which the time-independent Eq. (1) is coupled to a model of the time-dependent plasma hydrodynamics. The reason for that is the much shorter transit time (<1ps) for light across the plasma channel (maximum diameter ~100μm) compared with the plasma-hydrodynamics time-scales (~50ps for avalanche-driven electron density growth, ~100ps for shock development, and ~1ns for radial evolution of the plasma column) and the laser pulse duration (100ps) [17]. Because the plasma is cylindrically symmetric [18], the model is further simplified by using a 1-D radial Lagrangian hydrocode. The calculation includes field ionization [19], collisional ionization, gradient-based and flux-limited thermal conduction, and a collisional-radiative ionization package.

In this experiment we fixed the laser energy, the laser wavelength, and the laser pulse-width and used the same axicon Bessel-beam parameters, while varying the gas density. Resonant pulse-shortening versus the initial gas density is demonstrated.

4.3 Experimental setup

Figure 4.4 shows the experimental setup. The laser system used in this experiment was 10Hz Nd:YAG laser pulse with a wavelength of 1064nm, pulse duration of ~100ps, and energy of 350mJ. Laser beams are normally incident on the axicon with respect to its plane surface. The axicon used has a base angle of $\alpha = 25°$, corresponding to a ray-approach angle of $\gamma = 15°$ with respect to the optical axis. The resulting J_0 beam produces a ~1.5cm-long plasma column in the ambient mixed gases consisting of 20-torr N_2O and variable pressure of argon. The beam transverse-profile is invariant along the line focus, the longitudinal intensity-distribution along the axicon's line-focus peaks at about the axial mid-range of the axicon focus and decreases toward the two ends. The envelope is shown in Fig. 4.4. The peak intensity of the laser pulse is approximately 5 x 10^{13}W/cm^2. To remove electrons from neutral atoms through optical-field ionization, the ionization potential required for argon gas is U_I =15.8eV, The Keldysh parameter [21] $\gamma = (U_I / 2U_p)^{1/2}$ is used to describe the ratio of the ionization time to the laser period, where U_I is the ionization potential of the atom or ion and U_p is the ponderomotive potential which is given by $U_p = e^2E^2/4m_e\omega^2$. For our case, U_p = 5eV corresponding to $\lambda = 1064nm$ gives $\gamma \approx 1$. The ADK tunneling theory [22] has been shown experimentally [23] to well predict the ionization rate for $\gamma \approx 1$. The laser initially produces seed free-electrons via tunnel ionization, which depends on the laser's peak intensity. The liberated electrons are further heated by absorbing energy from the laser field through inverse *bremsstrahlung* [24-26]. The plasma waveguide formed is longitudinally uniform (except at the ends, where the plasma tapers [17] over a distance of ~ a few hundred

μ m [17]) and cylindrically symmetrical about the optical axis [17-18]. To more easily generate the uniform avalanche breakdown in argon gas, seed electrons were provided by the N_2O component, which can be field ionized at ~10^{13}W/cm^2 lower than that of argon [17]. In the event of self-trapping, the pump laser-pulse is quasi-confined in the plasma channel. A portion of the incident laser beam is trapped and guided along the plasma axis during self-trapping (denoted as trapped beam here), and the remaining part of the incident laser beam (the un-trapped axicon rays) transmits through the plasma and forms a ring (conical beam), which diverges quickly (denoted as transmitted beam here). To separate the trapped pulses (trapped beam) from the measurement of the ring beam (transmitted beam), a 45-degree reflective mirror with a hole in the center, coated at 1064nm wavelength, was used. The trapped beam passed through the hole and was captured by a CCD camera that monitored the mode profile at the exit-plane of the plasma-waveguide channel. The transmitted beam was then reflected by a mirror and redirected to a streak camera, which explicitly gave the temporal profile of the un-trapped ring. The pulse-shortening of the Bessel beam by its self-generated plasma was measured by the streak camera. Since the camera is not sensitive to infrared light, a KDP crystal was used to double the frequency of the laser pulses to the wavelength of 532nm, appropriate to the streak camera photocathode. The streak camera was calibrated with equal-paced pulses in the time domain generated by using a variable optical-delay line. The resulting resolution is 3.2ps per pixel along the axis.

4.4 Experimental results and discussion

The signals averaged over 50 shots (laser on) were extracted by subtracting the 50-shot averaged background (laser off). Figure 4.5(a) shows one sample of the extracted results. To minimize the noise, the extracted signal pulses were then fitted to a polynomial curve. A sample of the fitting results is shown in Fig. 4.5(b). From there, the full width at half maximum (FWHM) of signals was calculated. The pulse-width of the transmitted beam versus the initial gas pressure is plotted in Fig. 4.6.

At low pressure, the pulse width is almost 100ps which is the same as that of our incident laser pulse. It implies that the plasma is transparent to the pulse. The typical pulse shape under pressure of 220torr is shown on the inset (1). That is because when the initial gas pressure is too low, $N_e < N_{cr} \sin^2 \gamma$ all the time, only *radiation modes* are allowed, almost all the incident pulse transmit through the plasma without trapping, except that only the front edge (<=50ps) of the incident pulse is absorbed to heat the gas and form the plasma. As the pressure increases, the pulse-width of the transmitted beam decreases very quickly, and the first dip appears around 340torr. At slightly higher pressures the pulse-width increases back sharply, implying a resonant pulse-shortening at ~340torr. This implies that a temporal slice of the incident-pulse envelope is trapped by the evolving plasma channel, which appears as the pulse-width of the transmitted beam is shortened. Inset (2) shows the typical pulse shape under the resonant pressure of 340torr. This is because, as the pressure increases, $N_e > N_{cr} \sin^2 \gamma$ could occur during the plasma evolution, and self-trapping of the beam is allowed. When the incident Bessel beam has the axial wave number $\beta = k \cos \gamma$ match to β_{ch} for the evolving channel, strong resonant coupling of the

beam can occur. A significant portion of the middle temporal slice of the incident pulse is trapped in the plasma, rather than being transmitted through it. When the pressure is increased a little bit higher than 400torr, the pulse resonantly shortens again, with the second dip occurring at ~460torr. Inset (3) shows the typical pulse shape under that pressure. It is seen that the corresponding pulse width is 68ps. Beyond that pressure, the pulse-width did not change significantly because, when the pressure is high enough, many higher-order modes are able to be self-trapped in the more rapidly evolving and larger-diameter waveguides. Portions of the middle temporal slice and even the tail part of the incident pulse are trapped in the plasma at those high pressures. Inset (4) is a sample of the pulse trace at 660torr.

Comparing those results with the self-coupling efficiency of the incident pulse measured in our previous experiments with the same 25^0 base angle axicon corresponding to $\gamma = 15^0$ [15-16], the first dip occurs at ~300torr in that experiment, reasonably close to the result of pulse shortening. The second dip occurs at ~460torr in that experiment, which agrees with this experiment. At low pressure, the self-coupling efficiency is almost zero. When the pressure increases, the first strong resonant coupling occurs at a pressure of 300torr, corresponding to the $p = 0, m = 0$ lowest order mode. Inset (1) shows the mode profile at that pressure. At slightly higher pressures, the coupling drops significantly, obviously indicating a resonant trapping at ~300torr. As pressure increases to higher than 400torr, the coupling efficiency increases again. The second strong coupling occurs at 460torr. Inset (2) shows that the dominant mode is the $p = 1, m = 0$ mode. That is quite consistent with the results of the pulse-width measurements of the transmitted beams. As pressure

increases further, many higher-order modes are allowed [16]; the coupling efficiency keeps increasing. In our pulse-width measurements of the transmitted beams, it is almost constant after 560torr. Figure 4.7 shows a simulation for total absorption

$$A = \frac{\int_{-\infty}^{\infty} (1 - |\eta(t)|^2) E_i^2(t) dt}{\int_{-\infty}^{\infty} E_i^2(t) dt} \tag{3}$$

as a function of pressure for the conditions of Fig. 4.1: peak vacuum intensity of 5×10^{13}W/cm^2, λ=1064nm, 100ps pulse-width laser incident on axicon with ray-approach angle of $\gamma = 15^0$ in an ambient gas of 20-torr N_2O plus a variable pressure of argon. The result shows two main resonant peaks ($p = 0, m = 0$ mode and $p = 1, m = 0$ mode) at 300torr and 460torr, respectively. It is in agreement with the pulse-shortening experiment. Because the model assumes cylindrical symmetry, the coupling to $m > 0$ electromagnetic modes is not addressed, while coupling to $m > 0$ modes is allowed for higher pressures in the experiment. We also observed and measured the pulse-width of the trapped beams, where we removed the CCD camera and injected the trapped beams to the streak camera with frequency doubled using the KDP crystal. When the pressure is below 300torr, the signal is too weak to observe well-defined pulses. Samples of such traces are shown in Fig. 4.8(a). At 340torr, pulses with well-defined pulse-width occur, as shown in Fig. 4.8(b). It is seen that the width of pulses exiting from the plasma channel is ~49.6ps. That indicates that a certain temporal slice of the incident pulse is resonantly trapped and guided by the evolving plasma channel. Inset (1) shows the mode of exiting pulses. When the pressure increases again before reaching 460torr, either no pulses or only pulses with

widths not well-defined were observed, like the case of below 300torr. At 460torr, pulses with clear widths occur again, the averaged width is 54.4ps, as shown in Fig. 4.8(c). Inset (2) shows the mode of exiting pulses. Another resonant pulse-shortening is indicated. At greater than 600torr, at the plasma-channel exit, pulses with well-defined widths emerge out; the average width is 50.2ps. A sample trace is shown in Fig. 4.8(d). The results of pulse-width observations of trapped beams complement those of pulse-width measurements of transmitted beams. They show strong evidence that resonant pulse-shortening occurs.

4.5 Conclusion

We demonstrated resonant pulse-shortening in an under-dense ($N_e \sim 10^{-2} N_{cr}$) plasma channel. The findings are consistent with our earlier experiment results and simulations. Two strong resonant dips in the pulse widths of transmitted beams were observed at 340torr and 460torr.

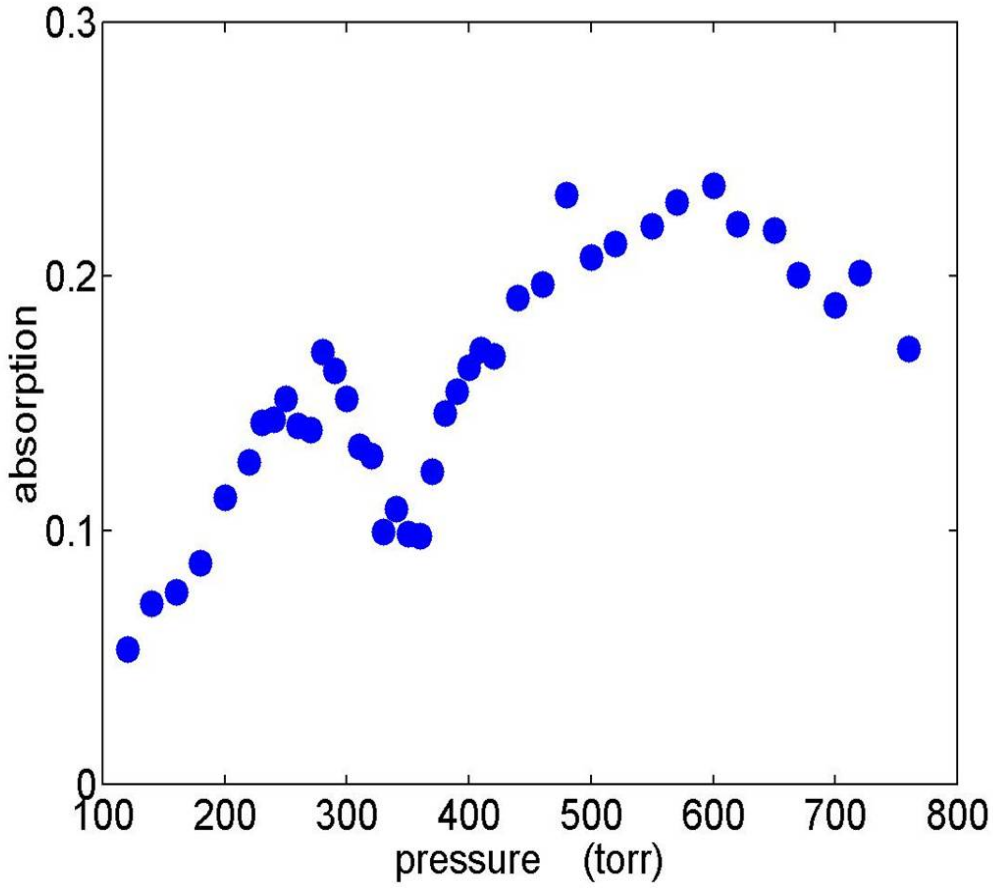

Figure 4.1: Absorption efficiency versus pressure. 10Hz 100ps, 1064nm, 350mJ Nd:YAG laser pulse injected onto the axicon with base angle of 25^0. Gas fill was 20-torr N_2O with variable pressure argon. Each point was averaged over five hundred shots.

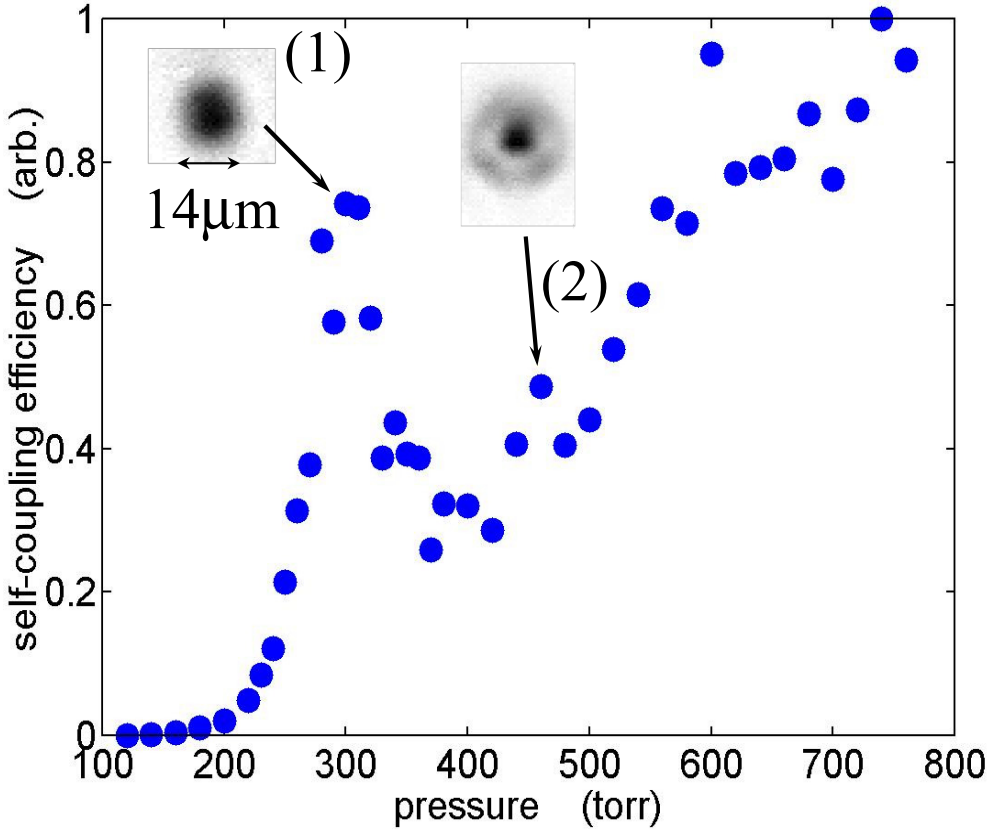

Figure 4.2: Relative self-trapped energy measured at channel exit versus pressure; each point was averaged over ten shots. Insets are resonant mode images at different pressures

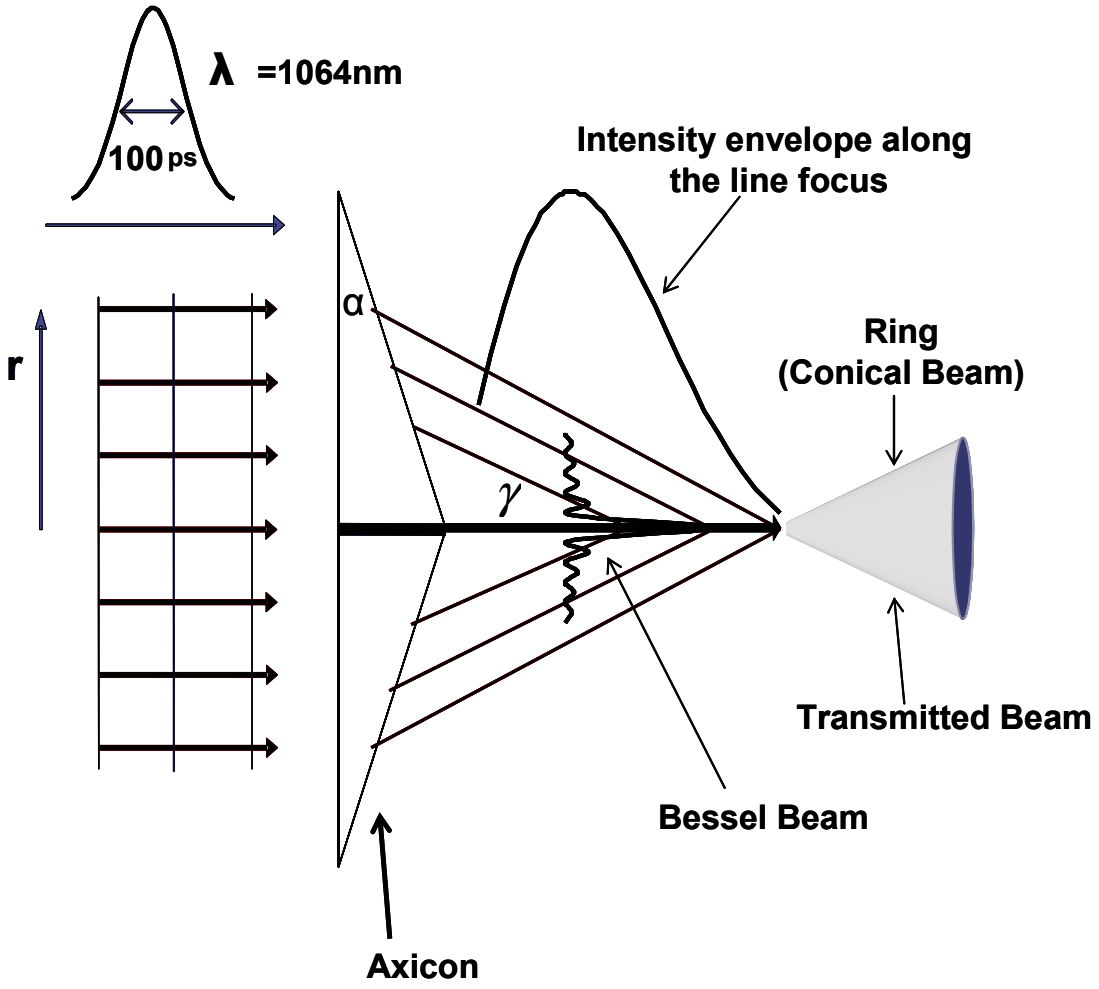

Figure 4.3: The diagram of J_0 Bessel beam generation using axicon with base angle of $\alpha=25^0$. The injected laser pulse was from 10Hz, 100ps, 1064nm, 350mJ Nd:YAG laser pulse, After the line focus, The transmitted beam is a divergent ring (conical beam).

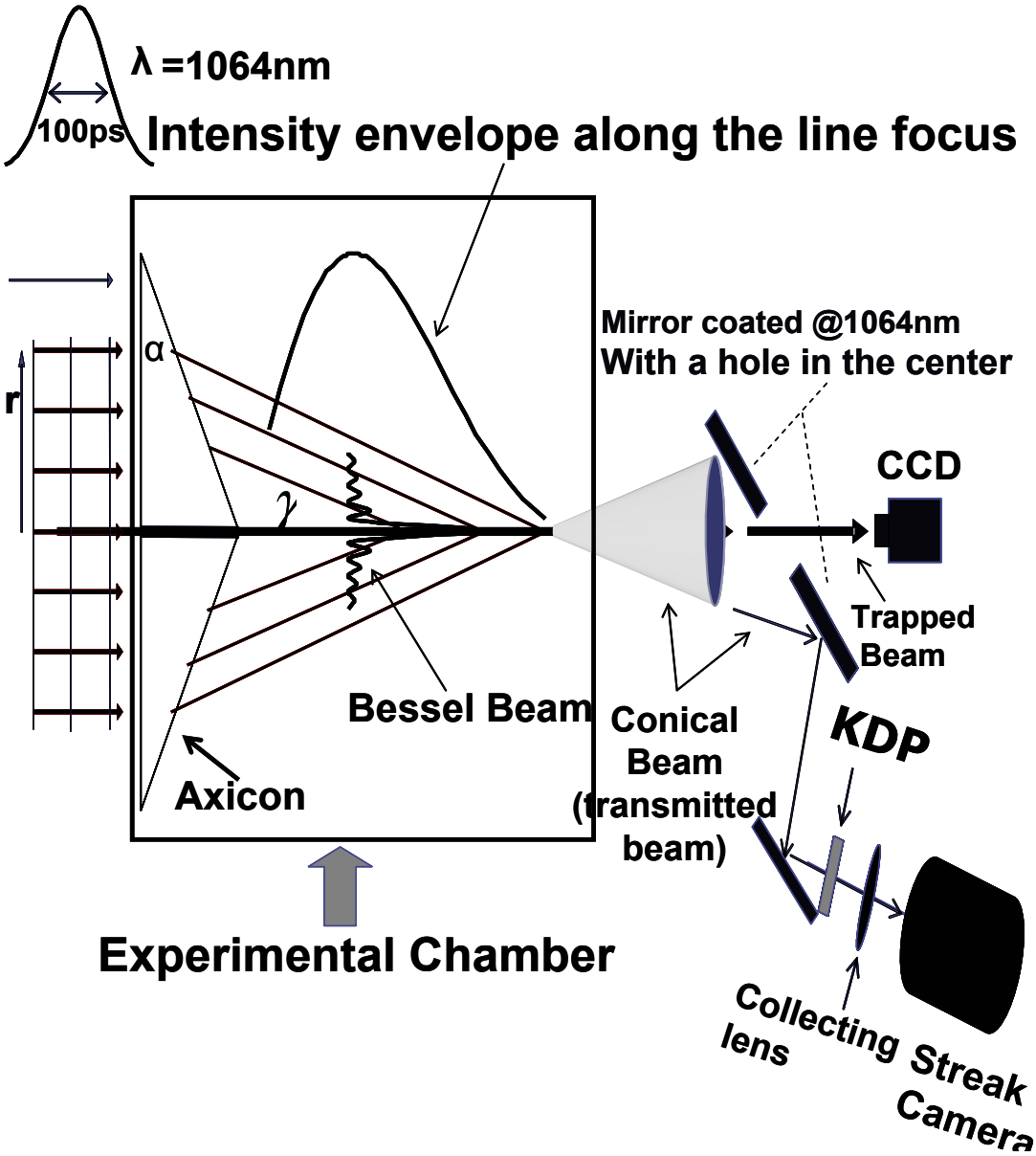

Figure 4.4: Experimental setup to measure Bessel-beam resonant pulse-shortening, laser beam was from a Nd:YAG laser system (10Hz 100ps, 1064nm, 350mJ). Axicon had a base angle of $\alpha=25^0$ corresponding to $\gamma=15^0$. Gas fill was 20-torr N_2O with variable pressure argon. The transmitted cone beam was directed into a streak camera after frequency doubling.

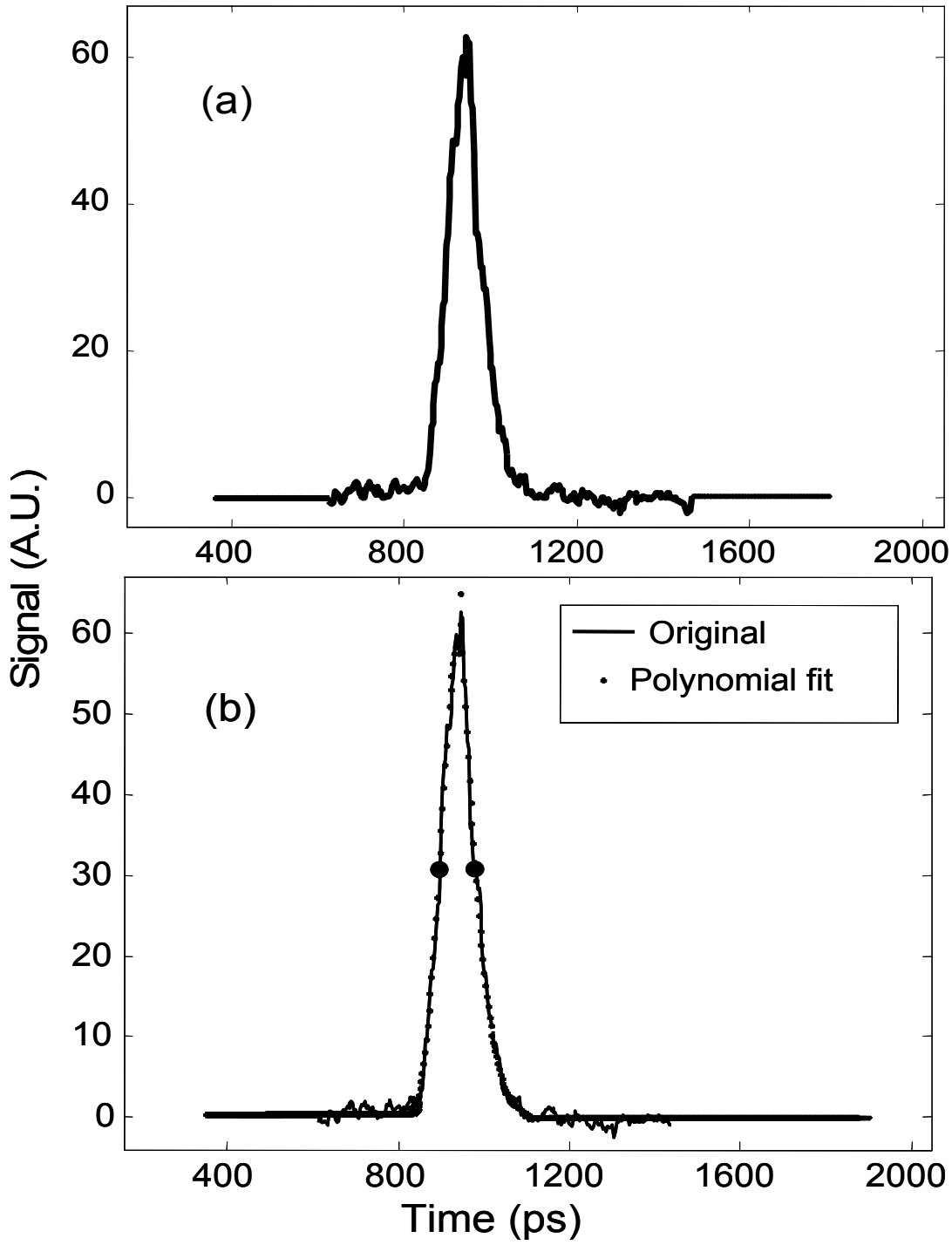

Figure 4.5: (a) the extracted signal from the 50-shot averaged signal subtracted from background. (b) The dashed dot line represents polynomial fit of degree 4 of the extracted signal and the solid line denotes the extracted signal itself. The two big black dots represent the locations of the half magnitude which was used to calculate the full width at half maximum (FWHM).

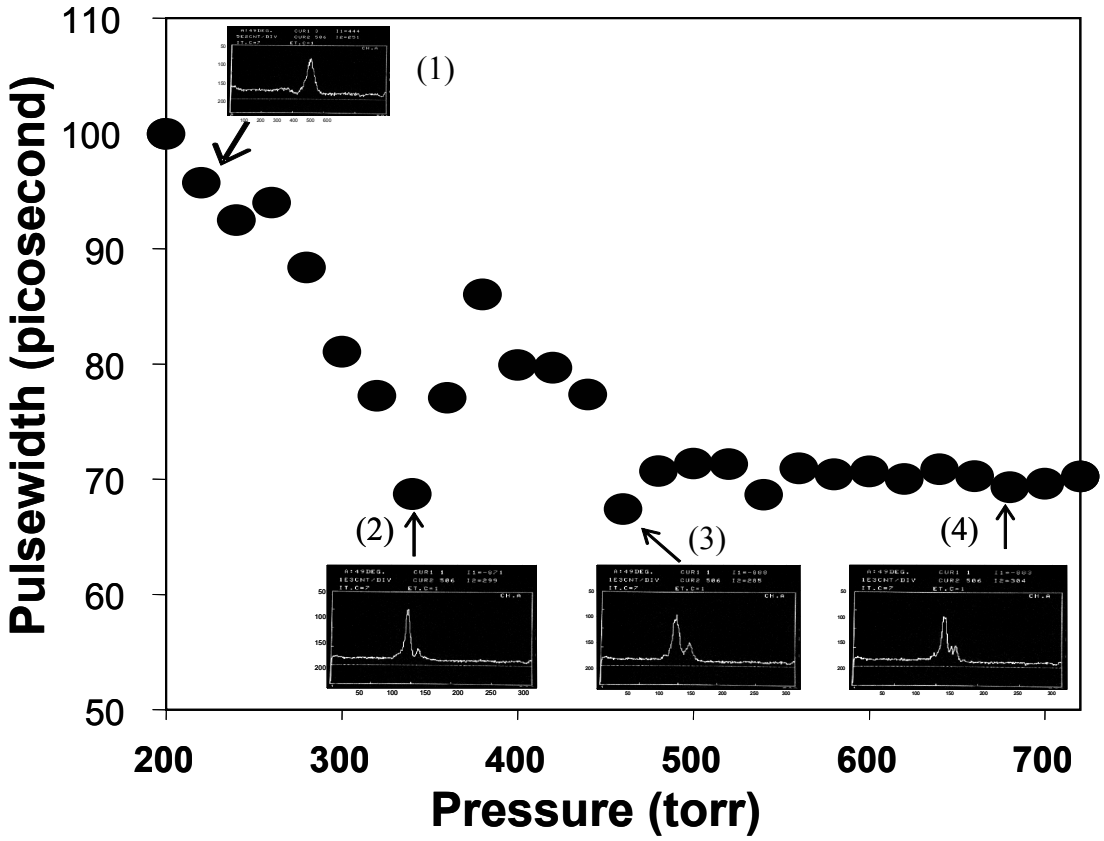

Figure 4.6: The pulse-width of the untrapped portion (cone beam) from 10Hz, 100ps, 1064nm, 350mJ Nd:YAG laser pulse versus pressure. Each point was 100 shots averaged. Insets are the streak images at different pressures. The streak camera was calibrated with 3.2ps/pixel.

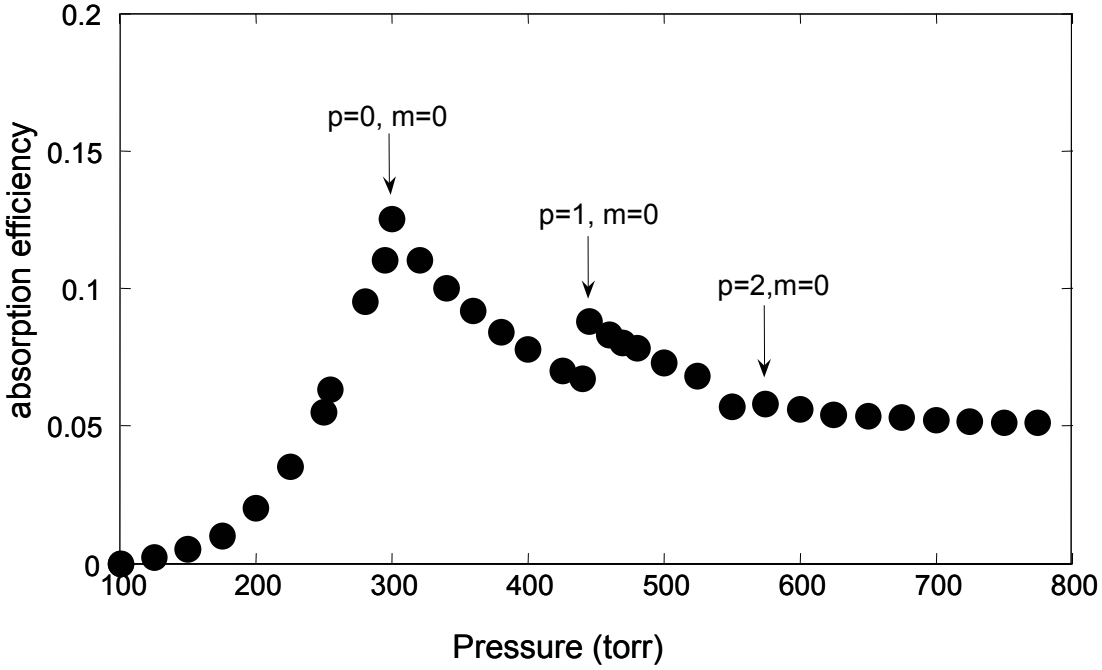

Figure 4.7: Calculation of absorption efficiency versus pressure. Parameters used in the calculation are the same as in the experimental results of Figure 4.1 and 4.2. The two peaks in the absorption curve correspond to coupling to the p=0, m=0; p=1, m=0 modes. Peak vacuum intensity of 5 X 10^{13}W/cm^2, $\gamma=15^0$, 1064nm, 100ps. The pulse peak occurs at ~120ps.

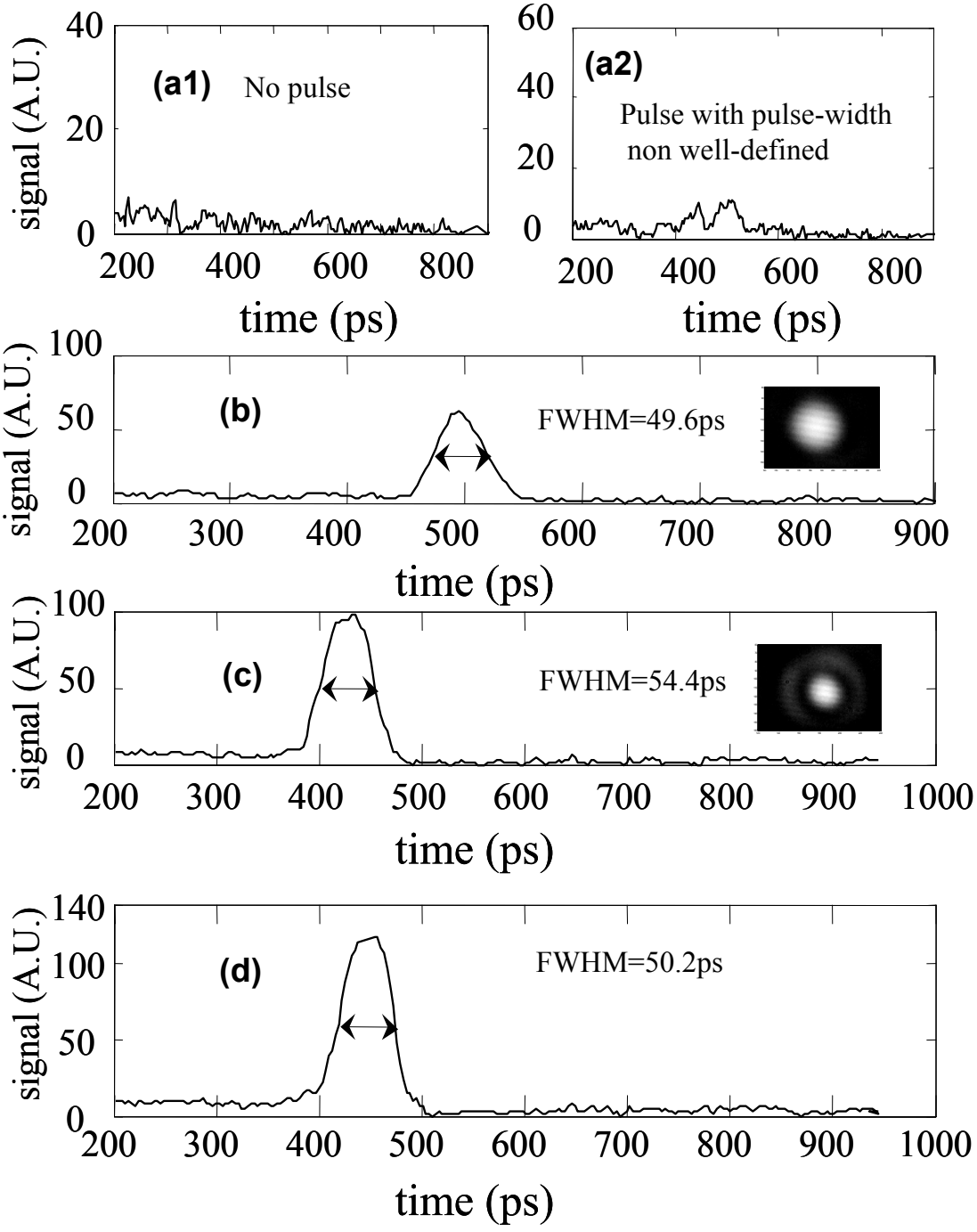

Figure 4.8: Sample pulse traces of trapped beams under pressure of (a) 300torr, (b) 340torr, (c) 460torr, and (d) 600torr.

Chapter 5: Plasma waveguides efficiently generated by Bessel beams in elongated cluster gas jets

5.1 Introduction

Plasma waveguides have been produced by electrical discharge in capillaries, both pre-filled with gas [1] and not [2], in imploding Z-pinches [3] and by plasma structures generated through laser-driven non-equilibrium radial shock waves in gas targets [4] and in variations of this technique [5-6]. In addition, short waveguides have been generated by ponderomotive force expulsion of electrons by relativistically self-guided pulses [7]. Most recently, highly ionized waveguides have been generated in clustered gases, with long waveguide plasmas generated through the plasma evolution following the self-guiding and strong coupling [8] of a pulse injected into the end of a long cluster gas jet [9]. In that experiment, plasma waveguides are efficiently generated with millijoule level femtosecond pulses, which experience absorptions up to 85%.

In this chapter, we show that plasma waveguides can be also generated in clustered gases by line-focusing a much longer duration laser pulse into an extended clustered gas jet. Previously, the line-focus technique has been limited to heating unclustered backfill or gas jet targets with line-focused pulses produced by axicons (Bessel beam heating) [4, 6, 10] or by cylindrical lenses [5], but pump absorption efficiency in these targets is typically less than a few percent. For very high backfill gas densities at atmospheric pressure and beyond ($>3\times10^{19}$ atoms/cm^{-3}) absorption can be ~10%, but the resulting electron densities can be much too high for some

applications such as laser-driven resonant wakefield acceleration [11]. As a special case for Bessel beams, there are some pressure ranges in non-clustered gases where absorption can be resonantly increased depending on axicon geometry, pump laser intensity, pulsewidth, and wavelength [10] as discussed in chapter 4, but absorption still remains below ~15%, and the choice of target gas density is limited by the resonance condition.

In this chapter we show that using clustered gas targets and long 100ps heating pulses, absorption can be non-resonantly increased by as much as a factor of ~10 compared to unclustered gases of the same volume average atomic density. We measure maximum long pulse absorptions of 35%, which is only 2 to 3 times less than the absorption levels of femtosecond pulses. Using clustered gas targets and long pulse irradiation, we can make small diameter plasma waveguides with on-axis electron densities near 10^{18}cm^{-3}, significantly lower than with non-clustered targets. A signature feature is that a 100ps pulse appears to be a surprisingly efficient heater of the cluster plasma despite the fact that individual clusters disassemble to below critical density on a timescale of only a few hundred femtoseconds, and thus are expected to be strongly absorbing only during that period [12].

In unclustered gas, efficient collisional breakdown for plasma waveguide generation requires high gas density N_0 due to the early time exponential growth of electron density $N_e(t) \sim N_{e0}\exp(SN_0t)$ where N_{e0} is the initial electron density and S is the collisional ionization rate. N_{e0} can be generated by optical field ionization (OFI) [13] in the main heating pulse, or through the use of a separate pre-pulse [5]. Alternatively, it can be provided by an auxiliary electrical discharge [6] in advance of

a laser heater pulse. In most practical cases, N_{e0} constitutes only a very small pre-factor such that $Z_{init}=N_{e0}/N_0 \ll 1$, where Z_{init} is the initial effective degree of ionization. Under these conditions, after a few e-folding times of N_e growth, saturation begins and memory of N_{e0} is lost, with N_0 as the dominant factor in determining the end condition [14-15]. The requirement for large N_0 results in typical minimum electron densities in plasma waveguides, after radial hydrodynamic expansion, higher than ~$5\text{x}10^{18}\text{cm}^{-3}$, which is not optimum for some applications, most notably resonant laser wakefield acceleration. For resonant excitation of wakefields, the goal is to match the laser pulse width to the plasma period. For 50-100fs pulses, typical of today's high power Ti:Sapphire laser systems, the desirable electron density is ~10^{18}cm^{-3} or less [16]. Using clustered gas jet targets and 100ps axicon-focused Bessel beam pulses, we can achieve long, efficiently generated plasma waveguides at such low densities. The use of clusters strongly increases the effective level of preionization so that $Z_{init} \gg 1$. Since further growth in ionization over most of the laser envelope starts near saturation, sensitivity to N_{e0} is no longer lost. This is discussed in more detail in section 5.5 below.

The clusters in our experiment are assemblies of ~10^3 to 10^7 atoms held together by mutually-induced polarization forces, or van der Waals bonding [17]. Such inter-atom forces become significant under sufficient gas cooling. In our experiment, the cooling and collision processes leading to cluster formation occur when high pressure gas adiabatically expands into vacuum through a supersonic nozzle. Typical cluster radii a are in the range ~10–100Å such that $ka \ll 1$, where k is the laser vacuum wavenumber. For greater numbers of atoms and larger values of a

such that the assembly size approaches the laser wavelength, the convention has been to use the term *droplet* rather than *cluster*.

5.2 Experimental setup

Figure 5.1 shows the experimental setup. Cluster jets were produced using a pulsed valve and a slot nozzle with an exit orifice of dimension 0.5mm by 1.2cm. High valve backing pressures and low temperatures favor the formation of larger clusters. The pulsed valve body is encased in a liquid nitrogen-cooled copper jacket so that the pre-expansion gas can be cooled as low as -120C. Valve backing pressure and temperature ranged from 10 to 80bar and -120C to room temperature. The valve temperature was finely controlled to within ±0.2C of any set point in this temperature range by two solid-state cartridge heaters encased in the copper jacket, which operate in tandem with the liquid nitrogen cooling [18]. The density of the clusters in our jet occupies a wide range ~ 10^{12}-10^{17} clusters/cm^3, and the volume average electron density after heating by a laser pulse and subsequent cluster plasma expansion can be in the range 10^{16}-10^{20}cm^{-3}. This density control is achieved by controlling the cluster size and density through the valve backing pressure and temperature.

An all-optical method to measure cluster size and density was developed to characterize cluster jets [19]. The method uses measurements of Rayleigh scattering and interferometry in combination. Figure 5.2(a) shows an image of a weak 10ns duration 532nm probe beam propagating along the long axis of the jet and scattering from clusters. A sequence of Rayleigh scattering images are shown in Fig. 5.2(b) for fixed backing pressure of 400psi and variable valve temperature, with lineouts of

these images seen in Fig. 5.2(c). It is seen that the cluster flow becomes quite uniform as the valve is cooled to 200K and lower, and a very sharp ~0.5mm falloff in scattering yield occurs the ends of the jet. Figures 5.3(a) and 5.3(b) show a sequence of plots, obtained using the method of reference [19], of average cluster size and cluster number density as a function of valve backing pressure for four different valve temperatures. The wide control provided for cluster size and cluster density is evident.

The laser used in this experiment is a mode-locked Nd:YAG system with a wavelength of 1064nm, pulsewidth of 100ps and energy up to 800mJ. The detail is described in Chapter 2. The pump beam was focused by an axicon with a base angle $\alpha = 25°$, generating a ~1.3cm long plasma column 2mm above and along the axis of the cluster nozzle orifice. The beam resulting from focusing by the axicon, also called a Bessel beam [10], has a transverse profile invariant along the optical axis, while the length L of the high intensity central maximum is determined by the beam radius a and the axicon base angle α according to $L = a(1/\tan\gamma - \tan\alpha)$, where $\gamma = \sin^{-1}(n\sin\alpha) - \alpha$ is the angle of approach of the axicon rays to the beam axis [15]. In our case L=1.6cm for $\alpha = 25°$, axicon BK-7 glass refractive index n=1.507 at λ=1064nm, and 2a=1cm. The longitudinal intensity distribution along the axicon line focus has a peak located near the axial mid-range and decreases toward the two ends. This occurs because the input beam profile is mapped onto the focal line with a radial weighting factor: the weighting factor is zero for the input beam center, which maps to a point closest to the axicon vertex, and the input beam periphery (where intensity decreases to zero) is mapped farthest from the axicon vertex [15]. In the experiment, the ends of

the 1.6cm long line focus overlap the ends of the cluster jet (as defined in the Rayleigh scattering images of Fig. 5.2(b)) so that there is no section of the jet left un-ionized. The peak vacuum intensity in the central maximum of the Bessel beam is ~ 6 X 10^{13}W/cm^2 corresponding to the maximum energy used of 415mJ, although in practice the breakdowns were more uniform with less energy. The range of intensities used is sufficient for the optical field ionization (OFI) of neutral argon. The OFI electrons act as a seed for the subsequent cascade avalanche ionization of the cluster. An image of the line breakdown in an elongated argon cluster jet is shown in Fig. 5.4. The ring on the screen at left is nonlinear fluorescence of the locus of rays from the axicon which heat the plasma and are transmitted through it, and the central spot is from the central part of the input beam which passes through a 2.5mm diameter hole in the centre of the axicon. (This hole is used in experiments where secondary delayed pulses are injected through the axicon and coupled into the plasma waveguide and optically guided [4, 15]). Visually, Bessel beam breakdowns of the clustered gas jet are significantly brighter than similar breakdowns in unclustered jets or in backfill targets.

The time- and space-resolved evolution of the plasma waveguide is measured by a probe pulse directed perpendicularly to the waveguide axis and into a folded wavefront interferometer [20]. The probe was obtained by splitting off a 1mJ portion of the 100ps main pulse and directing it to an optical delay line, which provides the time resolution through pump-probe delays of -1ns through +11ns. The diameter of the probe beam is 1.6cm, which is big enough to fully contain the plasma channel. After passing through the plasma channel, the probe was directed to a lens pair

imaging system with the first lens of focal length f1 placed a distance f1 away from the plasma, the second lens (f2) placed a distance f1+f2 away from the first lens, and the probe image formed a distance f2 beyond the second lens with magnification f2/f1=2. An uncoated BK7 wedge in the probe beam path prior to the image plane was used to produce two angularly separated beams. At the image plane the two beams form complementary interferograms whereby a portion of the beam unperturbed by the plasma overlaps with a portion of the beam passing through the plasma to generate interference fringe shifts due to the plasma refractive index profile. At the image plane a 4X microscope objective coupled to CCD camera was used to capture the interferogram, for an overall system magnification of 8X. The phase information encoded in the interferogram was extracted with a fast Fourier transform technique, and the phase was further processed by Abel inversion, assuming cylindrical symmetry, to recover electron density profiles [20-22]. Insets to Figure 5.1 show typical interferograms of the central region of the waveguide and the end.

5.3 Experimental results

Figure 5.5(a)-(c) shows grayscale images of the extracted electron density at 3 probe delays for the case of argon at valve temperature -100C, backing pressure of 800psi and pump laser energy of 150mJ. It is notable that for waveguides of similar electron density produced in non-clustered argon, the pump energy required was ~500mJ *and* a seed gas (N_2O at 10-20% partial pressure) was needed to provide OFI electrons to seed the avalanche breakdown [20]. In the present case, the lower laser

energy and lack of a seed gas means a much reduced OFI rate. But the much higher local atomic density in a cluster ensures that, even with the lower yields of first generation OFI electrons, the subsequent collisional breakdown is far more vigourous than in the seeded unclustered gas case. This will be seen in the later simulations.

Figure 5.6 shows plots of electron density vs. radius, as a function of probe delay from the central region of the waveguide, for two settings of the argon cluster jet. In Fig 5.6(a), P_{valve}=800psi, T_{valve}= -100C and laser energy is 150mJ. By ~500ps, a hollow electron density profile develops, and a laser-induced shockwave propagates radially outward. By 2ns, the on-axis electron density has dropped below ~$10^{18}cm^{-3}$. The electron density falloff at radial distances beyond the shock is more extended than for laser-plasmas generated in unclustered targets, owing to both conduction and radiation precursors [23-24] and a reduced laser intensity threshold for strong ionization of clusters [12]. The latter effect means that subsidiary off-axis radial maxima of the Bessel beam are effective in plasma generation. In Fig. 5.6(b), P_{valve} was reduced to 500psi, also with T_{valve}= -100C. In order to make a stable, continuous channel, it was necessary to increase the pump laser energy to 230mJ. Under these conditions, it is seen that the peak electron density does not occur until ~500ps past the pump pulse, and the central electron density dip does not occur until ~1ns after the pump pulse. These results illustrate that cluster target control plays an extremely significant role in determining the amount of pump energy required for desired waveguide parameters. In this case, increasing the jet backing-pressure results in a very large pump-energy-savings.

We also generated plasma waveguides in a nitrogen cluster jet. Figure 5.7 shows the evolution of the nitrogen cluster plasma under P_{valve}= 900psi and T_{valve}= -100C with pump laser energy of 415mJ. These higher levels of backing pressure and pump energy were required for stable continuous channels. It shows a similar evolution as in the argon cluster plasma, with the density dip appearing at ~500ps, and the central density dropping to $<10^{18}cm^{-3}$ after ~ 2ns. By comparison, in unclustered nitrogen, both from gas jets and in backfill targets, no breakdown occurred for the pure gas using axicons and 100ps pulses, and only with significant additional partial pressure of N_2O (>20%) was breakdown possible.

The results of this experiment show that clustered gases achieve breakdown to high degrees of ionization much more readily than unclustered gases. One would expect that an absorption measurement would be consistent with this observation. Such a measurement was performed by collecting the cone of rays transmitted by the plasma (shown in the schematic of Fig. 5.1 and shown projected onto the screen in Fig. 5.4 with a second axicon after the plasma breakdown, and delivering the light to an energy meter. The input beam energy was directed to the axicon by a 90 degree 1064nm mirror with a central hole of slightly larger diameter than the hole in the axicon. Therefore, for this measurement the central beam spot shown in Fig. 5.4, which does not participate in plasma generation or heating, was not collected. Figure 5.8(a) shows absorption vs. backing pressure of argon and nitrogen clusters for T_{valve}=-100C and laser energy of 315mJ and Fig. 5.8(b) shows absorption as a function of pump energy for argon clusters (P_{valve}=800psi and T_{valve}=-100C) and for argon gas (P_{valve}=800psi and T_{valve}=25C). The level of absorption in unclustered

nitrogen jets was below the sensitivity level of the measurement. It is seen that the maximum absorption is approximately 35%. While not at the level of >80% absorption of femtosecond pulses in clustered gases [9] the absorption of these long 100ps pulses is much greater than that achievable in unclustered gas jets.

5.4 Calculations of long pulse breakdown of cluster jets

We now discuss the result that the use of clustered gas significantly enhances pump pulse absorption and waveguide generation, even though the few hundred femtosecond cluster disassembly time is greatly exceeded by our 100ps pump pulses. Our earlier femtosecond time-resolved measurements showed that heating of few hundred angstrom diameter clusters by 10^{15}W/cm^2 , λ=800nm, 70fs pump pulses induces an ultrafast cluster plasma explosion, wherein the peak electron density drops from solid levels of ~10^{23}cm^{-3} to subcritical levels below ~2x10^{21}cm^{-3} within ~0.5ps [12], and the plasmas from nearby cluster explosions merge in ~10-100ps, depending on cluster density. The implication of this for the current experiment is that the majority of the 100ps pulse envelope will encounter low subcritical density, uniform plasma arrived at from expansion and merging of individual cluster explosions that are initiated very early in the pulse. Therefore, an explanation for the surprisingly high absorption efficiency in the current experiment resides in the cluster plasma dynamics in the leading edge of the 100ps pump pulse. Figure 5.9 shows results from our laser cluster hydrodynamic code [25], for a 200 Å argon cluster exposed to a 100ps, λ=1064nm pulse over a range of intensity. The code solves the plasma hydrodynamic equations coupled to the equation $\nabla\cdot(\varepsilon\mathbf{E})=0$ for the electric near field,

where $\varepsilon(\mathbf{r},t)$ is the space- and time-dependent plasma dielectric function and $\mathbf{E}(\mathbf{r},t)$ is the self-consistent electric field from the laser and plasma. The near field model is well satisfied here for $ka<<1$, where k is the laser wavenumber and a is the cluster radius. The code accounts for OFI and collisional ionization and heating, thermal conduction and uses a time-dependent collisional radiative model for the ionization dynamics. The pulse temporal envelope is taken to be Gaussian. The figure plots the log of cluster peak electron density as a function of time for peak pulse intensities in the range 10^{13}-10^{14}W/cm^2, corresponding to the range of experimental intensities in the central maximum of the Bessel beam. The pulse starts near t = -300ps at $1.5\text{x}10^{-11}$ of peak intensity (for example, the starting intensity is 1500W/cm^2 in the case of the peak 10^{14}W/cm^2 pulse), where the initial electron density is taken to be 2 electrons/cm^3, effectively zero over the cluster volume. The results are insensitive to this choice of negligible initial electron density. The pulse peaks at t=0. It is seen that extremely strong cluster ionization occurs in the far leading edge of the pulse, saturating to an average degree of ionization Z_{avg}~8 corresponding to the Ne-like Ar^{8+} ion, which is quite stable against further ionization to the next higher stage. The ionization onset time varies over a ~40ps range as the peak intensity varies from 10^{13} to 10^{14}W/cm^2, but the onset always remains in the far leading edge of the pulse. The other crucial occurrence is that an exploding cluster plasma, once it has dropped below critical density, can cool by expansion during the leading edge of the long pulse, well before the pulse intensity increases sufficiently to contribute to heating. During this phase, the expanding and merging cluster plasma is also cooled via thermal conduction to the neutrals and weakly pre-ionized gas on the periphery of the

main plasma. From single cluster calculations alone [25] (ignoring thermal conduction to the gas jet periphery), expansion cooling can drop the temperature from a peak of a few hundred eV down to a few eV.

The conclusion from these calculations is that essentially the full 100ps pulse envelope encounters highly ionized, uniform, and relatively cold plasma as its effective initial target. From this perspective, the clustered gas can be viewed as enabling a supercharged pre-ionization scheme. In typical pre-ionization schemes, the initial ionization level per atom is much less than unity, $Z_{eff}<<1$ [5, 6]. With clusters as the target, one can have $Z_{eff}>>1$, as seen in Fig. 5.9. The effects of this on the further breakdown and heating of the target can now be investigated by utilizing our self-consistent Bessel-beam plasma interaction code [10], which simulates axicon pulse heating of gas-density plasmas. In this calculation, the gas density plasma hydrodynamic equations are solved coupled to the equation for the *z*-propagating Bessel beam, $\square$, where the electric field is given by $E(\mathbf{r}_\perp, z, \omega) = e^{i\beta z} u(\mathbf{r}_\perp, \omega)$, $\kappa^2(\mathbf{r}_\perp, \omega) = k^2(1 + \delta_{plasma}(\mathbf{r}_\perp, \omega) + 4\pi\chi(\mathbf{r}_\perp, \omega)) - \beta^2$ is the square of the local transverse wave number, χ is the total atomic and ionic susceptibility and δ_{plasma} is the plasma contribution to the medium response. In the above equations, $\square$ is the Laplacian in the transverse coordinate $\mathbf{r}_\perp$, $k=\omega/c$ is the vacuum wavenumber of the laser, and β is the wavenumber along the propagation axis *z*.

For this calculation, we use conditions corresponding to experimental parameters of Fig. 5.8: axicon ray approach angle γ=15°, λ=1064nm, a peak intensity of $2.5\text{x}10^{13}\text{W/cm}^2$, and gas densities $N_n = 0.7\text{ x}10^{19}$, $1.0\text{ x}10^{19}$ and $1.4\text{x}10^{19}\text{cm}^{-3}$,

corresponding to backfill pressures of 200, 300, and 400torr, and shown in Figs. 5.10, 5.11, and 5.12 respectively. The figures show the time dependent absorption for initial ionization levels in the range $Z_{init}= 10^{-7}$ through $Z_{init}=8$. This corresponds to the initial plasma conditions encountered by a long pulse interacting with targets spanning the range of initially unclustered gas to a gas of large clusters. Overlaid on these curves is the incident pulse envelope, normalized to unity. The tables inset in the plots give the curve legend for the various values of Z_{init} and the total absorption fraction, η, which is the integral of each curve. It is seen for 200torr (Fig. 5.10) that absorption for the 'clustered' case of $Z_{init}=8$ (η=0.10) is ten times greater than for the 'unclustered' case of $Z_{init}= 10^{-7}$ (η=0.012). For 300torr (Fig. 5.11), the maximum absorption is η=0.33, while it decreases at 400torr (Fig. 5.12) to η=0.25. In both the latter cases, a high degree of initial ionization increases the subsequent absorption by approximately a factor of 3 compared to the low initial ionization case. In the higher density case, the absorption is somewhat less owing to the incipient exclusion of the axicon field from the plasma caused by the increase in the effective critical density $N_{cr,eff}= N_{cr}\sin^2\gamma$ seen by the Bessel beam [10]. In general, low average density cluster gases show the greatest relative absorption enhancement over their non-clustered counterparts, while the largest absolute absorption takes place at intermediate pressures, before density is large enough to effect Bessel-beam field exclusion. In all cases the absorption in clustered gases, represented by the $Z_{init} >>1$ cases, is significantly greater than in neutral gases of equivalent density, where conventional pre-ionization $Z_{init} << 1$.

5.5 Conclusions

We have demonstrated that clustered gases are an excellent medium for use in plasma waveguide generation using 100ps long pulse axicon-generated Bessel beam pump pulses. The plasma waveguide space and time evolution is measured using picosecond interferometry. The resulting waveguides can have both central densities as low as ~10^{18}cm^{-3} and small diameter, a desirable but hard to achieve combination for hydrodynamic shock waveguides using conventional gases, or for other techniques such as discharge capillaries. A main advantage for which cluster targets are well known, namely extremely efficient absorption of femtosecond laser pulses, is shown to extend to pulses that are significantly longer than the timescale for cluster explosive disassembly. The long pulse absorption efficiencies can be more than a factor of 10 greater than in unclustered gas targets of the same volume average atomic density. The maximum long pulse absorption observed in cluster jets under our range of conditions was 35%. This is due to the fact that a clustered gas is very strongly preionized in the far leading edge of a long pulse; the subsequent pulse envelope acts to heat a locally uniform, cool plasma which is already near ionization saturation. From this perspective, the use of clustered gases is equivalent to a supercharged pre-ionization scheme for long duration laser pulses.

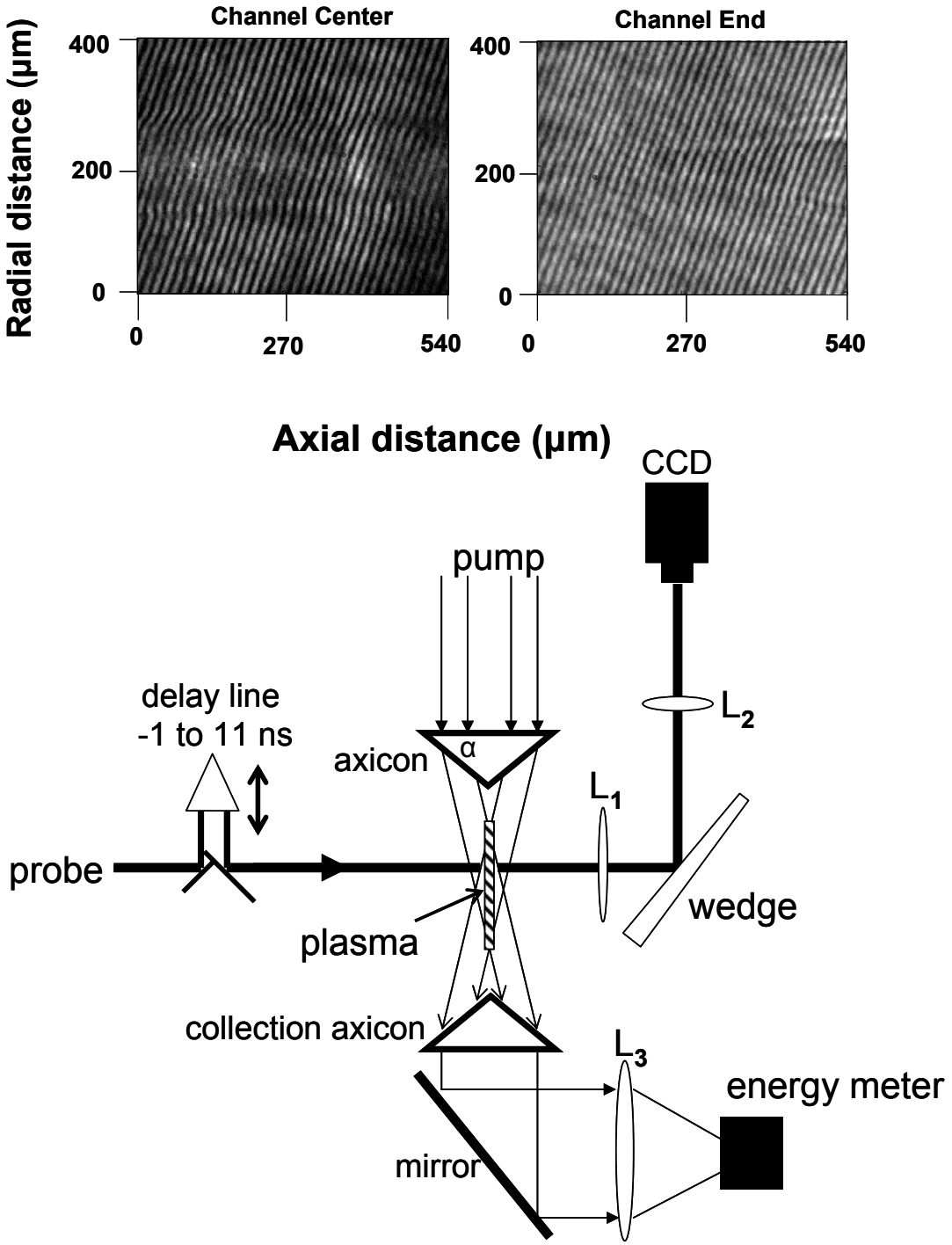

Figure 5.1: Experimental setup, showing waveguide generating axicon with base angle $\alpha = 25^0$ and folded wave front interferometer with variably delayed 1064nm, 100ps, ~1mJ probe pulse, imaging optics and reflection wedge. The collection axicon is used for pump absorption measurements. The insets show typical interferograms of the central region of the waveguide and the end.

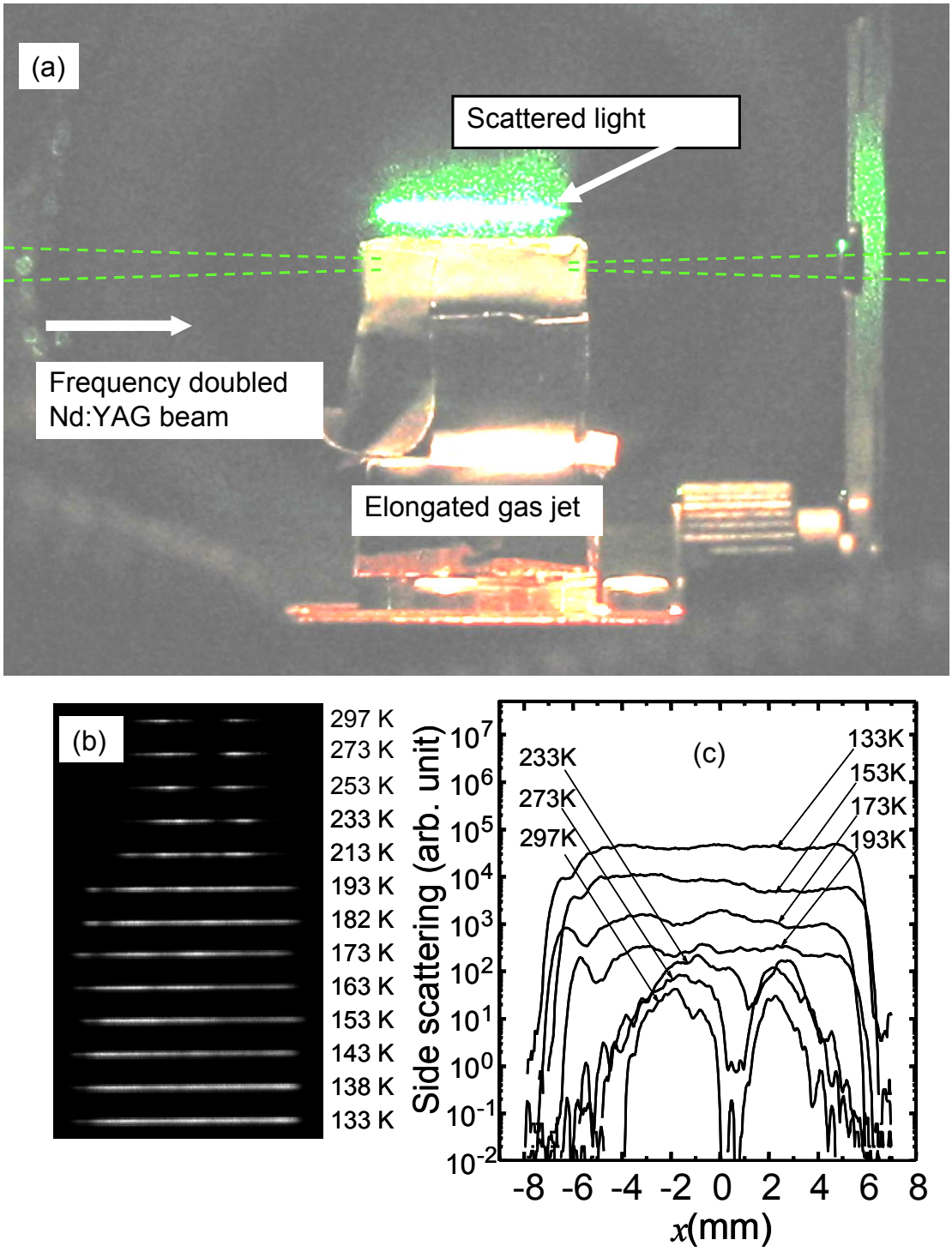

Figure 5.2: Color online (a) Image of weak 532nm beam scattered by elongated cluster jet. (b) Image of scattering zone of cluster jet versus valve temperature, for valve backing pressure of 400psi. (c) Central lineout of the scattering images of (b). It is seen that the uniformity of the cluster flow improves with valve cooling.

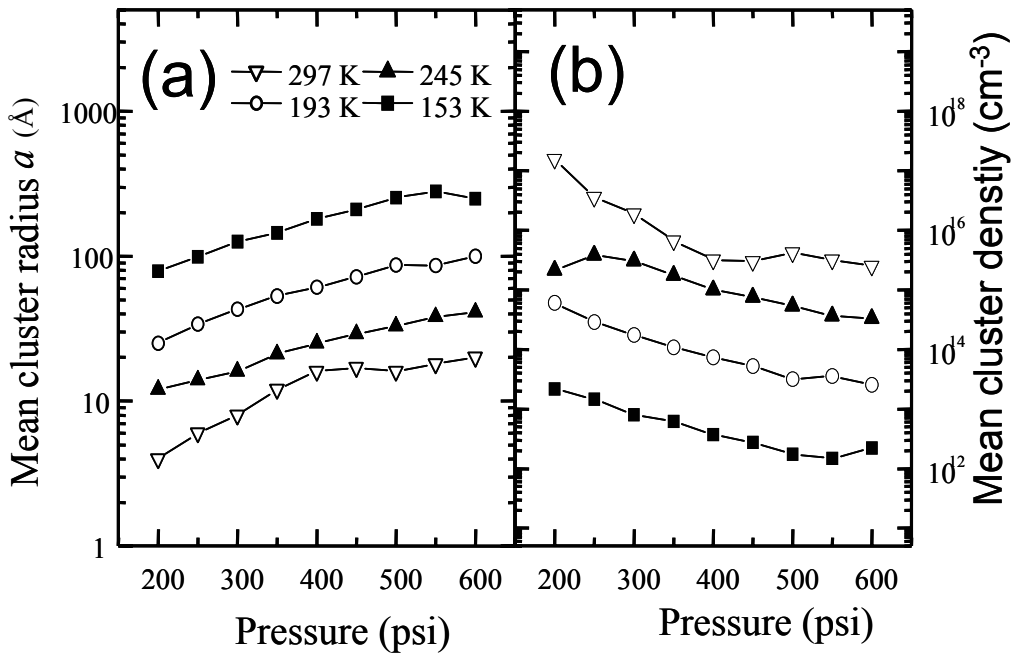

Figure 5.3: Argon cluster (a) size and (b) density versus valve backing pressure for several valve temperatures. The measurement is made using the technique of Ref. [19].

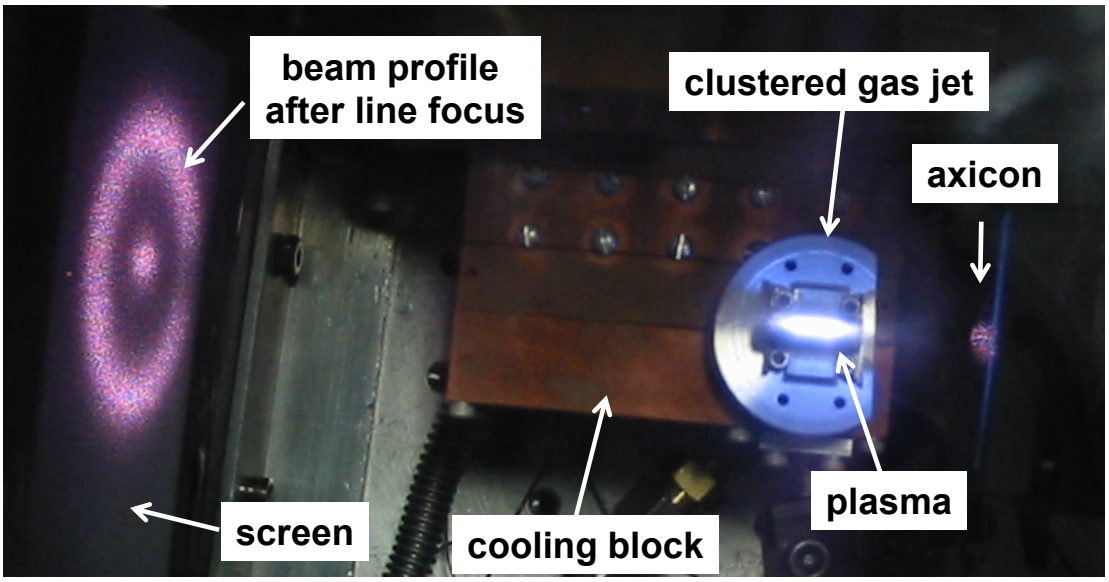

Figure 5.4: An image of the Bessel beam-induced breakdown occurring in an elongated argon cluster jet. The ring on the screen at left is the nonlinear fluorescence of the locus of rays from the axicon transmitted through the plasma. The central spot is from the central part of the input beam that passes through a 3mm diameter central hole in the axicon.

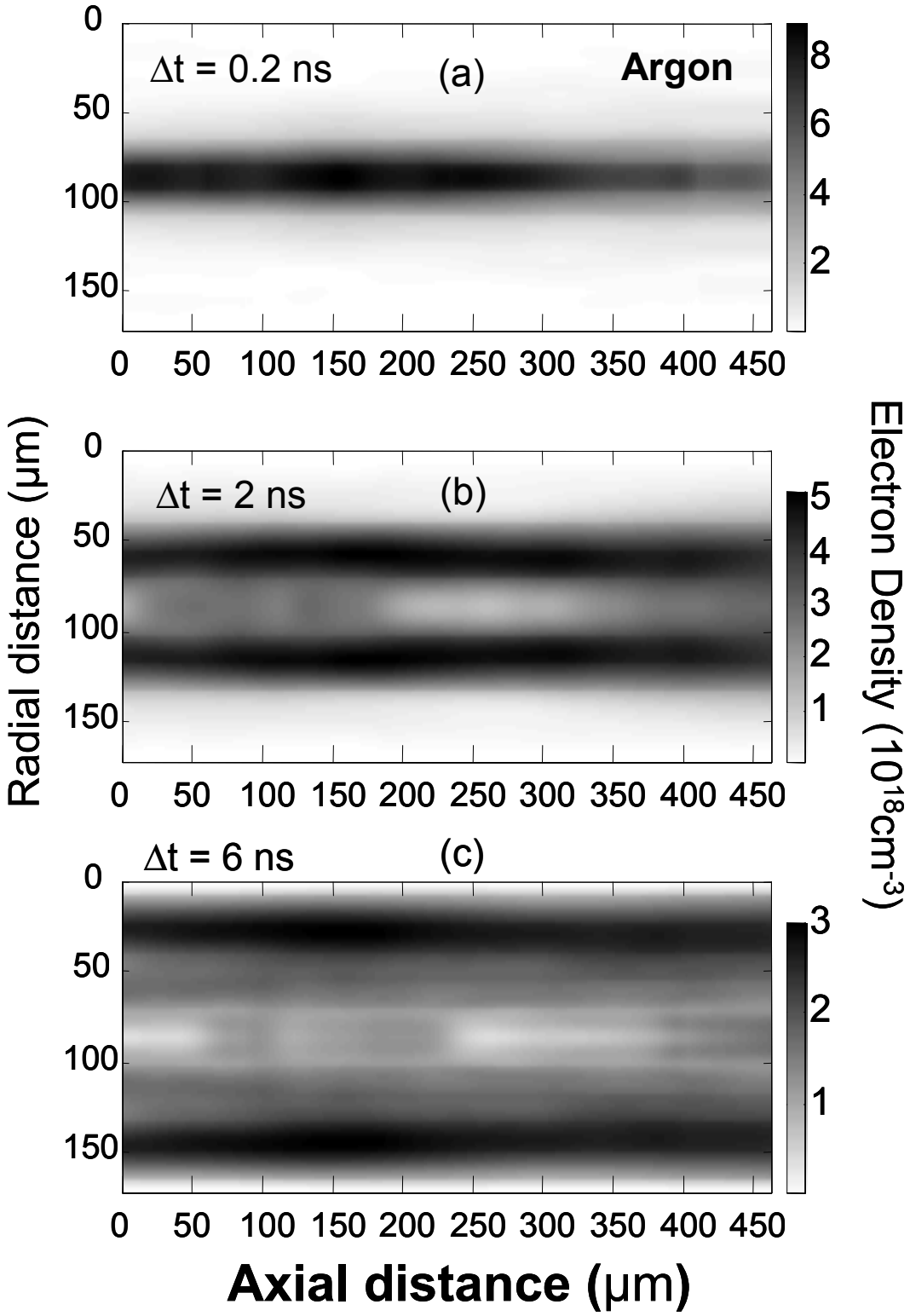

Figure 5.5: Gray scale images of the extracted electron density near the center of the waveguide at probe delays (a) 200ps, (b) 2ns, and (c) 6ns for argon at a backing pressure of 800psi, valve temperature of 173K, and pump laser energy of 150mJ.

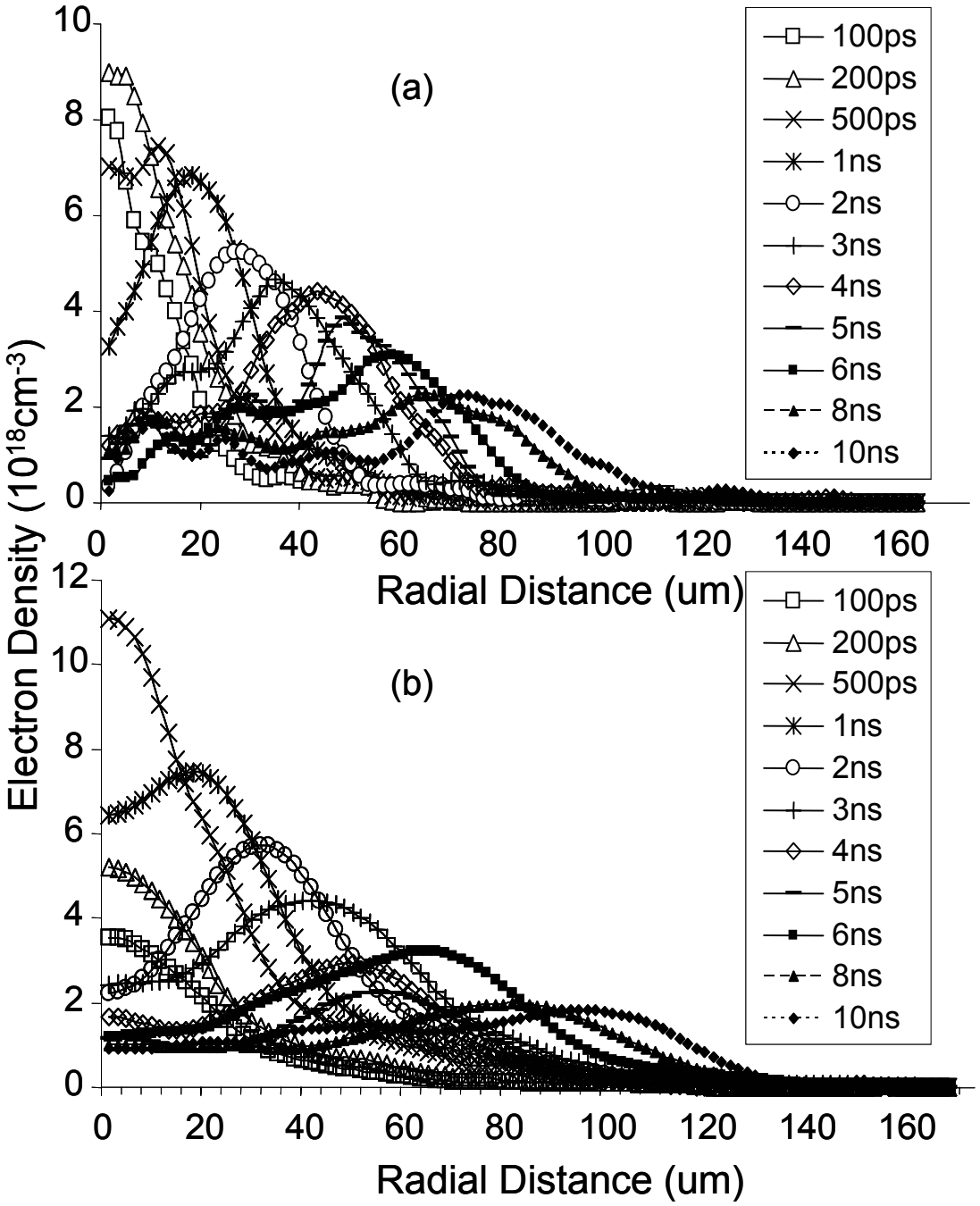

Figure 5.6: Extracted electron density versus radius near the central region of the waveguide as a function of probe delay for argon cluster jets with valve temperature 173K, backing pressure 800psi, and pump laser energy 150mJ; (b) valve temperature of 173K, backing pressure 500psi, and pump laser energy 230mJ.

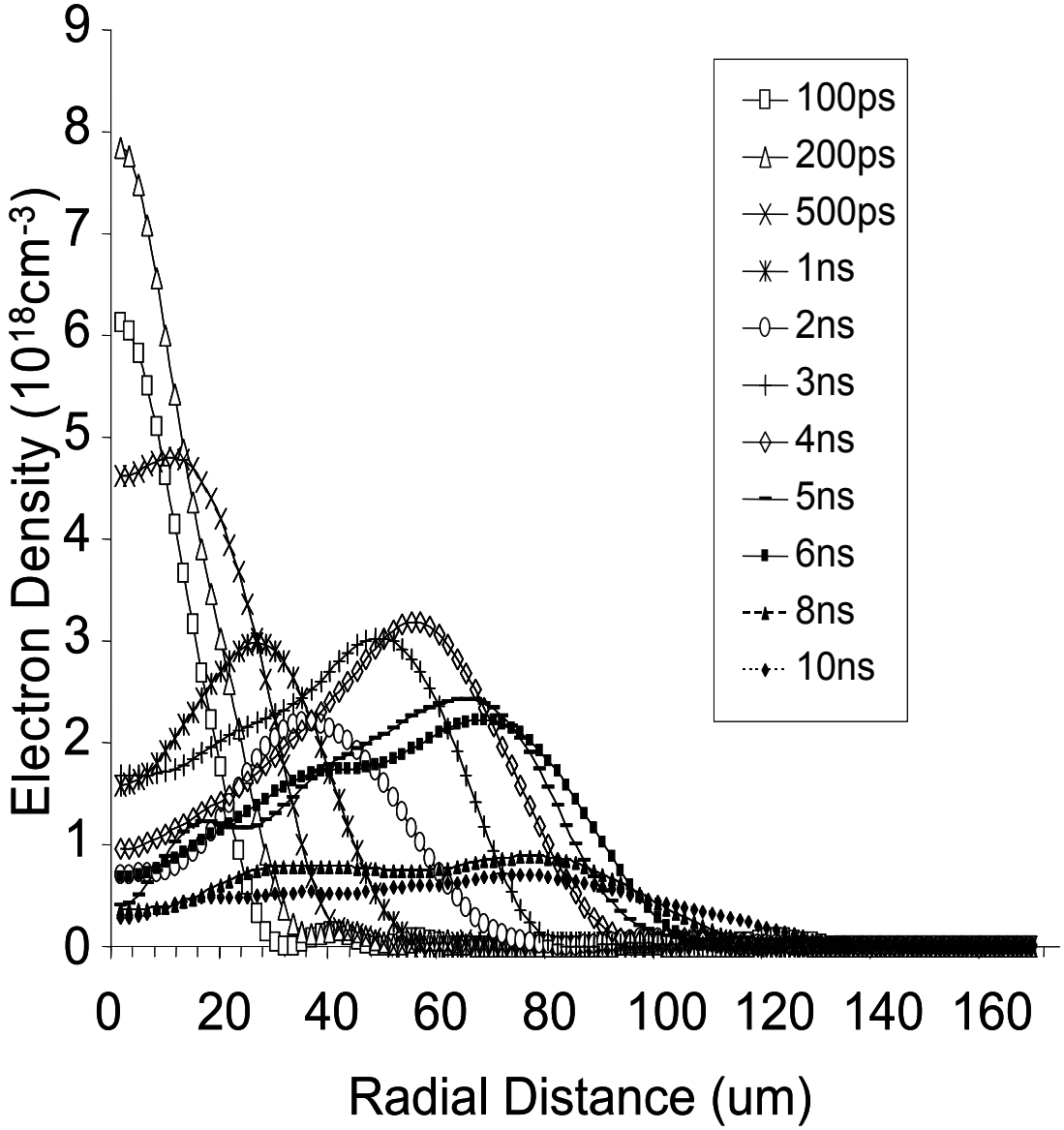

Figure 5.7: Electron density versus radius near the central region of the waveguide as a function of probe delay for clustered nitrogen cluster jets with (a) valve temperature 173K, backing pressure 900psi, and pump laser energy 415mJ.

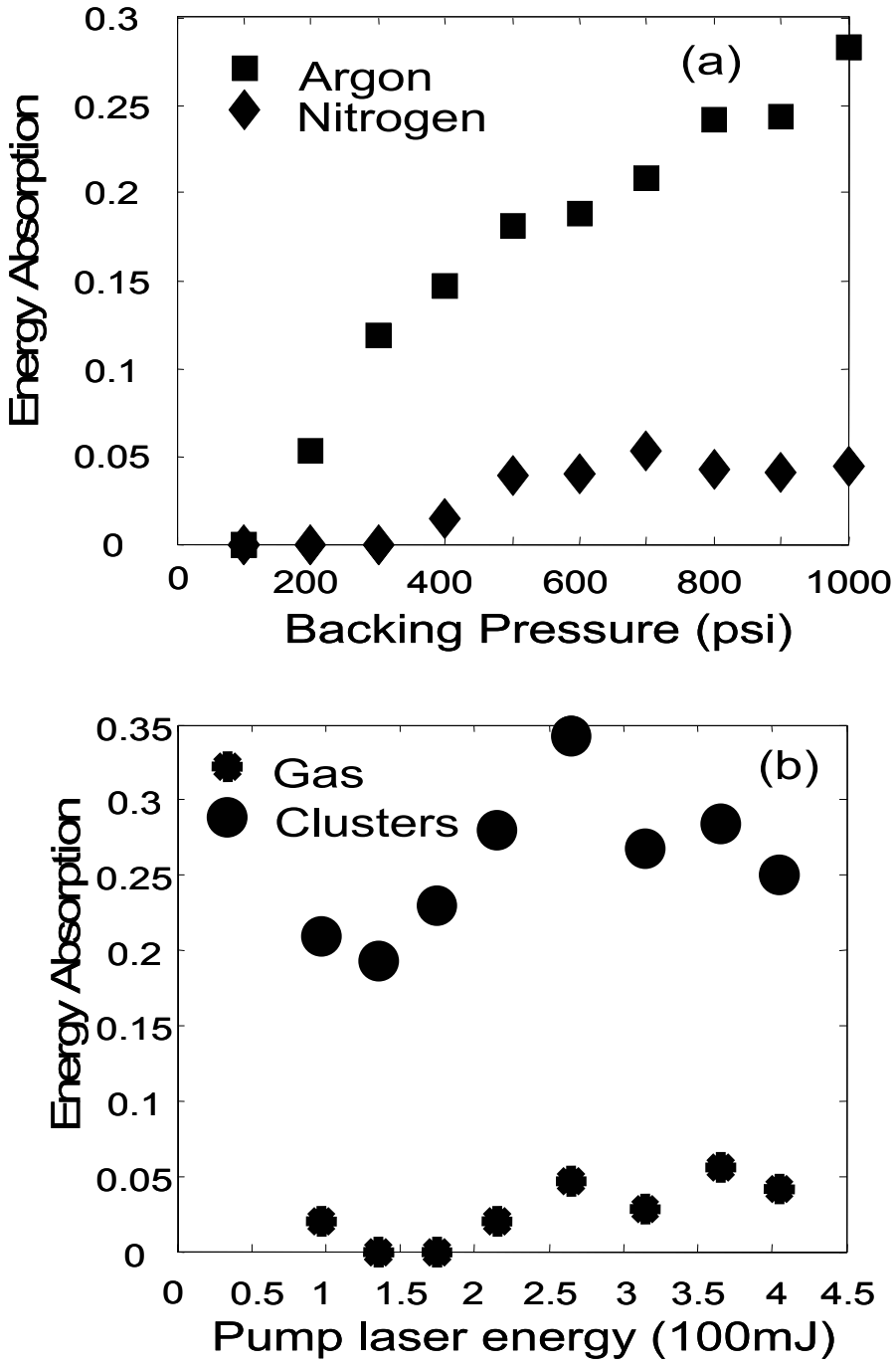

Figure 5.8: (a) Absorption efficiency versus backing pressure of clustered argon and nitrogen for temperature 173K and laser energy 315mJ; (b) absorption efficiency versus pump laser energy for clustered argon at backing pressure 800psi and temperature 173K, and unclustered argon at backing pressure 800psi and temperature 298K.

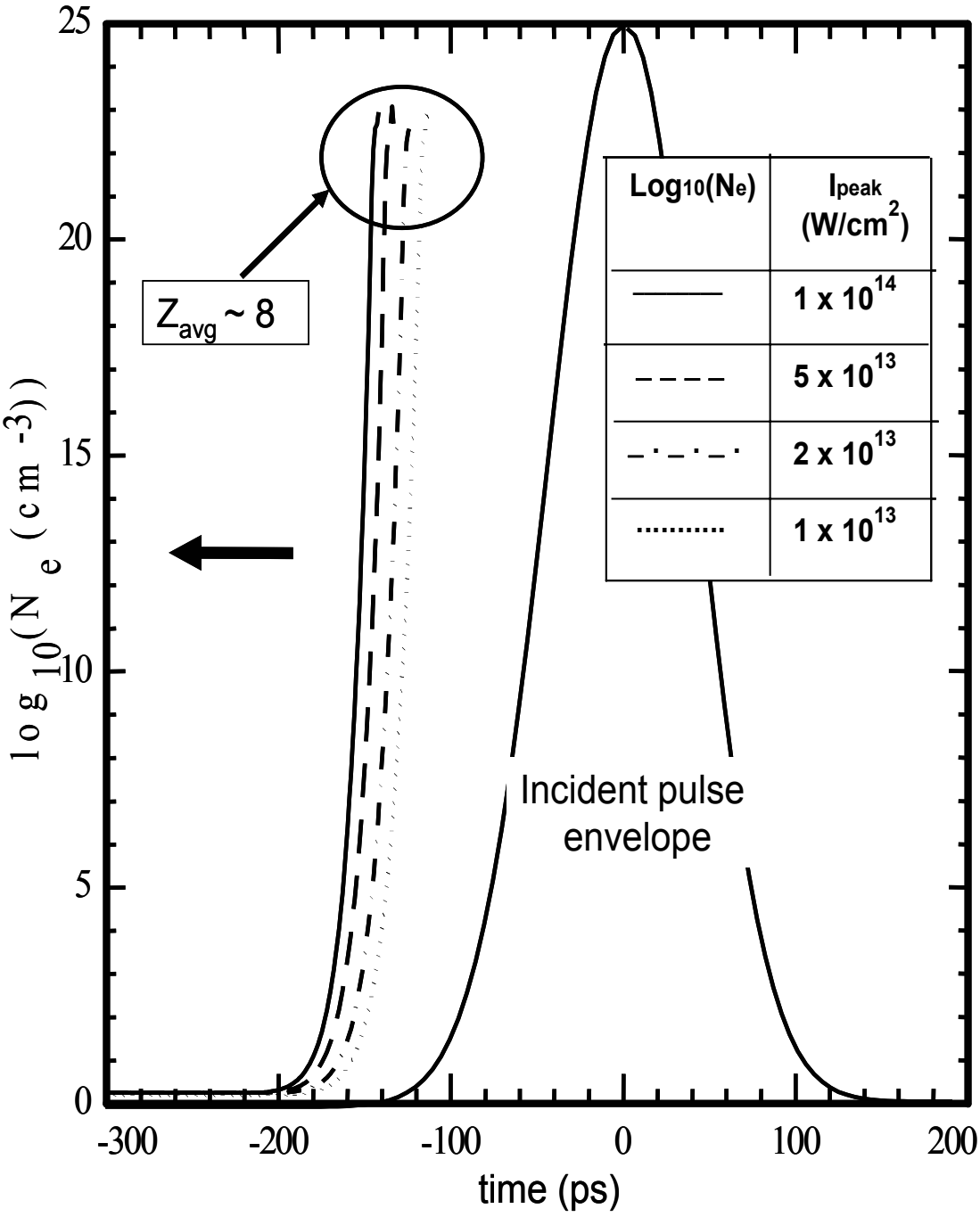

Figure 5.9: Calculation using laser-cluster interaction code [25] of the logarithm of electron density versus time for a 200 Å argon cluster under irradiation of 1064nm, 100ps pulses of intensity 10^{13}, $2X10^{13}$, $5X10^{13}$, and 10^{14}W/cm^2. The effective degree of ionization saturates near Z_{init}~8 in the very early leading edge of the pulse.

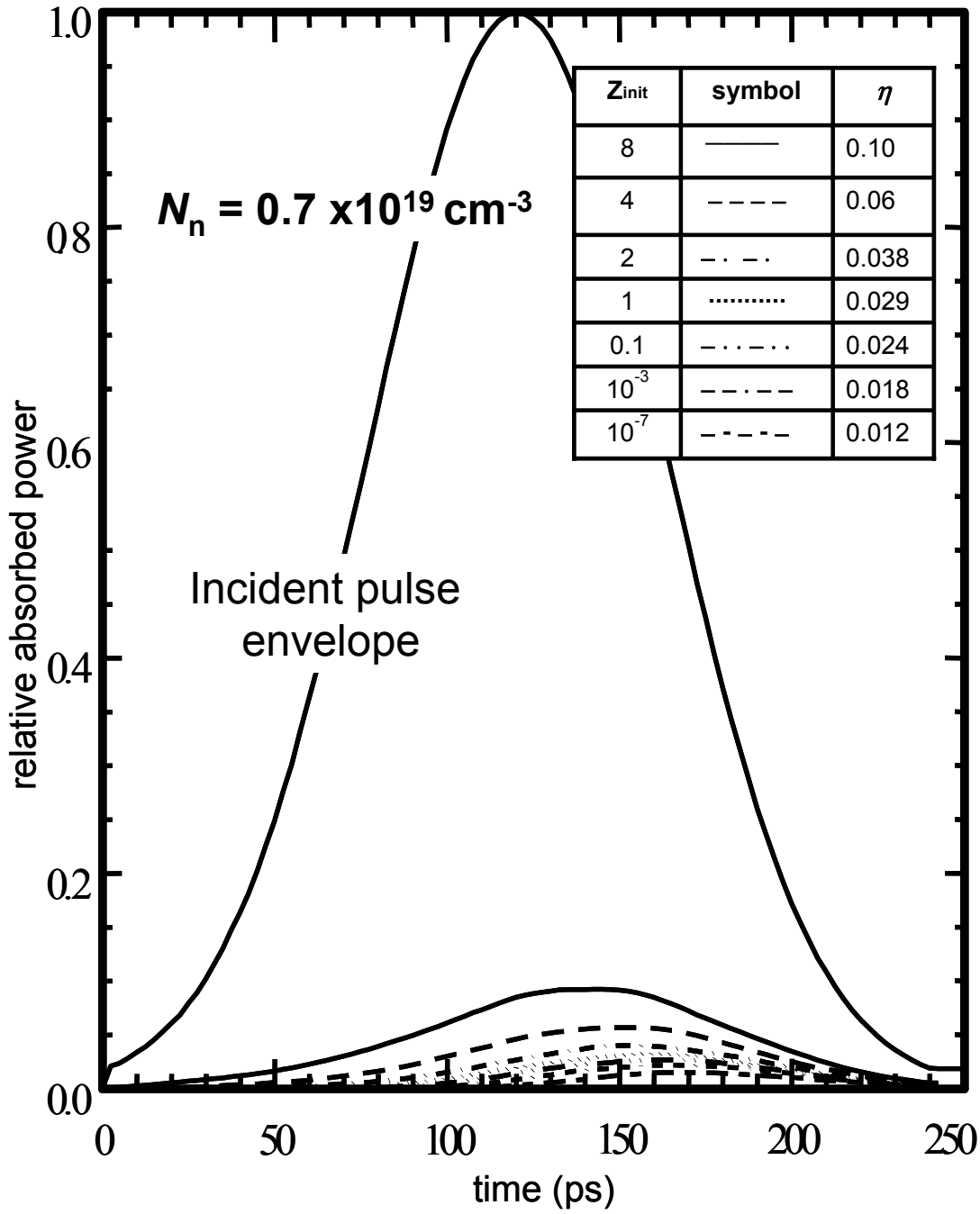

Figure 5.10: Calculation using self-consistent Bessel-beam plasma interaction code [10] of time-dependent Bessel beam absorption. The initial ionization state is varied from $Z_{init}=10^{-7}$ to $Z_{init}=8$, corresponding to the conditions encountered by a long pulse interacting with a range of targets spanning initially unclustered gas to a gas of large clusters. The initial gas density is $0.7X10^{19}cm^{-3}$ (200torr). Total absorption is given by η. Here, the absorption for $Z_{init}=8$ ("clustered") is ~10 times greater than for $Z_{init}\sim10^{-7}$ ("unclustered").

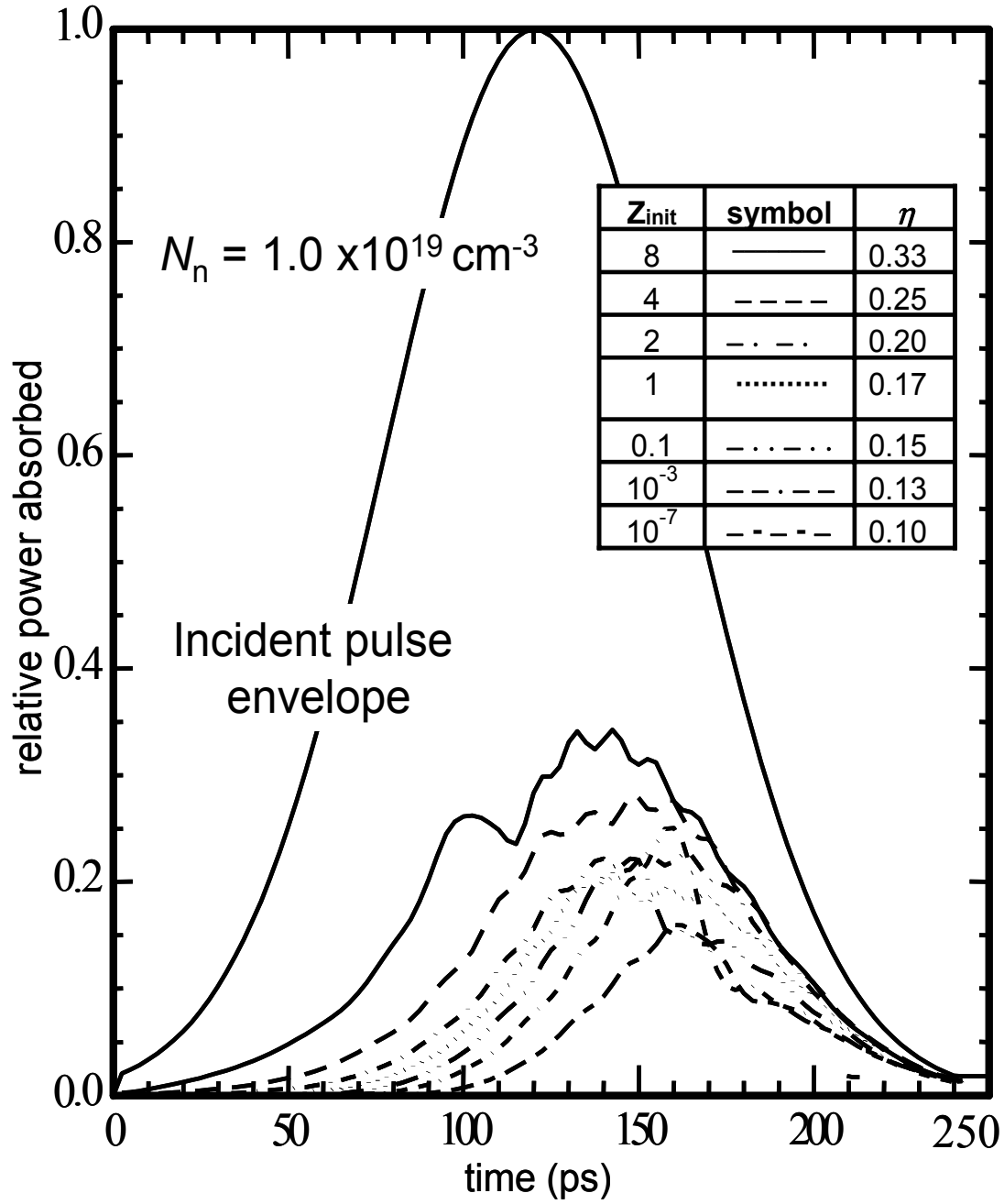

Figure 5.11: Calculation using self-consistent Bessel-beam plasma interaction code [10] of time-dependent Bessel beam absorption. The initial ionization state is varied from $Z_{init}=10^{-7}$ to $Z_{init}=8$, corresponding to the conditions encountered by a long pulse interacting with a range of targets spanning initially unclustered gas to a gas of large clusters. The initial gas density is $1.0X10^{19}cm^{-3}$ (300torr). Total absorption is given by η. Here, the maximum absorption of ~35% is predicted for the $Z_{init}=8$ ("clustered") case.

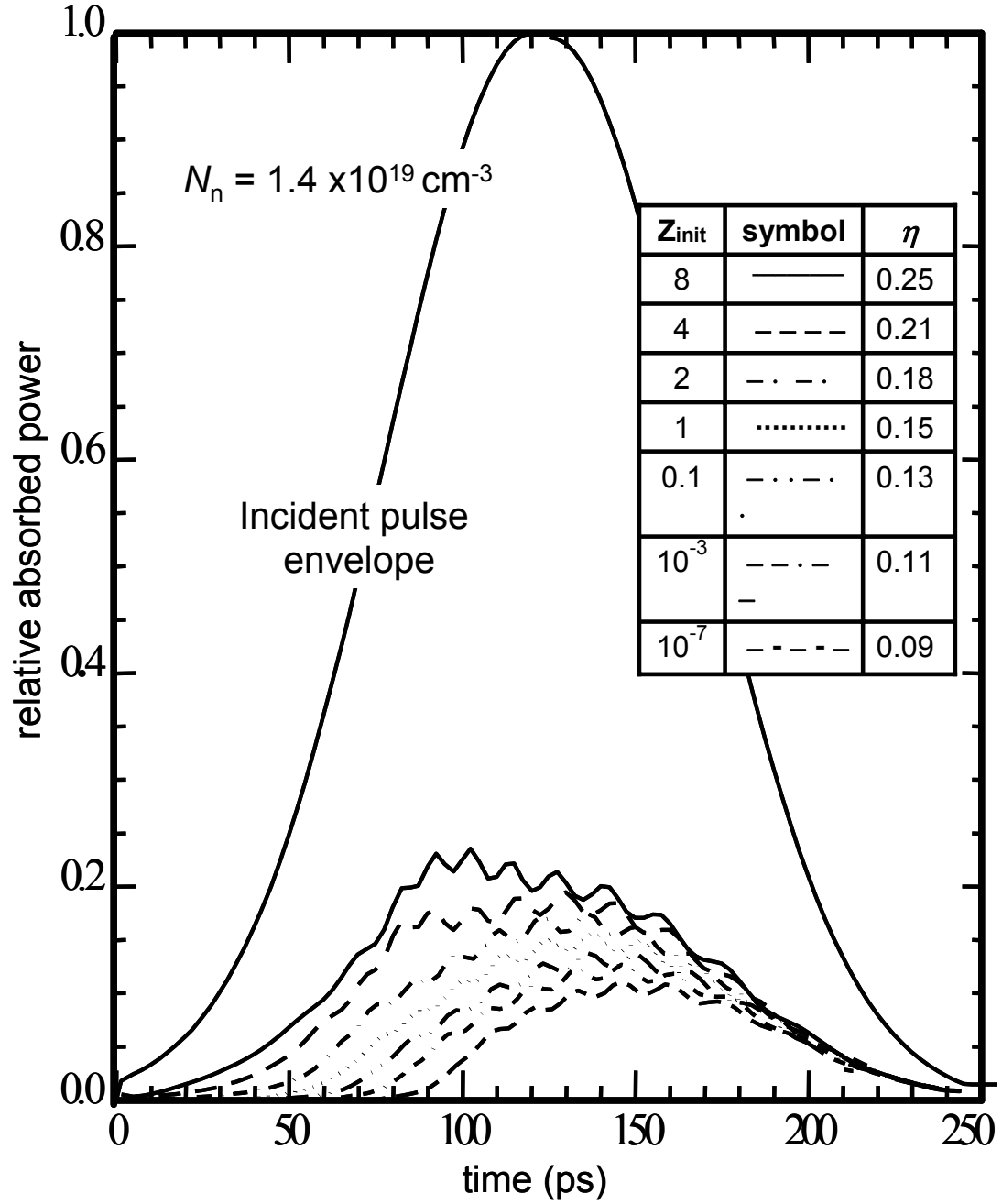

Figure 5.12: Calculation using self-consistent Bessel-beam plasma interaction code [10] of time-dependent Bessel beam absorption. The initial ionization state is varied from $Z_{init}=10^{-7}$ to $Z_{init}=8$, corresponding to the conditions encountered by a long pulse interacting with a range of targets spanning initially unclustered gas to a gas of large clusters. The initial gas density is $1.4X10^{19}cm^{-3}$ (400torr). Total absorption is given by η. Here, the absorption drops compared to the $1.0X10^{19}cm^{-3}$ case (Fig. 5.11) because the Bessel beam experiences incipient exclusion from the central region of the plasma.

List of References

Chapter 1 References

1. D. Attwood, *"Soft x-rays and extreme ultraviolet radiation: Principles and Applications"*, Cambridge University Press (2000)
2. S. V. Gaponov, N. N. Salashchenko, Proceedings of a Conference on Laser Optics. Leningrad, USSR, 4-8 Jan. (1982), E. Bjorkholm, *"EUV Lithography- The Successor to Optical Lithography?"*, Intel Technology Journal Q3'98 (1998)
3. G. D. Kubiak, L. J. Bernardez, K. D. Krenz, D. J. O'Connell, R. Gutowski, and A. M. M. Todd, OSA Trends Opt. Photonics Ser. **4**, 66 (1996). G. D. Kubiak, L. J. Bernardez, and K. Krenz, SPIE Proceedings **3676**, 669 (1999)
4. E. Spears and H. I. Smith, *"High Resolution Pattern replication Using Soft X-rays"*, Elec. Lett. **8**, 102 (1972); E. Spears and H. I. Smith, "X-ray Lithography- A High Resolution Replica Process", Solid State Technol. **15**, 21 (1972)
5. C. Krautschik, M. Ito, L. Nishiyama, K. Otaki, SPIE Proceedings **4343**, 392 (2001)
6. Y. Nakayama, S. Okazaki, N. Saitou, and H. Wakabayashi, J. Vac. Sci. Technol. B **8**, 1836 (1990); S. D. Berger, J. M. Gibson, R. M. Camarda, R. C. Farrow, H. A. Huggins, J. S. Kraus, and J. A. Liddle, J. Vac. Sci. Technol. B **9**, 2996 (1991)

7. B. J. Lin, SPIE Proceedings **4688**, 11 (2002)

8. D. Sweeney, *"Extreme Ultraviolet Lithography: Imaging the Future"*, Science & Technology Review, Nov. (1999)

9. G. T. Dao, R. S. Mackay and P. K. Seidel, SPIE Proceedings **4688**, 29 (2002)

10. D. A. Tichenor *et al*., *"System integration of the EUV engineering test stand"*, SPIE Proceedings **4343**, 19-37 (2001); D. A. Tichenor, G. D. Kubiak, W. C. Replogle, L. E. Klebanoff, *"EUV Engineering Test Stand"*, SPIE Proceedings **3997**, 48-69, (2000)

11. I. Crick, *"Extreme UV opens the door to next –generation lithography"*, Philips Research Password **22** February (2005)

12. H. Kinoshita, T. Watanabe, M. Niibe, M. Ito, H. Oizumi, H. Yamanashi, K. Murakami, T. Oshino, Y. Platonov and N. Grupido, SPIE Proceedings **3331**, 20 (1998)

13. J. B. Murphy, D. L. White, A. A. MacDowell, and O. R. Wood II, Appl. Opt. **32**, 6920 (1993)

14. H. N. Chapman and K. A. Nugent, SPIE Proceedings **3767**, 225 (1999)

15. H. Komatsuda, SPIE Proceedings **3997**, 765 (2000)

16. E. Hecht, *"Optics"*, 4th edition, Addison Wesley Publisher (2001)

17. M. Born, and E. Wolf, *"Principles of Optics: Electromagnetic Theory of Propagation, Interference and Diffraction of Light"* 7th Edition (1999)

18. E. Spiller, Appl. Phys. Lett. **20**, 365 (1972)

19. J. M. Slaughter, D. W. Schulze, C. R. Hillis, A. Mirone, R. Stalio, R. N. Watts, C. Tarrio, T. B. Lucatorto, M. Krumrey, P. Mueller, and C. M. Falco, J. Appl. Phys. **76**, 2144 (1994).

20. J. M. Slaughter, D. W. Schulze, C. R. Hillis, A. Mirone, R. Stalio, R. N. Watts, C. Tarrio, T. B. Lucatorto, M. Krumrey, P. Mueller, and C. M. Falco, *"Structure and Performance of Si/Mo Multilayer Mirrors for the Extreme Ultraviolet"*, J. Appl. Phys. **76**, 2144 (1994).

21. T. W. Barbee, S. Mrowka, and M. C. Hetterick, *Appl. Opt*. **24**, 883 (1985)

22. K. M. Skulina, C. S. Alford, R. M. Bionta, D. M. Makowiecki, E. M. Gullikson, R. Soufli, J. B. Kortright, and J. H. Underwood, *Appl. Opt*. **34**, 3727 (1996)

23. C. Montcalm, D. G. Stearns, S. P. Bajt, R. D. Behymer, M. A. Wall, and J. A. Folta, SPIE Proceedings **3331**, 42 (1998); C. Montcalm, B. T. Sullivan, H. Pepin, J. A. Dobrowski, and M. Sutton, *Appl. Opt.* **33**, 2057 (1994)

24. E. Spiller, *"Soft X-Ray Optics"* (SPIE, Bellingham, WA, 1994)

25. T. W. Barbee and D. L. Keith, *"Synthesis of Metastable Materials by Sputter Deposition Techniques"*, p. 93 in *Synthesis and Properties of Metastable Phases*; E. S. Machlin and T. J. Rowland, Editors (Metallurgical Society, Amer. Inst. Mech. Eng. Warrendale, PA, 1980)

26. J. A. Folta, *et al.*, SPIE Proceedings **3676** (1999); D. G. Stearns, *et al.*, Appl. Opt. **32**, 6952 (1993); P. A. Kearney, *et al.*, J. Vac. Sci. Tech. **B 15**, 2452 (1997)

27. D. L. Windt and W. K. Waskiewicz, J. Vac. Sci. Tech. **B 12**, 3826 (1994)

28. J. B. Kortright, E. M. Gullikson, and P. E. Denham, *Appl. Opt.* **32**, 6961 (1993)

29. P. N. Peters, R. B. Hoover, R. N. Watts, C. Tarrio, and A. B. C. Walker, Jr., SPIE Proceedings **2515**, 576 (1995).

30. S. Bajt, H. N. Chapman, N. Nguyen, J. Alameda, J. C. Robinson, M. E. Malinowski, E. M. Gullikson, A. Aquila, C. Tarrio, and S. Grantham, *Appl. Opt.* **42**, 5750 (2003).

31. G. Gutman, J. Keem, K. Parker, J. Wood, R. Watts, and C. Tarrio, SPIE Proceedings **1742**, 373 (1992)

32. D. Attwood, *"Soft X-rays and extreme ultraviolet radiation, principles and applications"*, Cambridge university press, (1999)

33. C. M. Garza, S. R. Palmer, and J. Shu, Optical Engineering **32**, no.10, Oct. 1993. p. 2328-36

34. W. Maurer, and A, Torres, ***"****RET options at 70nm"*, Microlithography World, **11**, no.4, p. 4-8, 16, Nov. (2002)

35. E. Bjorkholm, "*EUV Lithography-The Successor to Optical Lithography?"*, Intel Technology Journal Q3'98

36. D. A. Tichenor, et al., SPIE Proceedings **4688**, 72 (2002)

37. S. H. Lee, *et al.*, SPIE Proceedings **4688**, 266 (2002)

38. D. J. O'Connell *et al.*, SPIE Proceedings **5037**, 83 (2003)

39. K. A. Goldberg, P. Naulleau, P. Batson, P. Denham, E. H. Anderson, H. Chapman and J. Bokor, J. Vac. Sci. Tech. B, **18**, 2911 (2000)

40. H. N. Chapman *et al.*, J. Vac. Sci. Technol. B, **19**, 2389 (2001)

41. D. A. Tichenor *et al.*, SPIE Proceedings **4506**, 9 (2001)

42. C. Krautschik, M. Ito, I. Nishiyama, S. Okazaki, SPIE Proceedings **4688**, 289 (2002)

43. E. Gullikson, S. Baker, J. E. Bjorkholm, J. Bokor, K. A. Goldberg, J. E. M. Goldsmith, C. Montcalm, P. Naulleau, E. Spiller, D. G. Stearn, J. S. Taylor, J. H. Underwood, SPIE Proceedings **3676**, 717 (1999)

44. K. A. Goldberg, *et al.*, SPIE Proceedings **4688**, 329 (2002)

45. P. Naulleau, *et al.*, J. Vac. Sci.Technol. B, **19**, 2396 (2001)

46. T. Oshino, *et al.,* SPIE Proceedings **5037**, 75 (2003)

47. D. A. Tichenor, G. D. Kubiak, W. C. Replogle, L. E. Klebanoff, J. B. Wronosky, L. C. Hale, H. N. Chapman, J. S. Taylor, J. A. Folta, C. Montcalm, R. M. Hudyma, K. A. Goldberg and P. Naulleau, SPIE Proceedings **3997**, 48 (2000)

48. K. L. Blaedel, J. S. Taylor, S. D. Hector, P. Y. Yan, A. Ramamoorthy and P. D. Brooker, SPIE Proceedings **4688**, 767 (2002)

49. H. Becker, L. Aschke, B. Schubert, J. Krieger, F. Lenzen, S. Yulin, T. Feigl, T. Kuhlmann and N. Kaiser, SPIE Proceedings **4688**, 503 (2002)

50. P. B. Mirkarimi, D. G. Stearns, S. L. Baker, J. W. Elmer, D. W. Sweeny and E. M. Gullikson, J. Appl. Phys. **91**, 81 (2002)

51. A. Barty, P. B. Mirkarimi, D. G. Stearns, D. W. Sweeney and H. N. Chapman, SPIE Proceedings **4688**, 385 (2002)

52. P. Yan, *"EUVL Mask Patterning"*, International Sematech EUVL Mask Development Seminar (2002)

53. Y. Watanabe, K. Ota, H. Franken, *"Source requirement updated"*, International Sematech Source workshop, (2004)

54. U. Stamm, J. Kleinschmidt, K. Gabel, G. Hergenan, C. Ziener, G. Schriever, I. Ahmad, D. Bolshukhin, J. Brudermann, R. de Bruijn, T. D. Chin, A. Geier, S. Gotze, A. Keller, V. Korobotchko, B. Mader, J. Ringling, T. Brauner, SPIE Proceedings **5751**, 236 (2005).

55. I. N. Weinberg and A. Fisher, Nucl. Inst. Methods Phys. Res. A **242**, 535 (1986)

56. M. McGeoch, *Appl. Opt.* **37**, 1651 (1998)

57. V. M. Borisov, I. Ahmad, S. Goetze, A. S. Ivanov, O. B. Khristoforov, J. Kleinschmidt, V. Korobotchko, J. Ringling, G. Schriever, U. Stamm, and A. Y. Vinokhodov, SPIE Proceedings **4688**, 626 (2002).

58. S. Lee, P. Lee, G. Zhang, X. Feng, V. A. Gribkov, M. Liu, A. Serban, and T. K. S. Wong, IEEE Trans. Plasma Sci. **26**, 1119 (1998)

59. Y. Kato and S. H. Be, Appl. Phys. Lett. **48**, 686 (1986)

60. M. A. Klosner and W. T. Silfvast, Opt. Lett. **23**, 1609 (1998)

61. M. A. Klosner and W. T. Silfvast, J. Opt. Soc. Am. B **17**, 1279 (2000)

62. I. Krisch, P. Choi, J. Larour, M. Favre, J. Rous, and C. Leblanc, Contrib. Plasma Phys. **40**, 135 (2000)

63. T. Boboc, R. Bischoff, and H. Langhoff, J. Phys. D **34**, 2512 (2001)

64. E. Robert, B. Blagojevic, R. Dussart, S. R. Mohanty, M. M. Idrissi, D. Hong, R. Viladrosa, J.-M. Pouvesle, C. Fleurier, and C. Cachoncinlle, SPIE Proceedings **4343**, 566 (2001)

65. L. Juschkin, A. Chuvatin, S. V. Zakharov, S. Ellwi, and H.-J. Kunze, J. Phys. D **35**, 219 (2002).

66. N. R. Fornaciari, H. Bender, D. Buchenauer, J. Dimkoff, M. Kanouff, S. Karim, C. Romeo, G. Shimkaveg, W. T. Silfvast, and K. D. Stewart, SPIE Proceedings **4688**, 110 (2002).

67. K. Bergmann, G. Schriever, O. Rosier, M. Mu¨ller, W. Neff, and R. Lebert, *Appl. Opt.* **38**, 5413 (1999)

68. K. Bergmann, O. Rosier, W. Neff, and R. Lebert, *Appl. Opt.* **39**, 3833 (2000).

69. D. J. Nagel, C. M. Brown, M. C. Peckerar, M. L. Ginter, J. A. Robinson, T. J. Mcllrath, and P. K. Carroll, *Appl. Opt.* **23**, 1328 (1984)

70. U. Stamm, *"Extreme ultraviolet light sources for use in semiconductor lithography-state of the art and future development"*, J. Phys. D: Appl. Phys. **37**, 3244-3253 (2004)

71. B. Honnef, *"Taking light to new dimensions"*, 326th Heraeus Seminar, June 07 (2004)

72. M. A. Liberman, J. S. De Groot, A. Toor and R. B. Spielman, *"Physics of High-Density Z-Pinch Plasmas"*, Springer-Verlag (1999)

73. T. Krucken, K. Bergmann, L. Juschkin and R. Lebert, *"Fundamentals and limits for the EUV emission of pinch plasma sources for EUV lithography"*, J. Phys. D: Appl. Phys. **37**, 3213-3224 (2004)

74. N. V. Filippov, T. I. Filippova and V. P. Vinogradov, Nucl. Fusion (Suppl. 2) p 577 (1962)

75. J. W. Mather, *"Methods of Experimental Physics"*, Plasma Physics **9B**, ed H R Griem and R H Loveberg (New York: Academic) p 187 (1971)

76. H. Bhuyan, S. R. Mohanty, N. K. Neog, and S. Bujarbarua and R. K. Rout, J. Appl. Phys. **95**, 2975 (2004)

77. U. Stamm, J. Kleinschmidt, K. Gabel, G. Hergenhan, C. Ziener, G. Schriever, I, Ahmad, D. Bolshukhin, J. Brudermann, R. de Bruijn, T. D. Chin, A. Geier, S. Gotze, A. Keller, V.Korobotchko, B. Mader, J. Ringling, T. Brauner, *"EUV sources for EUV lithography in alpha-, beta- and high volume chip manufacturing: An update on GDPP and LPP technology"*, SPIE Proceedings **5751**, 236 (2005)

78. M. A. Klosner and W. T. Silfvast, Opt. Lett. **23**, 1609 (1998)

79. W. T. Silfvast, M. Klonser, G. Shimkaveg, H. Bender, G. Kubiak, and N. Fornaciari, SPIE Proceedings **3676**, 272, (1999)

80. N. R. Fornaciari, J. J. Chang, D. R. Folk, S. Gianoulakis, J. E. M. Goldsmith, G. D. Kubiak, B. C. Long, D. J. O'Connell, G. Shimkaveg, W. T. Silfvast and K. D. Stewart, SPIE Proceedings **3997**, 120, (2000)

81. N. R. Fornaciari, H. Bender, D. Buchenauer, J. Dimkoff, M. Kanouff, S. Karim, C. Romeo, G. Shimkaveg, W. T. Silfvast, and K. D. Stewart, SPIE Proceedings **4688**, 110 (2002)

82. J. Pankert, K. Bergmann, J. Klein, W. Neff, O. Rosier, S. Seiwert, C. Smith, R. Apetz, J. Jonkers, M. Loeken, G. Derra, SPIE Proceedings **4688**, 87 (2002)

83. Y. B. Zel'dovich and Y. P. Raizer, *"Physics of Shock Waves and High-temperature Hydrodynamic Phenomena"*, Academic Press, New York, p. 340 (1967)

84. T. Ditimire, T. Donnelly, A. M. Rubenchik, R. W. Falcone, and M. D. Perry, Phys. Rev. A **53,** 3379 (1996)

85. V. P. Krainov and A.S. Roshchupkin, Phys. Rev. A **64**, 063204 (2001)

86. G. J. Pert, J. Phys. A, **5**, 506 (1972)

87. S. Churilov, Y. N. Joshi, and J. Reader, *"High-resolution spectrum of xenon ions at 13.4nm"*, Opt. Lett. **28**, 1478 (2003)

88. D. W. Myers, I. V. Fomenkov, B. A. M. Hansson, B. C. Klene, D. C. Brandt, *"EUV Source System Development Update: Advancing Along the Path to HVM"*, SPIE Proceedings **5751**, 248 (2005).

89. F. Jin, M. Richardson, G. Shimkaveg, and D. Torres, SPIE Proceedings, **2523**, 81, (1995)

90. R. C. Spitzer, T, J. Orzechowski, D. W. Phillion, R. L. Kaufman, and C. Cerjan, *J. Appl. Phys.*, **79**, 2251 (1996)

91. A. Cummings, G. O'Sullivan, P. Dunne, E Sokell, N. Murphy and J White, J. Phys. D: Appl. Phys. **38**, 604-616 (2005)

92. S. Miyamoto, S. Amno, T. Inoue, A. Shimoura, K. Kaku, P. Nica, H Kinugasa, and T. Mochizuki, *"EUV Source Developments on Laser-Produced Plasmas using Xe Crygenic Target and Li new Scheme Target"*, Sematech EUV Source Workshop, 27 Feb (2005)

93. T. Nishikawa, *"EUV light sourve design by Li target LPP"*, Sematech EUV

Source Workshop, 27 Feb (2005)

94. H. Shields, S. W. Fornaca, M. B. Petach, M. Michaelian, R. D. McGregor, R. H. Moyer, and R. St. Pierre, SPIE Proceedings **4688**, 94 (2002)

95. B. A. M. Hansson, L. Rymell, M. Berglund, O. Hemberg, E. Janin, J. Thoresen, and H. M. Hertz, SPIE Proceedings **4605**, 1 (2001)

96. E. N. Ragozin, V. E. Levashov, K. N. Mednikov, A. S. Pirozhkov, and P. V. Sasorov, SPIE Proceedings **4781**, 17 (2002)

97. H. Stiel, U. Vogt, S. Ter-Avetysian, M. Schnuerer, I. Will, and P. V. Nickles, SPIE Proceedings **4781**, 26 (2002)

98. R. C. Constantinescu, J. Jonkers, P. Hegeman, and M. Visser, SPIE Proceedings **4146**, 101 (2000)

99. W. Svendsen and G. O'Sullivan, Phys. Rev. A. **50**, 3710 (1994)

100. Y. Shimada, Appl. Phys. Lett. **86**, 051501 (2005)

101. T. Mochizuki and C. Yamanaka, SPIE Proceedings **733**, 23, (1987)

102. F. Gilleron, M. Poirier, T. Blenski, M. Schmidt, and T. Ceccotti, J. Appl. Phys. **94**, 2086 (2003)

103. Shields H. Fornaca S W, Petach M B, Michaelian M, McGregor R D, Moyer R H and St Pierre R J 2002, SPIE Proceedings **4688** 94-101 (2002)

104. D. A. Tichenor *et al.*, Opt. Lett. **16**, 557 (1991)

105. T. Mochizuki, SPIE Proceedings **3886**, 306 (2000)

106. H. Shields, S. W. Fornaca, M. B. Petach, M. Michaelian, R. D. McGregor, R. H. Moyer, R. St. Pierre, SPIE Proceedings **4688**, 94 (2002)

107. B. A. M. Hansson, L. Rymell, M. Berglund, O. Hemberg, E. Janin, J.

Thoresen, and H. M. Hertz, SPIE Proceedings **4605**, 1 (2001)

108. B. A. M. Hansson, L. Rymell, M. Berglund, and H. M. Hertz, Microelectron. Eng. **53**, 667 (2000)

109. D. Moyer, Sematech Workshop on EUVL Source Development, San Jose, 2 March (2001)

110. M. Richardson, C.-S. Koay, K. Takenoshita, and C. Keyser, J. Vac. Sci. Technol. **B 22**(2), 785 Mar/Apr (2004)

111. R. Stuik, H. Fledderus, F. Bijkerk, P. Hegeman, J. Jonkers, M. Visser and V. Banine, *"Flying Circus EUV Source Comparison"*, 2nd International Sematch EUVL workshop 19-20 October (2000)

112. *For example*, CEO Optronics presentation, International Sematech EUVL Source Workshop, Santa Clara, CA, February 23, (2003)

113. Hiroki Tanaka, A. Matsumoto, K. Akinaga, A. Takahashi, and T. Okada, *"Comparative study on emission characteristics of extreme ultraviolet radiation from CO2 and Nd:YAG laser-produced tin plasmas"*, Appl. Phys. Lett. **87**, 041503 (2005)

114. S. Miyamoto, A. Shimoura, S. Amano, K. Fukugaki, H. Kinugasa, T. Inoue, and T. Mochizuki, *"Laser wavelength and spot diameter dependence of extreme ultraviolet conversion efficiency in ω, 2ω, and 3ω Nd:YAG laser-produced plasmas"*, Appl. Phys. Lett. **86**, 261502 (2005)

115. M. Yamaura, S. Uchida, A. Sunahara, Y. Shimada, K. Hashimoto, K. Nagai, T. Norimatsu, K. Nishihara, and C. Yamanaka, *"Characterization of extreme ultraviolet emission using the fourth harmonic of a Nd:YAG laser"*, Appl. Phys.

Lett. **86**, 181107 (2005)

116. E. Parra, S. J. McNaught, and H. M. Milchberg, Rev. Sci. Inst. **73**, 468 (2002)

117. S. J. McNaught, J. Fan, E. Parra, and H. M. Milchberg, Appl. Phys. Lett. **79**, 4100 (2001)

118. E. Parra, I. Alexeev, J. Fan, K. Y. Kim, S. J. McNaught, and H. M. Milchberg, Phys. Rev. E. **62**, R5931 (2000)

119. N. W. Krall and A. W. Trivelpiece, *"Principle of Plasma Physics"*, (San Francisco Press, San Francisco, 1986), p.147

120. E. Parra Ph.D. thesis, *"Interaction of Intense Laser Pulses with Noble Gas Clusters and Droplets"*, University of Maryland (2002)

Chapter 2 References

1. P. G. Gobbi and G. C. Reali, Opt. Comm. **52**, 195 (1984)

2. P. G. Gobbi, S. Morosi, G. C. Reali and Amin S. Zarkasi, *Appl. Opt.* **24,** 26 (1985)

3. A. E. Siegman, *Lasers* (University Science Books, Mill Valley, Calif., 1986

4. P. Walzel, in: Ullmann's Encyclopedia of Industrial Chemistry, 5th Ed., Vol. B2 (VCH, Weinheim, 1988), pp. 6.1-6.14.

5. S. P. Lin and D. J. Kang, Phys. Fluids **30**, 2000 (1987)

6. A.M. Ganan-Calvo, Phys. Rev. Lett. **80**, 285 (1998)

7. R. D. Reitz and F. V. Bracco, Phys. Fluid **22**, 1054 (1979)

8. M. R. Lindblad and J. M. Schneiger, J. Sci. Instrum. **42**, 635 (1965)

9. L. Malmqvist, L. Rymell, M. Berglund and H. M. Hertz, Rev. Sci. INstrum. **67**, 4150 (1996)

10. M. J. McCarthy and N. A. Molloy, Chem. Eng. J. **7**, 1 (1974)

11. H. M. Hertz, L. Rymell, M. Berglund, and L. Malmqvist, SPIE Proceedings **2523,** 88 (1995)

12. K-J. Wu, R. D. Reitz, and F. V. Bracco, Phys. Fluids **29** (4), April (1986)

13. E. Parra, S. J. McNaught, and H. M. Milchberg, Rev. Sci. Inst. **73**, 468 (2002).

14. M. J. Gouge, P. W. Fisher, Rev. Sci. Instrum. **68** (5), May (1997)

15. V. A. Rabinovich, A. A. Vasserman, V. I. Nedostup, L. S. Veksler, *"Thermophysical Properties of Neon, Argon, Krypton, and Xenon"*, Springer-Verlag, (1988)

16. S. J. McNaught, J. Fan, E. Parra, and H. M. Milchberg, Appl. Phys. Lett. **79**, 4100 (2001).

17. W. L. Kruer, *"The Physics of Laser Plasma Interaction"*, (Addison-Wesley, Redwood City, CA, 1988)

18. E. B. Treacy, IEEE J. Quantum Electronics, **QE-5**, 9, 454 (1969).

19. C. E. Thomas and L. D. Siebert, *Appl. Opt.* **15**, 462 (1976)

20. L.L.N.L. Laser Program Annual Report, UCRL-50021-76, 2-308 (1976)

21. Pulse stacker manufactured by Quantel.

22. E. M. Hodgson, C. J. Reason and I. N. Ross, SPIE Proceedings **369**, 140 (1982)

23. J. Kojima and Q. Nguyen, *Appl. Opt.* **41**, 6360 (2002)

24. J. A. R. Samson, *"Techniques of Vacuum Ultraviolet Spectroscopy"*, (Pied

Publications, Lincoln, 1980)

Chapter 3 References

1. S. J. McNaught, J. Fan, E. Parra, and H.M. Milchberg, Appl. Phys. Lett. **79**, 4100 (2001).
2. E. Parra, I. Alexeev, J. Fan, K. Y. Kim, S. J. McNaught, and H.M. Milchberg, Phys. Rev. E **62**, R5931 (2000).
3. R. L. Kelly, J. Phys. Chem. Ref. Data Suppl. **16**, 1 (1987); T. Shirai, K. Okazaki, and J. Sugar, J. Phys. Chem. Ref. Data **24**, 1577 (1995)
4. E. Parra, S. J. McNaught, and H. M. Milchberg, Rev. Sci. Inst. **73**, 468 (2002).
5. E. Parra Ph.D. thesis, *"Interaction of Intense Laser Pulses with Noble Gas Clusters and Droplets"*, University of Maryland (2002)
6. F. Gilleron, M. Poirier, T. Blenski, M. Schmidt and T. Ceccotti, J. Appl. Phys. **94**, 2086 (2003)
7. E. Miura, H Honda, K. Katsura, E. Takahashi, and K. Kondo, Appl. Phys. B: Lasers Opt. **70**, 783 (2000).
8. A. B. Borisov, J. W. Longworth, A. McPherson, K. Boyer, and C. K. Rhodes, J. Phys. B **29**, 247 (1996).
9. G. O'Sullivan, J. Phys. B **15**, L765 (1982)
10. S. Churilov, Y. N. Joshi, and J. Reader, Opt. Lett. **28**, 1478 (2003)
11. K.Y. Kim, I. Alexeev, and H. M. Milchberg, Appl. Phys. Lett. **81**, 4124 (2002)
12. T. R. Clark and H. M. Milchberg, Phys. Rev. Lett. **78**, 2373 (1997)

13. I. Alexeev, K. Y. Kim, and H. M. Milchberg, Phys. Rev. Lett. **88**, 073901 (2002)

Chapter 4 References

1. T. Tajima and J. M. Dawson, Phys. Rev. Lett. **43**, 267 (1979); P. Sprangle, E. Esarey, A. Ting, and G. Joyce, Appl. Phys. Lett. **53**, 2146 (1988)
2. E. Esarey, P. Sprangle, and A. Ting, IEEE Trans. Plasma Sci. **24**, 252 (1996)
3. C. J. Joshi and P. B. Corkum, Phys. Today **48**, 36 (1995)
4. P. L. Shkolnikov, A. E. Kaplan, and A. Lago, J. Opt. Soc. Am. B 13, 412 (1996); H. M. Milchberg, C. G. Durfee, and T. J. McIlrath, Phys. Rev. Lett. **75**, 2494 (1995)
5. J. Krause, K. Schafer, and K. Kulander, Phys. Rev. Lett. **68**, 3535 (1992); C. G. Wahlstrom, S. Borgstrom, J. Larsson, and S. G. Pettersson, Phys. Rev. A **51**, 585 (1995)
6. H. M. Milchberg, C. G. Durfee III, and J. Lynch, J. Opt. Soc. Am. B **12**, 731 (1995)
7. C.G. Durfee and H.M. Milchberg, Phys. Rev. Lett. **71**, 2409 (1993); S. P. Nikitin *et al.*, Phys. Rev. E **59**, R3839 (1999).
8. P. Volfbeyn *et al.*, Phys. Plasmas **6**, 2269 (1999)
9. E. W. Gaul *et al.* Appl. Phys. Lett. **77**, 4112 (2000).
10. C. G. Durfee III, H. M. Milchberg, Phys. Rev. Lett. **71**, 2409 (1993)
11. C. G. Durfee III, J. Lynch, and H. M. Milchberg, Opt. Lett. **19**, 1937 (1994)
12. C G. Durfee III, J. Lynch, and H. M. Milchberg, Phys. Rev. E **51,** 2368 (1995)

13. C. G. Durfee III, T. R. Clark, and H. M. milchberg, J. Opt. Soc. Am. B **13**, 59 (1996)

14. H. M. Milchberg, T. R. Clark, C. G. Durfee III, T. M. Antonsen, and P. Mora, Phys. Plasmas **3**, 2149 (1996)

15. J. Fan, E. Parra, and H. M. Milchberg, Phys. Rev. Lett. **84**, 3085 (2000)

16. J. Fan, E. Parra, K. Y. Kim, I. Alexeev, H. M. Milchberg, J. Cooley and T. M. Antonsen, Phys. Rev. E. **65**, 056408-1 (2002)

17. T. R. Clark, and H. M. Milchberg, Phys. Rev. Lett. **78**, 2373 (1997)

18. T. R. Clark, and H. M. Milchberg, Phys. Rev. Lett. **81**, 357 (1998)

19. M. V. Ammosov, N. B. Delone, and V. P. Krainov, Sov. Phys. JETP **64**, 1191 (1987). Zh. Eksp. Teor. Fiz. **91**, 2008 (1986)

20. T. R. Clark and H. M. Milchberg, Phys. Rev. E **61**, 1954 (2000)

21. L. Keldysh, Sov. Phys. JETP **20**, 1307 (1965)

22. M. V. Ammosov, N. B. Delone, and V. P. Krainov, Sov. Phys. JETP **64**, 1191 (1986)

23. S. Augst, D. Strickland, D.D. Meyerhofer, S. L. Chin, and J. H. Eberly, Phys. Rev. Lett. **63**, 2212 (1989)

24. T. Ditimire, T. Donnelly, A. M. Rubenchik, R. W. Falcone, and M. D. Perry, Phys. Rev. A **53,** 3379 (1996)

25. V. P. Krainov and A.S. Roshchupkin, Phys. Rev. A **64**, 063204 (2001)

26. G. J. Pert, J. Phys. A, **5**, 506 (1972)

Chapter 5 References

1. A. Butler *et al.*, Phys. Rev. Lett. **89**, 185003 (2002).
2. Y. Erlich *et al.*, Phys. Rev. Lett. **77**, 4186 (1996) ; D. Kaganovich et al., Phys. Rev. E **59**, R4769 (1999).
3. B.M. Luther *et al.*, Phys. Rev. Lett. **92**, 235002 (2004).
4. C.G. Durfee and H.M. Milchberg, Phys. Rev. Lett. **71**, 2409 (1993); S. P. Nikitin *et al.*, Phys. Rev. E **59**, R3839 (1999).
5. P. Volfbeyn *et al.*, Phys. Plasmas **6**, 2269 (1999)
6. E. W. Gaul *et al.* Appl. Phys. Lett. **77**, 4112 (2000).
7. K. Krushelnick *et al.* Phys. Rev. Lett. **78**, 4047 (1997); S. -Y. Chen *et al.* Phys. Rev. Lett. **80**, 2610 (1998)
8. I. Alexeev, K.Y. Kim, and H.M. Milchberg, Phys. Rev. Lett. **90**, 103402 (2003).
9. V. Kumarappan, K.Y. Kim, H. M. Milchberg, Phys. Rev. Lett. **94**, 205004 (2005)
10. J. Fan, E. Parra, and H. M. Milchberg, Phys. Rev. Lett. **84**, 3085 (2000); J. Fan, E. Parra, K. Y. Kim, I. Alexeev, H. M. Milchberg, J. Cooley and T. M. Antonsen, Phys. Rev. E **65**, 056408 (2002)
11. T. Tajima and J. M. Dawson, Phys. Rev. Lett. **43**, 267 (1979); P. Sprangle, E. Esarey, A. Ting, and G. Joyce, Appl. Phys. Lett. **53**, 2146 (1988)
12. K. Y. Kim, I. Alexeev, E. Parra, and H. M. Milchberg, Phys. Rev. Lett. **90**, 023401 (2003)

13. M. V. Ammosov, N. B. Delone, and V. P. Krainov, Sov. Phys JETP **64**, 1191 (1987). (Zh. Eksp. Teor. Fiz. **91**, 2008 (1986))

14. K.Y. Kim *et al.*, AIP Conf. Proc **647**, 646 (2002)

15. C G. Durfee III, J. Lynch, and H. M. Milchberg, Phys. Rev. E **51,** 2368 (1995).

16. W. P. Leemans *et al.*, Phys. Plasmas **5**, 1615 (1998)

17. O. F. Hagena and W. Obert, J. Chem. Phys. **56**, 1793 (1972); O. F. Hagena, Z. Phys. D **4**, 291 (1987).

18. E. Parra, S. J. McNaught, and H. M. Milchberg , Rev. Sci. Inst. **73**, 468 (2002)

19. K. Y. Kim, V. Kumarappan, and H. M. Milchberg, Appl. Phys. Lett. **83**, 3210 (2003)

20. T. R. Clark and H. M. Milchberg, Phys. Rev. Lett. **78**, 2373 (1997)

21. M. Takeda, H. Ina, and S. Kobayashi, J. Opt. Soc. Am. B **72**, 156 (1981)

22. I. H. Hutchinson, *"Principles of Plasma Diagnostics"* (Cambridge University Press, Cambridge, 1987)

23. J. Fan, T. R. Clark, and H. M. Milchberg, Appl. Phys. Lett. **73**, 3064 (1998)

24. T. Ditmire, E. T. Gumbrell, R. A. Smith, A. Djaoui, and M. H. R. Hutchinson, Phys. Rev. Lett. **80**, 720 (1998)

25. H. M. Milchberg, S. J. McNaught, and E. Parra, Phys. Rev. E **64**, 056402 (2001).